Electrochemical Studies On Porosity and Additives In Hot-Pressed Iron-Based Anodes

For The Iron-Air Battery Application

Master Thesis Report

G.G. Wolzak

Delft University of Technology

TU Delft

Electrochemical Studies On Porosity and Additives In Hot-Pressed Iron-Based Anodes

For The Iron-Air Battery Application

by

G.G. Wolzak

Student Name	Student Number
Geertje Wolzak	4491270

Committee:	Dr. P. Taheri, Dr. Y. Gonzalez-Garcia, Dr. P. Braga Groszewicz, Dr. A. Yilmaz
Duration Thesis:	August, 2022 - November, 2023
Faculty:	Materials Science and Engineering, TU Delft
Collaboration:	Ore Energy

TU Delft

Preface and Acknowledgements

This thesis work entitled 'Electrochemical Studies on Porosity and -Additives In Hot-Pressed Iron-Based Anodes For the Iron-Air Battery Application' is part of the Master Materials Science and Engineering faculty, University of Technology, Delft in cooperation with Ore Energy, Amsterdam.

By finishing this exciting project and journey, I want to thank my thesis committee Dr. P. Taheri, Dr. Y. Gonzalez-Garcia, Dr. P. Braga Groszewicz and Dr. A. Yilmaz for examining my thesis work. In special, I want to thank my daily supervisors Dr. Y. Gonzalez-Garcia and Dr. A. Yilmaz and for their guidance and support. I want to thank Dr. P. Taheri for being the chair of my committee. Last but not least, I want to thank the people from Ore Energy for the help doing the experiments, in-depth discussions and support.

Dear parents, siblings and Claire, thank you for the endlessly support, encouragement to develop myself to the fullest potential and always having my back. While having a bachelor's degree in Applied Physics, the master Materials Science and Engineering enriched my knowledge in a broad but also in a in-depth way. While having discovered the wide field of science and suitable applications coming along with this master, I will always be fascinated about its relevance in a world where materials play a key role everywhere where you look, now and in the future.

G.G. Wolzak
Delft, October 2023

Abstract

The reliability of battery performance is crucial for the implementation of long-term large-scale energy storage. The promising Iron-Air battery is known for its suitable properties relying on its advantageous iron-based anode, characterized by its high volumetric energy density, robustness, material abundance, low cost and scalability. The anode does however present drawbacks, such as self-discharge, hydrogen evolution reaction (HER) and initial- and gradual surface passivation. In previous studies the effect of porosity and specific additives have been presented as important factors in tackling these drawbacks. This multidisciplinary research aimed to study porosity and additive effects on the electrochemical behaviour and performance of iron-based mechanically-stable anodes, manufactured at elevated temperature and pressure. Specifically, the effect of 10wt% pore former K_2CO_3 on the initial capacity and on the passivation behaviour was studied by galvanostatic charge-discharge, with prior investigation on pore formation. In addition, the effect of high-performance additives (Bi_2S_3, Bi_2O_3, ZnS and FeS) was investigated on HER kinetics and the passivation behaviour, by cyclic voltammetry (CV) and galvanostatic cycling, respectively. Surface characterization was performed by optical microscopy, scanning electron microscopy (SEM), and profilometry. Post-test analysis was carried out by optical microscopy and X-ray Photoelectron Spectroscopy (XPS). An intensification of surface cracks was observed for the K_2CO_3-rich sample before testing and its initial discharge capacity is 27 mAh/g less than a sample without pore former, but passivated later than the pristine sample in the full cell. Amongst the additives, the highest cycle of 100% capacity retention was marked at cycle 41 for FeS and for Bi_2S_3 at cycle 29 in the full cell, both showing 100% retention in the half cell up to 36 cycles. FeS might benefit from its readily available soluble reservoir of S^{2-} ions. Bi_2O_3 showed the lowest capacity retention which might be explained by low conductivity, low solubility and/or lack of beneficial role of S^{2-} ions. However, the additive Bi_2O_3 showed great reversibility of discharge products in the CV, confirmed by the lower O1s peaks and the lower respective Fe_2O_3 and FeOOH peak in XPS spectra. The pristine sample showed in the CV over the cycles increased current density and slope near the HER potential, with low reversibility. Apart from Bi_2O_3 and ZnS, the pristine sample showed lower capacity retention than FeS and Bi_2S_3, confirming the effective working of these additives. This systematic study portrays a good starting point for further studying porosity and additive effects on the electrochemical behaviour in hot-pressed anodes for the upcoming Iron-Air battery. Improvements can be assigned to cell design, electrolyte control and further detailed porosity characterization. Another type of current collector might withstand higher current densities and anode thickness reduction can lead to higher discharge capacities over its lifespan.

Contents

List of Figures

List of Tables

Nomenclature

Abbreviations

Abbreviation	Definition
IEA	International Energy Agency
MAB(s)	Metal Air Battery(/ies)
CIP	Carbonyl Iron Particles
PAM	Pristine Active Material
OCP	Open Circuit Potential
MMO, Hg/HgO	Mercury/Mercury-oxide
SHE	Standard Hydrogen Electrode
DoD	Depth of Discharge
SoC	State of Charge
MDC	Mean Discharge Capacity
RT	Room Temperature
EOF	End of Formation

Symbols

Symbol	Definition	Unit
Q_{spec}	Specific capacity	[mAh/g]
Q	Capacity	[mAh]
E	Specific Energy Density	[Wh/kg]
P	Specific power	[W/kg]
V_m	Molar Volume	[m^3/mol]
i_a	Anodic current density	[mA/cm^2]
i_c	Cathodic current density	[mA/cm^2]
i_D	Discharge current density	[mA/cm^2]
i_C	Charge current density	[mA/cm^2]
C	C-rate: speed of battery discharge/charge expressed as fraction of nominal capacity	[0.1C, 0.2C etc.]
ρ	Density	[kg/m^3]
η	Coulombic/Faradaic Efficiency	[%]

1 Introduction

The international energy agency IEA publishes periodically data reports on CO_2 emissions and show in addition, that fossil fuels are still primary resource for generation of electricity [1]. Greenhouse gases such as CO_2 causes the enhanced greenhouse effect leading to global warming effect and thus climate change. Assigning the main the source of greenhouse gas emission to combustion of fossil fuels [2] for generation of electricity, a world-wide debate on green energy resources and energy transition has been established. In addition to green energy generators such as wind-, solar-, tidal, hydro- and wave power, a great opportunity has been found in energy storage. Since green energy from solar or wind power might suffer from inevitable volatility issues, green energy storage systems might anticipate on excess and demand gaps adequately. So, in addition to utilizing green energy resources, their power is utilized to its fullest potential continuously. If wind power generation is low, energy storage might help to supply energy which originates from excess of wind power stored accordingly. This might lead to both better electricity market control, precision forecasting and insurance on long term energy supply while maintaining low impact on the environment.

The need for green energy storage systems have motivated the technology field to develop low environmental impact batteries fully utilizing their potential while exhibiting promising scalability properties in order to implement them globally. Among these green batteries, Iron-Air batteries show excellent material- and electrochemical properties. The promising volumetric energy density and beneficial material properties of iron in alkaline solutions are reported which make the Iron-Air Battery attractive characterized by a volumetric energy density of 9677 Wh/L [3] compared to approximately 6100 Wh/L for Li-O_2 (excluding oxygen consumption), meta-stability, robustness, low cost 0.40$/kg and 59$/kWh compared to 68$/kg and 1000$/kWh) and low environmental impact (1.5 kg CO_2 equiv/kg compared to 7.1 kg CO_2 equiv/kg of lithium [4]. Compared to zinc, the iron-based anode shows no dendrite formation and offers high durability compared to other Metal Air Batteries (MAB) already, having a theoretical discharge capacity of 0.960 mAh/g calculated by Faraday's law of electrolysis [5] by the first oxidation step and is able to reach an additional value of 1.273 Ah/g. This is calculated by 320 mAh/g by formation of magnetite and additional amount of 485 mAh/g by the deep discharge step of Fe(II)/Fe(III) [6]. Implementation might change the landscape as seen in Figure 1.1.

The full Iron-Air battery's electrochemical behaviour and performance have not been reviewed widely yet. Rodriguez et al. [8] reported half and full cell performance together. However, studies on separate components flourish: studies on kinetics and electrochemical behaviour of bifunctional ORR/OER Air Diffusion Electrodes exist and iron-based anodes (researched for FeNi batteries as well) have been analyzed extensively with a focus on the main challenges: self-discharge, HER upon recharging (the Fe(II)/Fe(0) is close to the HER potential [6]) and initial and gradual surface passivation. Therefor, parametrization of hydrogen evolution reaction (HER) kinetics, discharge rate capabilities investigation and discharge capacities and capacity retention/lifetime determination are performed. The challenges have been the incentive for research to explore solutions. Many structures and designs of various iron-based anodes have been assessed. Within powder metallurgy, pressed-plate anodes show excellent properties such as the capability for simple composition modification or ease of design

Figure 1.1: Illustration of grid implemented batteries. Image retrieved from: "Iron-Air Batteries Are Here. They May Alter the Future of Energy." [7]

optimization. In addition, powder-pressed anodes provide a large surface area increasing discharge capacity already to a great extent.

Two main opportunity directions within powder metallurgy stem from pressed-plate anodes focused on recent porosity studies [3] [9, 10, 11, 12] and metal sulfide studies [12, 13, 14, 15, 16, 17]. However, different promising additives have not always been synthesized in the iron-based anode equally or analyzed with equal experimental conditions which makes direct comparison difficult. Some of the promising additives remark carbon structures studied by Hang et al. predominantly [18], n-alkanethiols [19], electrolyte based sulfide compounds and anode based sulfide compounds, frequently named: Bi_2S_3, Bi_2O_3, FeS. In addition, ZnS is mentioned as promising additive [17]. The focus will be on these. In addition, many combinations or different mass ratios have been conducted, which might lead to multiple differences such as surface morphology or porosity differences which would make direct comparison on HER or discharge rate capability examination impossible. In order to fully understand the electrochemical behaviour, new research questions are formulated:

1. What is the effect of 10wt% K_2CO_3 pore former on the initial capacity and after 20 cycles of iron-based pressed-plate pellets?
2. What is the effect of the additives Bi_2S_3, Bi_2O_3, ZnS and FeS on the HER and passivation behaviour of iron-based pressed-plate pellets?

Carrying out these two sub-questions with structured protocol might lead to novel insights into individual behaviour of the additives and pore formers. From here on, new pathways could be created to investigate the synergistic role of different additives and pore formers.

In Chapter 2, the literature review is given for this topic. Recent high potential developments considering iron-based anodes, porosity and additives have been given in order to understand their effect on the mechanical and electrochemical behaviour. Chapter 3 reflects the experimental research explaining the methodology of this study. In Chapter 4, the results will be presented. Moreover, in Chapter 5 all results will be elaborated in depth. Also, reflections and further research will be stated here. In Chapter 6, the overall conclusions will be given. This thesis work is part of the Materials Science and Engineering faculty from Delft University of Technology in collaboration with Ore Energy.

2

Advances in Hot-Pressed Iron Anodes

In this section, the advances on the effect porosity for the initial discharge capacity as well as the advances of additives as valuable opportunity within powder-pressed samples are elucidated.

2.1. Porosity

The porous nature of hot-pressed iron powders is directly linked to its high initial capacity. The accessibility of electrolyte to electrode is strongly related to the initial porosity on micro- and macro scale, particle morphology, pore size and geometry, shape and dimensions of the anode. Micro-scale porosity, surface roughness and roughening and anode morphology will be discussed.

2.1.1. Micro-scale Porosity

Micro-scale porosity is defined by from several μm to 1000 μm, and originates from porosity created by the degree of compactness of powder nature as well as pore former addition in that dimension range. The degree of compactness can be influenced by the particle sizes and by the applied pressure. According to literature performed by Posada et al. [20], potassium carbonate (K_2CO_3) is used as pore forming agent, and poly-ethylene (PE) is utilized as binder. The study by Posada describes the pore formation by decomposition of the potassium carbonates. As being mentioned earlier, the electrochemical performance of the anode is affected by accessibility of ions and electrons migration paths that are correlated to the surface- and internal contact area. The study by Weinrich et al. [3] stresses the dissolution of the pore former into the electrolyte.

Porosity (%) and pore size (μm) created by pore formers are distinguished. A bigger porosity may be created as the anode thickness is increased, in general. An increased porosity correlates with higher discharge capacity. With higher porosity an outstanding discharge capacity is measured up to 0.5 Ah/g [12]. On the other hand, higher porosity (along with a thicker anode) also means that the interior of the anode is barely utilized, when discharge products accumulate at the surface, blocking the migration of hydroxide ions. Looking at the pore size, a two-fold phenomenon occurs as well. Large pore size will increase the accessibility for migration of ions and electrons, but lower pore size will increase the contact area with the electrolyte [12].

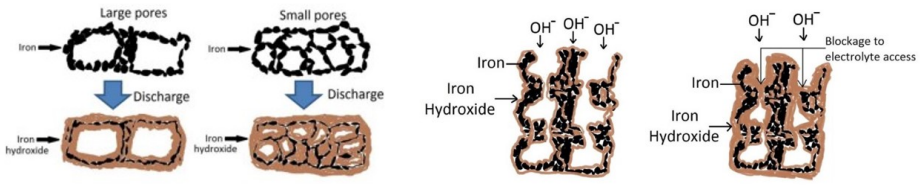

Figure 2.1: Left) The active material is increased when the pore size is increased. Note that this material is sintered and right) Schematic overview of the pore size, porosity on the accessibility of the anode. Images retrieved from Yang [12].

The discharge capacity that is predicted at maximum is C_{max}, K is a material constant with variables represented in the Table. The initial porosity (ϵ) should be corrected since the non-conductivity caused by irreversible discharge products filling up all open spaces within too high porosity would not add up to increased discharge capacity. This correction term k_{per} is equal to 0.2 which will cut the maximum allowed porosity at 61%. This corrected porosity is given in the third Equation of Table 2.1.

Table 2.1: Formulas reflecting porosity formulated by Yang et al. [12].

	Formula	Comments
C_{max}	$=\frac{\epsilon}{1-\epsilon}K$	$\cdot\ \alpha$ stands for the molar specific capacity
K	$=\frac{\alpha}{(V_2-V_1)\rho_1}$	$\cdot\ V_1$ and V_2 stand for the molar volume of the discharge and charge product
ϵ	$=\frac{1-(\frac{V_1}{V_2})}{1+k_{per}}$	$\cdot\ \rho_1$ is the density of the redox product from charging.

By Yang et al. [12], the porosity that gave highest discharge capacity in this study is estimated to be a value of 61% with pore size between 20-25 μm. It was remarked by Weinrich et al. [9], that the discharge capacity was linear depending on the charge capacity. Weinrich et al. state the importance of further investigation on a porous electrode resists high charging rates and investigation on the pore size.

According to Shangguan [21], it was mentioned that the manufacturing manner for sublimed sulphur, mechanical mixing results in larger pores, which increases the contact area, while allowing migration paths for OH^-. Notably, no information is given on differences in volume porosity or pore size. In addition, sulfur provides of porosity, since sublimed sulfur leaves behind pores. Mechanical mixing preserves larger particle size than ball milling since mechanical mixing does not decrease the particle size as much as ball milling.

2.1.2. Surface Roughness and roughening

The studies performed by Posada et al. [20] and Manohar et al. [16] state that the surface area becomes rougher at the formation process. Surface roughness may increase the surface area and therefore the discharge capacity [11]. Roughening can be obtained because the redox products are reversed back into iron Fe(0). Oxidative dissolution means the Fe(0) specie oxidizing into Fe(II) and precipitating at the surface. Upon reduction, the deep discharge products such as FeOOH is dissolved and converted back into iron hydroxide and oxide. Not all FeOOH is converted back and that describes the roughening process [11]. According to Manohar et al. [16] the active area increases upon formation. Considerably low active material can be ascribed to poor wettability of the anode. Poor wettability is solved by pore formers which increases the initial contact area and the pore volume. The binder clustering all the components inside the sample exhibit hydrophobicity, solved by adding a wetting agent. This hydrophobicity for water molecules may affect the migration paths of OH^-. A negative side effect of using potassium carbonate: dissolution of carbonate degrading cathode and therefore the performance of the cell. This is due to the fact that the carbonates fill the pores inside the air cathode, strongly affecting the ORR and OER rate [22].

The study that was performed by Weinrich et al. [11] characterized the topography upon formation by utilization of different techniques (X-ray photoelectron spectroscopy and electrochemical atomic force microscopy) to deepen the understanding of the evolution of the redox layer. These novel techniques unravel clear insights into the formation of the anode. It turned out that preferential precipitation sites for redox products were found, and the particle grew in size. This phenomenon was two-fold. On the one hand, the active material increased, thereby increasing the capacity. On the other hand, a passive layer was formed in between the particles, passivating the anode [11]. The observation of the increment in active surface material upon cycling was confirmed by a study performed by Weinrich et al. [9]. In this study, it was confirmed that the increase in surface area is improving the capacity, but when a too large volume of magnetite is formed, irreversibility comes to light which increases the passivation of the surface and thus decreases the capacity again. In the different studies, pore formation by pore formers was mentioned as happening while hot pressing or dissolving while exposed to the electrolyte. No explicit explanation has been given neither the choice for different pore formers. Although, Weinrich

et al. provided the most interesting different in-depth analysis of porosity phenomena.

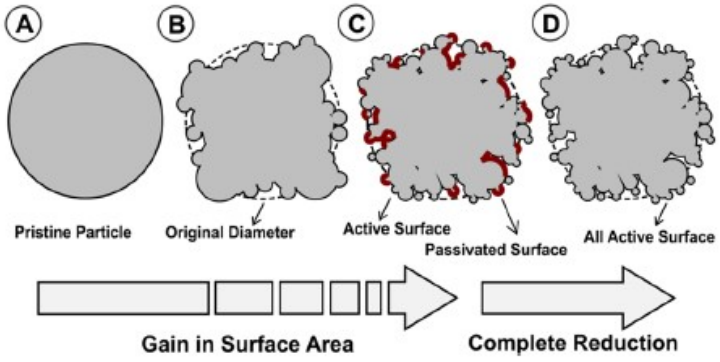

Figure 2.2: Increase in active surface area by precipitation/dissolution of the iron particles. Retrieved from Weinrich et al. [9].

2.1.3. Anode morphology

The shape and dimensions of the anode are also important aspects to consider. Although relatively thicker electrodes may exhibit higher porosity, the chance becomes higher that the inner electrode becomes inaccessible by the accumulation of less reversible magnetite. It is therefore recommended to utilize less thick electrodes. The contact area between electrolyte and electrode will increased. The ions migrate all at similar distance from the cathode, than the case where the anode is thicker and less high [10] [12]. A study on the porosity on micro-scale was illustrated by Weinrich et al. [10]. The wetting inside the anode is of significant importance. It has been shown in this study, that the utilization of a hydrophobic binder results in lack of wettability on the inside, but cannot be missed because of its binding properties. A steady discharge capability was measured for an electrode thickness of 0.60 to 3.22 mm. Individual particle surface area increased from 0.2 m^2/g to 0.5 m^2/g. The increased capacity is ascribed to the formation during which iron particles undergo coarsening by dissolution/precipitation upon cycling. Iron particles surface area grew (particle coarsening) due to gradually increasing wettability internally or by a binder displacement which can be caused by hydrogen evolution. An important question arises whether the displacement of the binder is detrimental to the cohesion between additives and CIPs of the electrode.

Initial wettability is low resulting in the relation defined as discharge capacity being inversely proportional to d, given a constant charge capacity of 16.7 up to 66.7 mAh per electrode. So at high thickness, the discharge capacity decreases due to reduced active material caused by the hydrophobicity of the binder [10]. The relation may be observed in Figure 2.3a). When looking at the curves, important to note is the description of the quantities, especially when focusing on specific or absolute capacity. In a) with smaller thickness and thus less active material the specific discharge capacity increases, since the charge capacity should be divided over less amount of active material. In d) the relation of specific charge capacity to specific discharge capacity is 1 to 1, and the total amount discharge capacity can grow with thickness and thus active material [10]. In order to reach the full depth of the anode it is estimated to make it as small as possible.

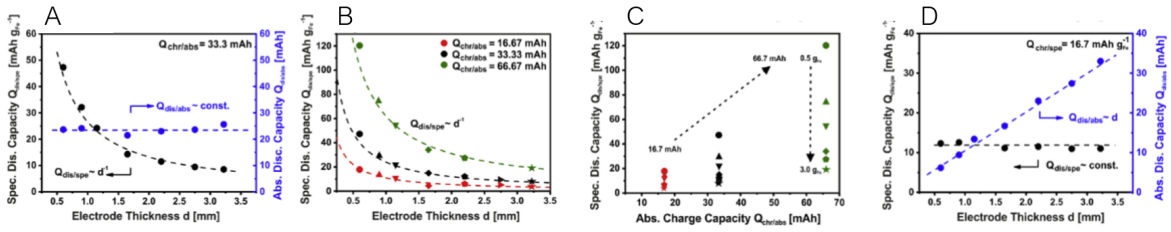

Figure 2.3: Relation on the thickness versus the discharge capacity. Image is retrieved and adapted from Weinrich et al. [10].

2.2. Comparative study on Additives

Additives give great outcomes against Hydrogen Evolution Reaction as well as suppression of passivation maintaining high discharge capacity or discharge rate capability ensuring high cycle life and capacity retention. Additives may be embedded into the structure via varying manufacturing processes and different synthesis of the overall powder pressed final products. Carbonyl Iron (CIP) is mostly used as iron powder with an average particle size of 3 to 5 μm, with high purity. It is stated that impurities are diminished during formation, which is decreasing the HER. The purity of carbonyl implies that no Mg or Cd are incorporated. These species accelerate the HER reaction. An elaborate explanation of the role of sulfide ions will be discussed at the end of this Section.

2.2.1. Additives: Bi_2S_3, FeS and Bi_2O_3

In this section, Bi_2S_3 and FeS in combination with Bi_2O_3 will be discussed, which is frequently mentioned as additive in literature [16]. Before discussing these promising additives, it is important to understand the working principle of HER-suppressing agents such as bismuth which is present in bismuth oxide and bismuth sulfide compounds. It is mentioned by Manohar et al. [14], that not only bismuth but also mercury, lead and cadmium and by Manohar et al. [16] that the same elements plus indium suitable agents against HER. A reasoning for this is given as:

- Elemental bismuth (and other elements such as mercury, lead, cadmium, indium) enhances the overpotential of HER, by alternating the electronic structure. This leads to higher activation energy for hydrogen evolution.
- Bismuth has a low surface energy and a low solubility, leading to low tendency to be re-distributed into the iron matrix. This leads to coherency with the iron bare surface [16]. It is also stated that Bi transforms into Bi_2O_3 during oxidation (over-discharge), albeit it reduces into elemental bismuth again upon charging.
- The specie bismuth is oftentimes also incorporated in iron hot-pressed powder as bismuth sulfide. According to the work of Posada et al. [20], Bi_2S_3 should be able to react with iron into Fe-S-Bi. Absorption of bismuth and sulfides might hinder the physical adsorption sites for absorption of hydrogen intermediate species that would subsequently prone to adsorption forming hydrogen. The phenomenon of this synergistic role is given as well in a study performed by Posada et al. [23] and a recommendation is to investigate the reaction between K_2S and Bi or K_2S and Bi_2S_3 [24] [25]. In addition, the additives Bi_2S_3 increase it even further since it is insoluble, electrically conducting and the electro-sorption of hydrogen intermediate species cannot take place by undesired energetic reactions.

Different studies performed by Manohar et al. [16] [14], looked upon the performance of the addition of additives FeS and Bi_2S_3 onto the iron electrode. The reactions that occur on recharging and discharging, respectively are:

$$Bi_2S_3 + 6e^- \rightleftharpoons 2Bi + 3S^{2-} \tag{2.1}$$

$$S^{2-} + Fe \rightleftharpoons FeS + 2e^- \tag{2.2}$$

The equilibrium potential is E^0 is -0.818V for Equation 2.1. The first Equation 2.1 is further directed into:

$$S^{2-} + Fe(OH)_2 \rightleftharpoons FeS + 2OH^- \tag{2.3}$$

According to Manohar et al. [16], the iron is synthesized in its purest form, CIP (carbonyl iron powder), with a particle size of 3 up to 5 μm. The charging efficiency is illustrated in Figure 2.4. Commercial electrodes consist of iron not manufactured from carbonyl iron, which may be manufactured from ore magnetite. As can be seen in the Figure, the addition of bismuth sulfide increases the coulombic efficiency.

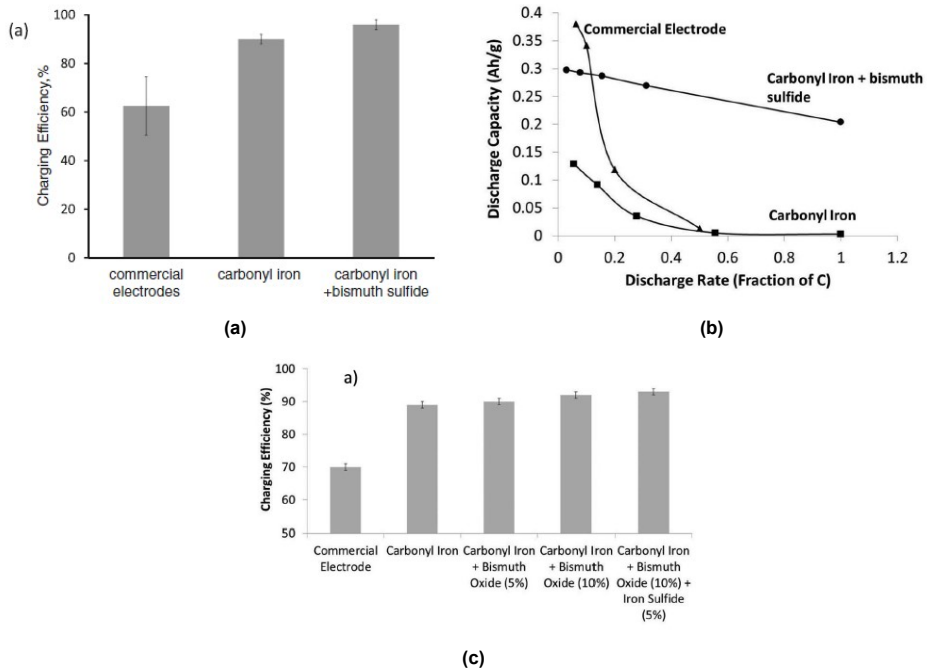

Figure 2.4: a) Charging efficiency (%) for a commercial electrode (no carbonyl iron, low-alloy steel), carbonyl iron and carbonyl iron plus bismuth sulfide. Image is retrieved from Manohar [16]. b) Plot of the electrode potential versus the specific capacity (Ah/g). c) Overview of different iron anodes tested on their coulombic efficiency. Images is retrieved from Manohar et al. 2012 (a,b) and 2013 (c) [16] [14].

The formation of FeS is explained from the reduction of Bi_2S_3, along with formation of other mixed-valent species, rearranging with iron hydroxide and sulfide ions into FeS. As being mentioned very often, this depassivates the bare iron metal allowing a high discharge rate capability and high discharge capacity. The discharge capacity versus the discharge rate is illustrated in Figure 2.4b). According to Manohar et al. [14], the function of sulfur is indicated as the increase in discharge capacity together with providing high discharge rates. Also, the surface is depassivated or dissolving residuals, while increasing conductivity. In this study, the effectiveness of Bi_2O_3 is tested. It was reported by Manohar et al. that the utilization of this additive increases porosity and also decreases compressive stresses and in addition to that, increased conductivity. It was not mentioned whether this was given in comparison to bismuth sulfide or examined individually on these properties. When bismuth (III) oxide is embedded in the powder, the reaction that takes place upon recharging consists of:

$$Bi_2O_3 + 3H_2O + 6e^- \rightleftharpoons 2Bi + 6OH^- \tag{2.4}$$

This reactions was expected to take place when recharging the battery (equilibrium reduction potential E^0 is -0.460V). The charging efficiency for different amount of bismuth (III) oxide is illustrated in Figure 2.4c). The systematical commercial electrode reflects an iron powder including impurities such as magnesium and calcium on which the HER may be accelerated. Lower charging efficiencies are measured with the addition of bismuth (III) oxide than for bismuth (III) sulfide. A reason for this is the morphology difference between the sample with Bi deposited by bismuth (III) oxide or bismuth (III) sulfide or due to a difference in particle size. Since, bismuth(III) oxide might exhibit larger particles from which the dispersion over the surface might be less. Moreover, the addition of FeS to bismuth (III) oxide did not give rise to significantly higher efficiency observed in Figure 2.4c). The discharge rate capability in combination with discharge capacity was measured as well. This is illustrated in Figure 2.5b).

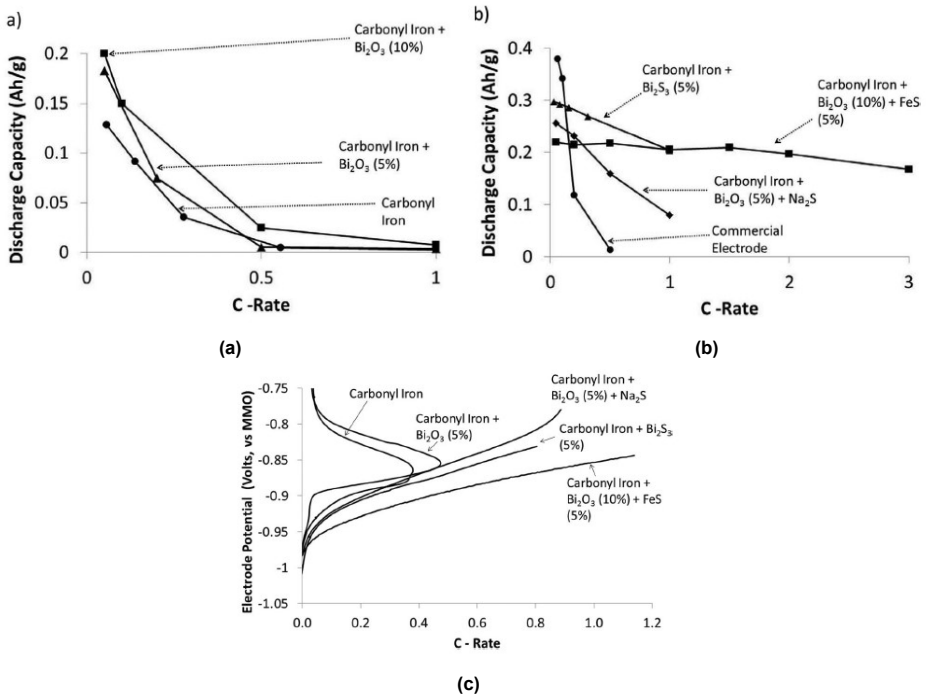

Figure 2.5: Electrochemical measurement of C-rate versus the discharge capacity [14]. a) CIP and bismuth oxide b) bismuth oxide/FeS and bismuth sulfide or bismuth oxide/sodium sulfide c) overview of the potentiodynamic polarization curve. All images are retrieved from Manohar [14].

When comparing Figure 2.4a) and Figure 2.4c) it can be concluded that Bi_2S_3 has a higher charging efficiency (96%) compared to 5,10% and 10% bismuth oxide with FeS with an efficiency of 90,92 and 93, respectively. The 5 % Bi_2S_3 has a higher discharge capacity, although it can not be retained at high C-rate [14]. Then, it was suggested that the Bi_2O_3 has much higher C-rates when FeS was added. It must be noted though, that the C-rate may decrease the battery's lifetime. When looked into the potentiodynamic polarization curve, the passivation only occurred for non-containing sulfur additives. It was concluded that the Bi_2O_3 in combination with FeS had much higher rates, which can be seen as well in Figure 2.5. A possible mechanism of the bismuth oxide in combination with iron sulfide might be that they have a synergistic effect on each other. Bi might deposit on the surface while preserving the sulfide ions simultaneously (they can get lost with bismuth sulfide). FeS provides a large reservoir of sulfide ions which can withstand high charging rates, because it exhibits high electrical conductivity while increasing active material of iron.

The study performed by Manohar et al. [13] confirms to earlier findings of Manohar et al. in 2013 [14], in which Bi_2O_3 in addition to FeS outperforms the additive Bi_2S_3. Manohar stated in a study in 2015 [13] that no difference in mechanism is looked upon Bi_2O_3 and FeS separately, which is done for the work of Manohar earlier in 2013 [14]. Note that this was given for 20 cycles. The cycle life was characterized extensively in contrast to earlier work of Manohar et al. in 2012 [16] and 2013 [14]. The electrode with Bi_2S_3 exhibits a discharge capacity of 0.3 Ah/g. The electrode with Bi_2S_3 had an efficiency of 96%. 50% of capacity loss measured at the 150th cycle. 2 mM K_2S increased the capacity, but was 60 % of the capacity was lost again in the 300th cycle. The carbonyl iron and bismuth oxide in addition with iron (II) sulfide had a discharge capacity of approximately 0.24 Ah/g constantly measured up to 1200 cycles. This was due to the fact that the FeS provided a large reservoir of sulfide ions. Cycle life was much better than the Bi_2S_3. Similar to Figure 2.5 and 2.4 discharge rate capability and discharge capacity is carried out as can be seen in Figure 2.6.

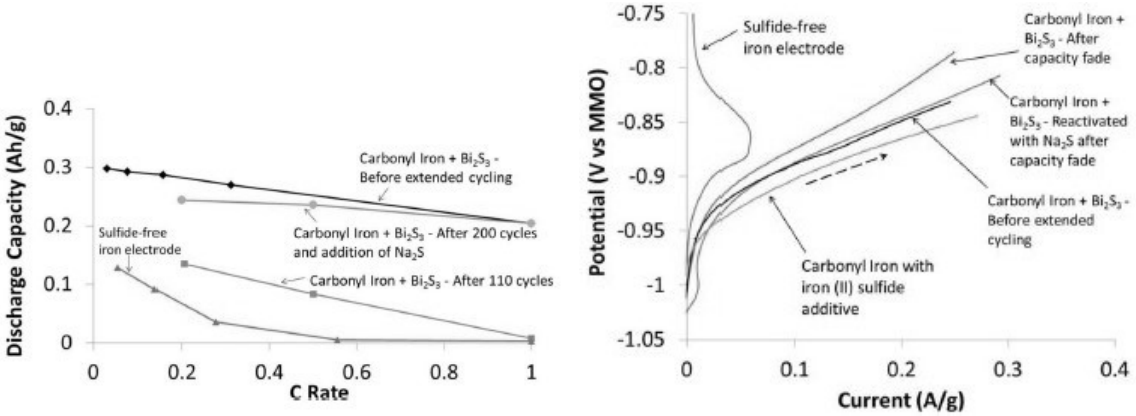

Figure 2.6: Electrochemical measurement of C-rate versus the discharge capacity a) and the potentiodynamic polarization curve (vs. MMO) b). Information is retrieved from Manohar et al. [13].

It was mentioned in previous work of Manohar et al. [16] [14] that the additive Bi_2S_3 sustained higher discharge capacity, but was only available at low C-rates. In this work, it was mentioned that the sulfide ions produced in Equation 2.1, could migrate towards the cathode and become irreversible meaning it is losing its sulfide ions, for the additive of Bi_2S_3. Accordingly, during discharge formed FeS by bismuth sulfide turned out to be much lower than the directly incorporated FeS, due to its reservoir build-up [13].

It can be confirmed, together with Figure 2.5 and 2.4, that passivation for Bi_2S_3 is mitigated by sulfur containing species, and increment of the discharge capacity occurred after cycling (200 cycles) when additional sulfur was added to the electrolyte. It must be noted that the charging capacity remained much higher for carbonyl iron with FeS and Bi_2O_3 than the Bi_2S_3 additive without adding additional sulfur. This confirms the observation that adding sulfur to the electrode in the form of FeS is much more efficient than adding it as Bi_2S_3 additive, since FeS provides a reservoir of S^{2-}. The capacity retained high (higher than for Bi_2O_3 and FeS), only at discharge rates lower than 1C for Bi_2S_3. The addition of sulfur to the electrolyte may increase the discharge rate capability and discharge capacity again. The irreversibility and gradual build-up of magnetite induces investigation on capacity fade. It was concluded that with the addition of sulfur ions, the capacity was retained again. A characterization technique confirmed the absence as well of FeS while investigating the formation of magnetite, hinting at the fact that sulfur was lost when magnetite accumulated during cycling. It was also stated, that the overpotential was increased by the accumulation of magnetite. In this study, it was confirmed as well that the higher discharge rates (1C) decreased the capacity significantly. It was observed as well that the DoD affected the capacity fade: 83% was recommended instead of 100%. This was highly probable done to prevent the anode from exceeding its charging and discharge limits. Overcharging at a slow rate retained the capacity as well. So, additional sulfide ions retain capacity by increasing conductivity as well as reversing magnetite into iron, by reducing the overpotential.

Although, the passivation properties seem more promising for FeS, Table 2.2 from Manohar et al. [14] hints at the fact that the efficiency is higher for Bi_2S_3. The sulfide ions which are immediately available for FeS, functions as large reservoir increasing cycle life, gradually providing its sulfide ions. The addition of sulfides to the electrolyte was recommended, but it was reported that the sulfide ions get gradually lost while migrating towards the cathode. FeS was praised in this work [13].

Table 2.2: Comparison of different additives on the discharge capacity and coulombic efficiency by Manohar et al. [14]. The active material was equal to 2g.

Anode additive	Dis. capacity (Ah/g)	Measured Eff. (%)	Cal. Eff. (%)
No additive	0.19	89	71
5 % Bi_2O_3	0.20	90	80
10 % Bi_2O_3	0.20	92	81
5 % Bi_2S_3	0.32	96	84
10 % Bi_2O_3 and 5% iron sulfide	0.25	93	82

2.2.2. Additives: ZnS, FeS, FeS_2 and Cu_2S

A recent highly interesting study was performed by Mitra et al. [17], which investigated different metal sulfides. The mechanism of metal sulfides is clearly described in this work. A comparative study was done for FeS, FeS_2, ZnS and Cu_2S investigating the effect of different metal sulfide additives. Conductivity and solubility is given in Table 2.3. Note that the solubility is given in water.

Table 2.3: Solubility and conductivity constant given for the investigated additives. Information retrieved from Mitra et al. [17].

Additive	El. conductivity (S/cm)	Sol. constant	El. Eq.	E^0 vs MMO
FeS	$1.5 \cdot 10^3$	$1.6 \cdot 10^{-19}$	$FeS + 2e^- \rightleftharpoons Fe + S^{2-}$	-0.97
FeS_2	$6 \cdot 10^{-1}$	$8 \cdot 10^{-26}$	$S_2^{2-} + 2e^- \rightleftharpoons 2\,S^{2-}$	-0.48
ZnS	$1 \cdot 10^{-6}$	$3 \cdot 10^{-23}$	$ZnS + 2e^- \rightleftharpoons Zn^{2+} + S^{2-}$	-1.41
Cu_2S	$6.5 \cdot 10^3$	$2.5 \cdot 10^{-48}$	$Cu_2S + 2e^- \rightleftharpoons 2Cu + S^{2-}$	-0.93

For the formation, soluble sulfide ions are needed. Since the solubility is very low for the metal sulfides other than FeS, a critical amount is reached to achieve that. ZnS has an intermediate solubility constant which hints at the fact that it exhibits a sufficient solubility which is required. The solubility is ranked: FeS>ZnS>Fe_2S,Cu_2S. A low solubility is needed in order to retain the sulfide ions, since too high solubility will result in loss of sulfide ions. Although, too low solubility prevents the working principle of sulfide ions and this phenomenon can be counteracted by adding a large amount of sulfides. For Fe_2S, Cu_2S the electro-reduction occurred. An appropriate balance needs to be found upon that electrochemical behaviour important for formation during the early cycles [16]. The formation by the addition of FeS decreases passivation by the fact that it increases conductivity and therefore increases performance. Although the solubility is very low, it is still losing sulfide ions over time resulting in oxidation of sulfide ions into sulfite and sulfate, since it has higher solubility compared to the other metal sulfides, Fe_2S, Cu_2S and ZnS: an extra amount of sulfide ions is then lost during charging cycles, which decreases depassivation capability since no FeS may be formed again. It is stated that corrosion is catalysed by FeS which is depassivating the interface electrode/electrolyte. In this work, it is mentioned that FeS has the highest solubility and almost highest conductivity. A suggestion may be that high solubility will lose sulfide ions occur more rapidly inducing corrosion.

At the end of formation (50 cycles), the discharge capacity was given. The C-rate for the discharge rate capability and life cycle was based on the capacity at cycle 50 (end of formation). In this work, it is confirmed as well that the purity of carbonyl material is enhancing the performance of the battery. The charging efficiency is highest for ZnS with the C/2 rate, followed by the C/5 rate, ending at the 1C rate for both charging and discharging. This specific rate is explained by the fact that too high discharging rates are increasing the internal resistance decreasing the utilization of the material. Too low rates such as C/5 increases the time that hydrogen evolution may affect the coulombic efficiency. ZnS exhibits the highest coulombic efficiency since the electrochemical reduction potential for ZnS prevented any loss when comparing all the equilibrium reactions. As can be observed from Table 2.3, the equilibrium potential for ZnS is lower than the applied potential, so the electro-reduction for ZnS is suppressed, which prevents the gradual loss of sulfide ions, is suggested. It was suggested by Mitra et al. that the HER takes place at iron or copper localized sites. These findings yield for the charging efficiency.

Consequentially, discharge rate capability and discharge capacity was investigated, by keeping the charging rate constant (C/2) and testing different discharging rates, 1C, C/2 and C/5. The capacity ratio was an indication for the discharge capacity since the charging rates were held constant. It turned out

that for even 1C discharging rates, the ratio was kept very high (95%). The utilization was measured to 0.25 Ah/g (cycle 10-16, discharge rate 1C) for ZnS compared to 0 Ah/g for the electrode without sulfide ions. So the discharge capacity for the additive ZnS was the highest as well. Note that it was unclear whether the discharge performances of the other additives was higher, since the charge capacity was not given. It was estimated that the charge capacities remained unchanged and were similar and so the discharge capacity was highest for: ZnS, FeS, FeS_2 ending at Cu_2S. The capacity retention is highest for FeS(99.4%) > ZnS(99%) > FeS_2(93%) > Cu_2S(81%), but all for a wide variety of life cycles. The cycle life for the ZnS was outstandingly considered as 750. It was shown that the coulombic efficiency went up for higher charge/discharge rates but at too high charge/discharge rates it reduced again. The capacity went down for too high charge/discharge rates (1C).

Table 2.4: Overview of the performance of the discussed metal sulfides by this work of Mitra et al. [17]. Electrodes are pressed-plate anodes with: CIP (70wt%), K_2CO_3 (10wt%), Bi_2O_3 (10wt%) and a polyethylene binder (5wt%) including the metal sulfide (5wt%). Data retrieved from the work of Mitra et al. [17]. All had discharge rate 1C unless mentioned otherwise. CR=Capacity retention, DC=Discharge capacity, CE=Coulombic Efficiency.

	CR C/2 charge/discharge	**CE initial (%) Cycle 50**	**CE final (%) Cycle 50+16**	**DC intial (Ah/g) Cycle 50**	**DC final (Ah/g) Cycle 50+16**
FeS	99.4% at 200	80	83	0.304	Capacity ratio 85%
FeS_2	93% at 200	70	70	0.317	Capacity ratio 75%
ZnS	99% at 750	85	87	0.326	0.25 (Capacity ratio 95%)
Cu_2S	99.4% at 180	70	74	0.340	Capacity ratio 65%

2.3. Summary of role sulfide ions

Various specific compounds with sulfide ions have been frequently named as promising additives which exhibit positive effects on the to overcome challenges such as HER and surface passivation predominantly [26] [14] [27]. Incorporation of sulfur ions and its effect on the physical cycling behaviour may be observed in Figure 2.7. It is made clear how the physical accumulation of discharge products take place with the different additives bismuth sulfide or bismuth oxide and iron sulfide. A clear suppression of surface passivation is illustrated by the presence of FeS in Figure 2.7b).

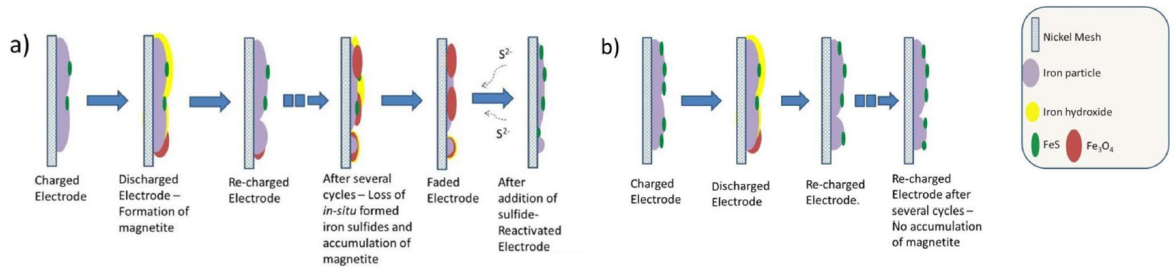

Figure 2.7: This overview indicates the electrochemical behaviour at the electrode-electrolyte interface after addition Bi_2S_3 (a) and Bi_2O_3 and FeS (b). Image is retrieved and adapted from Manohar et al. [13].

According to Hang et al. [26], it is mentioned that the sulfide ions are absorbed into $Fe(OH)_2$ oxide lattice, effectively breaking down the passivating layer that was formed. The additives may be thus, embedded into the the oxide lattice, strongly interacting with the crystal structure, enhancing formation of Fe(II,III)/Fe(III) [28]. When the sulfide is absorbed, the ionic conductivity is increased by formation of FeS, which in term lead to a higher reaction rate upon oxidation/reduction, while dissolution of iron is promoted [28] [21]. The iron hydroxide is modified so that it is more reversible [29]. The formation is faster in the presence of the sulfides [16], providing fast stability within the anode. The iron hydroxide is modified to be more reversible [29]. Sublimed sulfur is depleting $Fe(OH)_2$ and absorbed into the anode as well. They claim the occurrence of absorption followed by functioning as reservoir for S^{2-}. In case of the additive FeS, the cycle life may be enhanced significantly. According to Ravikumar et al. [30], small amount of sulfur can be absorbed into the first layers, which promotes dissolution of

the existing passivation layers. Bi_2S_3 is catalyzing reversibility of magnetite as well. It is measured that Bi_2S_3 augment the anodic dissolution of iron. According to Manohar [13], the overpotential of magnetite is lowered, increasing reversibility, allowing Fe(II,III) to Fe conversion. The function of the sulfide additives is properly understood by focusing on the mechanism of the sulfides: an increase in electronic conductivity, increase solubility of the discharge products and sustainable high discharge rates are described [16]. Suppressing HER, while enhancing Fe-H bonds by sulfides are documented [31].

2.4. Motivation of the Work

All in all, not only internal porosity increase the surface area and thus accessibility for OH^-, the porous structure accounts for the molar volume change of the redox products and the bare iron surface. Surface roughness and roughening effects needs to be taken into account as well. In micro porosity an optimal balance should be found between accessibility of the hydroxide ions while maintaining the interconnectivity between iron particles. It is clear that the function of bismuth oxide, bismuth sulfide and iron sulfide have a significant positive effect on the electrochemical behaviour of the anode. Moreover, the physical explanation is given on how these species prevent passivation and increase magnetite and iron hydroxide reversibility.

Although, studies in the literature are not consistent on how promising different additives are, and unclear why different content of additives should be used. In addition, often the choice has been made between bismuth sulfides or bismuth oxides or iron sulfide. The combination bismuth oxide and iron sulfide have higher discharge rate capability and higher discharge capacity there (around 0.2 mAh/g at 3C), but bismuth sulfide exhibits higher discharge capacity for lower C-rates. ZnS shows high capacity ratio and high charging efficiency, since it has low tendency to reduce sulfide ions. It should mark its ideality in combination with its low solubility. Remarkably, in literature, the synergistic effect between different species, that play a dominant role in the electrochemical equilibrium reactions on the electrolyte-electrode interface and in bulk is not clearly understood. A critical and distinct explanation should be given on the difference in working principle between additives, elaborating on the mechanism. A complexity is involved for comparing the performance of some promising additives iron-based anodes for Iron-Air Battery application, not only on the different electrochemical testing procedures but also on the manufacturing processes, cell designs, and chemical composition of the powder and additive. These research gaps drive this work and are the starting point for the research questions within this work.

3

Research Structure

3.1. Research Aim

The aim of this research is to state an in-depth analysis on electrochemical behaviour and performance in order to understand underlying formation mechanisms. This is elucidated by describing the individual role of pore formers and specific high-performance additives in order to circumvent the challenges of the iron-based pressed plates. More specifically, the role of pore formers on the initial capacity and durability is researched, and the role of additives on the hydrogen evolution and passivation behaviour is researched. Two research questions will be elucidated.

3.2. Research objective Porosity Studies

The objective on porosity is formulated in the following sub research question:

1. What is the effect of 10wt% K_2CO_3 pore former on the initial capacity and after 20 cycles of iron-based pressed-plate pellets?

The mechanism of creation of pores inside the powder structure is explained differently by different studies on pore formers. Weinrich [3] [9] [10] [11] et al. investigated pore formers and their effect thoroughly, but the exact mechanism of pore formation has not be described yet in hot-pressed pellets. Mechanisms can be understood as decomposing while hot pressing according to Posada et al. [20] or as dissolution when exposed to the electrolyte according to Weinrich et al. [10]. Allowing for stable hot-pressed pellet anodes, the thickness should be explored carefully providing high mechanical stability. According to McKerracher [6] a thickness of 1 mm anode was insensitive to capacity increment by addition of pore formers. If the anode is chosen adequately and higher than 1mm, adding of pore former could increase initial discharge capacity. On the contrary, Weinrich et al. [10] stated that an anode thickness >1 mm would lose specific discharge capacity drastically.

Hypothesis By 10wt% pore former the initial discharge capacity should be increased and should passivate later.

3.3. Research objective Additives Studies

The objective on additives is formulated in the following sub research question:

2. What is the effect of the additives Bi_2S_3, Bi_2O_3, ZnS and FeS on the HER and passivation behaviour of iron-based pressed-plate pellets?

Many studies have emphasized the effective role of bismuth in hydrogen evolution suppression as well as the successive function of sulfide compounds for passivation suppression. However, most promising additives have not been researched in a consistent study and compared and understood

clearly yet. Bismuth oxide has been revealed as additive incapable of prolonging high discharge capacity compared other bismuth sulfide, zinc sulfide or iron sulfide, whereas significant increase of coloumbic efficiency has been revealed by Manohar et al. [16] [13] [14] [15]. Coulombic efficiency has been investigated for 20 cycles for a combination of FeS and Bi_2O_3 and also for extended galvanostatic cycling for 1000 cycles. Important is to observe the HER kinetic behaviour over time for all individual additives facilitating not only observation of HER in the first cycle, but also over time. In addition an durability test could quantify coulombic efficiency and explain passivation or even degradation over time. In order understand electrochemical behaviour and the individual effect on formation mechanisms, their individual role should be clarified with consistent experimental protocol to unlock comparative studies on these additives. In addition, the ratio Fe:PE:additive should be held constant through the research.

Hypothesis All species can effect HER by reducing current densities near HER potential. Bismuth oxide can affect by electro-deposition of the HER suppressing element bismuth, gradually over time [14]. In addition, Zn shows low M-H absorption energy [32] probably leading to high coulombic efficiency. Upon the sulfide-containing species, ZnS might maintain highest discharge capacity by its low tendency to undergo electro-reduction providing an extensive reservoir of sulfide ions gradually utilized by its lower solubility [17] compared to FeS.

3.4. Overview

Different electrochemical and characterization techniques will be utilized to examine both sub-research questions. For the objective on porosity, porosity measurements will be done post-testing in combination with imaging via optical microscopy. Galvanostatic cycling will be performed in the half cell and the application-wise full cell. For the objective on additives, porosity and roughness measurements will be carried out and imaging in optical, digital and SEM microscopy helps to assess the iron-based anodes in combination with the additive. Additionally, XPS measurements address to identification of various discharge products after cyclic voltammetry. Furthermore, galvanostatic cycling tests in half cell and full cell are applied in order to further investigate the electrochemical behaviour.

4

Experimental Method

In this Chapter, the experimental method will be given. At first, the Anode Preparation Procedure will be explained. Optimization of the mechanical stability of the anodes was needed and thus researched in combination with the effect of fabrication method. When the optimal stability was found while considering porosity and particle size, the anodes were fabricated in optimized pressing procedure. In order to test the electrochemical kinetic parameters, behaviour and performance, the relevant electrochemical techniques will be explained, as well as the test configuration. Pre- and post-test characterization was carried out depending on the sub research question. Prior to electrochemical testing both sub-research questions were characterized by optical microscopy and isopropanol immersion. For the additives also SEM and profilometry was used. Post-testing for porosity, optical microscopy was used again. For the additives also XPS was used. A short overview is given in Table 4.1

Table 4.1: Overview of the applied techniques for investigation of the different research questions.

	Measurement	**Porosity studies**	**Additives studies**
Pre-test	Porosity measurement Surface analysis	Isopropanol immersion Optical microscopy	Isopropanol immersion Optical microscopy SEM Profilometry
Test	EC Analysis	BCD half cell GCPL half cell, full cell	Cyclic Voltammetry GCPL half cell, full cell
Post-test	Surface Analysis	Optical microscopy	Optical microscopy XPS

4.1. Anode preparation

In this Section both the material's properties and powder compositions will be given. In addition, the Hot Pressing Procedure will be given.

4.1.1. Material's properties and Powder compositions

In Table 4.2 the materials properties of the relevant powders are given. Particle size, purity and molecular weight are stated as well for further material characterization.

Table 4.2: Information of different specifications of the materials used [3]. *=hygroscopic **=after grinding.

	Purity (%)	Particle Size (μm)	Molecular Weight (g/mol)	Resource	Ref
Fe (CIP-OM)	97.8	3.9-5.2	55.85	ChemicalStore	[33]
PE (MIPELON)	Unknown	10	180 * 10^4	Mitsui Chemicals	[34]
K_2CO_3*	99	500	138.21	Sigma Aldrich	[35]
OH^-*	85	-	17.01	Thermo Fisher Sc.	[36]
Bi_2S_3	99.9	500**	514.16	Thermo Fisher Sc.	[37]
Bi_2O_3	99.9	$\sim$20	465.96	Thermo Fisher Sc.	[38]
ZnS	99.99	10	97.46	Sigma Aldrich	[39]
FeS	Unknown	400	87.91	Sigma Aldrich	

In Table 4.3 the relevant powder compositions are given that will be used in this work. Powders with the name FePE and FePEK_2CO_3 will be utilized to answer research objective on Porosity and FePE (also called pristine sample), Bi_2S_3, Bi_2O_3, ZnS and FeS are the relevant powder compositions for research objective on Additives . The solubility constant for ZnS is equal to 6*10^{-23}, for FeS equal to 10^{-19} [17] and Bi_2S_3 of many order of magnitude higher (10^{-73} is mentioned). Bismuth oxide is mentioned as practically insoluble. Note that all solubility constants are given in water. Electrical conductivity of ZnS was mentioned to be 10^{-6} S/cm and of FeS was equal to 10^3 S/cm [17]. Bi_2S_3 was assumed to be higher and Bi_2O_3 assumed to be lower than ZnS and FeS.

Table 4.3: Overview of the to be pressed anode compositions.

Sample name	Fe CIP-OM (wt%)	PE (wt%)	K_2CO_3 (wt%)	Bi_2S_3 (wt%)	Bi_2O_3 (wt%)	ZnS (wt%)	FeS (wt%)
FePE	94%	6%	-	-	-	-	-
FePEK_2CO_3	85%	5%	10%	-	-	-	-
Bi_2S_3	86.5%	5%	-	8.5%	-	-	-
Bi_2O_3	86.5%	5%	-	-	8.5%	-	-
ZnS	86.5%	5%	-	-	-	8.5%	-
FeS	86.5%	5%	-	-	-	-	8.5%

4.1.2. Hot Pressing Procedure and Mechanical Stability Optimization

In order to answer the two main sub research questions, the compositions including weight percentages had to be defined. Prior to the optimized hot pressing procedure; different compositions, materials, pressing times, loads and even mixing methods were used. It was required that the anode specimen was flat and exhibited high mechanical stability while maintaining porosity. Much modifications and observations were done in order to find the optimal pressing procedure and compositions which can be found in A.1. The overall procedure is given in Figure 4.1.

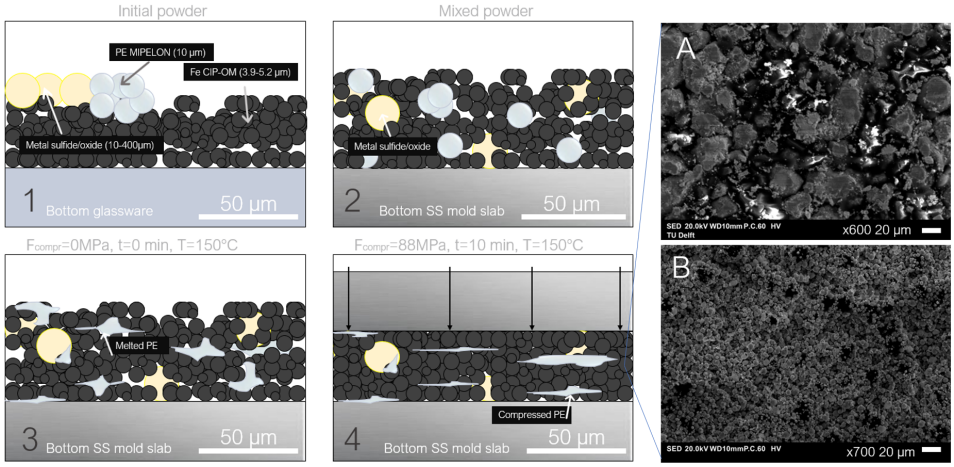

Figure 4.1: Side view of the step-wise production of a hot-pressed anode. SEM pictures A) and B) are from the top. Note that the PE was never melted, but brought near to its melting point. Therefore the particles of PE are not illustrated to scale.

Here the effect of ball milling and mechanical mixing was compared. Both manual mechanical mixing, machined mechanical mixing and ball milling were all applied to the powders to select the most promising mixing method. Manual mechanical mixing delivered overall unstable samples often in the presence of agglomeration of components without adequately mixing. Machined mechanical mixing as additional step to manual mixing showed overall stable behaviour for 15 minutes. The microstructure of a mechanically mixed sample can be seen in Figure 4.1B. However ball milling might exhibit high defect density making them more susceptible to corrosion desired for the cycling behaviour of the anode, as well as evenly mixing the powders. It was not chosen since the sample became a highly solid stable material without any porosity. The microstructure of a ball-milled sample can be seen in Figure 4.1A.

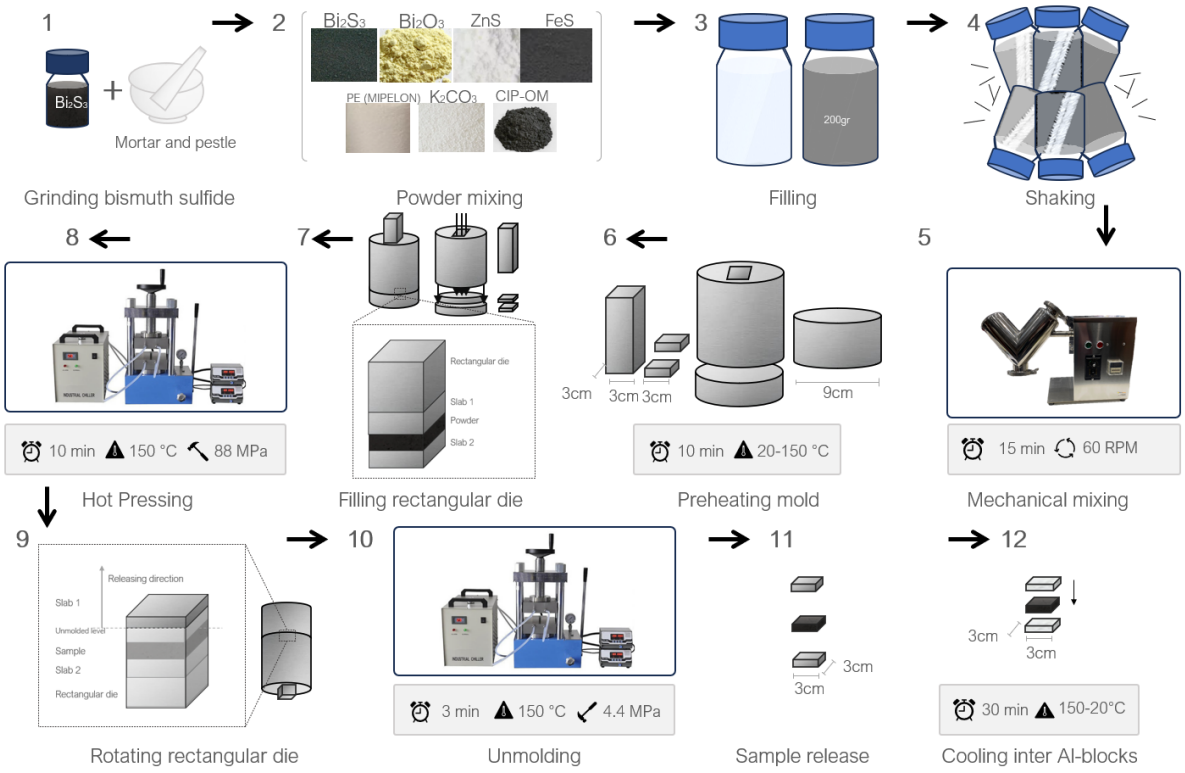

Figure 4.2: Twelve-step production from powder to hot-pressed iron anode.

In step 1) the bismuth sulfide chunks are grinded from a size of up to 2mm to a particle size of around 0.1mm. In step 2) the relevant powder is mixed with the adequate components with their correct weight percentage multiplied by 200gr for a full bottle of powder in order to make at least 14 samples per composition. Step 3) reflects a filled bottle of 200 gr with 3 relevant powder components after 2s of manual mixing. Step 4) reflects the manual shaking for around 3 minutes. In step 5) the total bottle is attached to the mechanical mixing system in which at 60 rpm for 15 minutes is mixed. Hereafter in step 6) the rectangular die containing mold, rectangular die, base plate, slabs and unloading mold are reflected (type MSE PRO Square Dry Pellet Pressing Set) which are preheated in the Hot Press (type Manual Flat Hydraulic Hot Pellet Press containing Double Plate).

In step 7) if the press and mold are fully heated to 150^{o}C, the powder is embedded in the mold in the order that the backplate is loaded with the mold onto the backplate. Hereafter in the open space; slab 1, powder, slab 2 and die is loaded. In step 8) the complete mold with powder is fully heated in between the flat heated plates. The turning wheel is lowered until it sandwiches the mold. Then the pressure is increased to 8 ton, equal to 88MPa for this mold size. After 10 minutes the press is released from its pressure. In step 9) the mold is taken out, the backplate is removed and the mold is rotated 180^o.

The unloading mold is placed on top and the entire configuration is placed back in the Hot Press. In step 10) the sample is released applying a pressure of approximately 4.4MPa, depending on the

friction inside the mold. When the entire die was located inside the mold (equal height of die and mold) it meant that the slabs and the just pressed powder was released. When the configuration is moved from the press and the unloading mold is removed, the sample in between the slabs as a sandwich structure can be removed in step 11). In step 12) the sample is cooled to room temperature for around 30 min. Aluminum slabs are utilized in order to apply the slabs to new sample preparation.

4.2. Cell components and Design

The cell designs for electrochemical testing in the half cell for anode are depicted in Figure 4.3. In the left and right picture the cell configuration of the half cell and full cell are reflected, respectively. Overall, the design was chosen so that the working electrode to reference electrode was equal to the reference electrode to counter electrode distance. In this manner, reduced IR drop could contribute to the overall kinetic parameters.

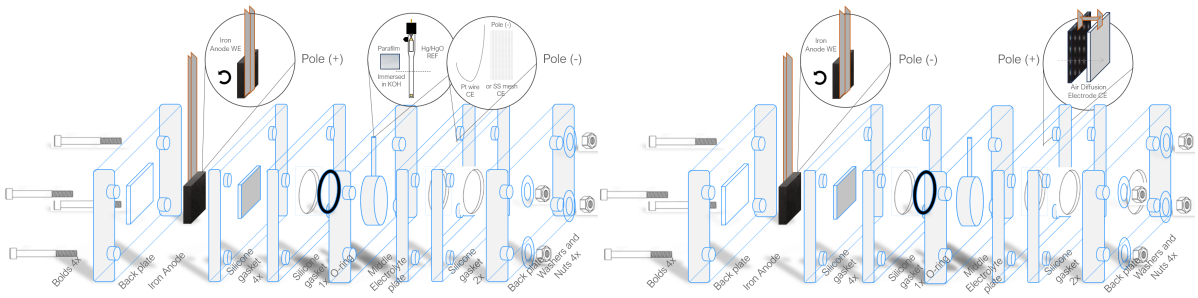

Figure 4.3: Left the half cell design and right the full cell design.

Both cells consist of three acrylic plates designed for a sandwiched structured battery cells containing two backplates and a middle plate for electrolyte filling. For each cell, four bolds, four nuts and washers were used. The cell had to be stacked and tightened by these bolds carefully and equally, since any pressure on one side of the anode might lead to cracking. Incorrect layering of the acrylic plates in combination with silicone gaskets could lead to small gaps and thus leakage. A rubber flat rubber (alkaline resistant) O-ring (23mm diameter) was needed additionally in between the middle plate and the silicone gaskets preventing the cells from leakage as well.

Utilizing this O-ring also ensured that the current densities could be selected with high precision, this the O-ring exposed a circular shape with diameter 23mm of the sample to the electrolyte. The maximum electrolyte volume of the cell was 5mL for both cells. Electrolyte is always 6M KOH by dissolving KOH pellets in purified water (demineralised water HATENBOERNEPTUNUS [40]). On the anode sample two copper tapes were used completely covering the backside of the electrode to ensure conductivity. Conductivity was always confirmed by a multi-meter (type 600V, 10A) by checking the resistance within the samples and counter electrode. Furthermore, their connection to the copper tape was also observed and confirmed.

For the half cell (left) a reference electrode MMO (+0.098V) was embedded and covered in parafilm in order to keep the same level of reference electrode in the electrolyte. As a counter electrode CE, a platinum (Pt) wire was used in case of cyclic voltammetry and for long-term galvanostatic cycling measurements, a stainless steel mesh was utilized providing a large surface area. In the full cell (right), the set up was almost equivalent. Although, the backplate contained a circular gap for oxygen accessibility, no reference electrode was used and as a cathode, an Air Diffusion Electrode (with bifunctional non-precious metal catalyst) [41].

4.3. Electrochemical Analysis

For all applied electrochemical techniques it is important to clarify the surface area for the current density. The exposed surface area A_{exp} and exposed volume V_{exp} were equal to:

$$A_{exp} = \frac{1}{4}\pi D^2 \tag{4.1}$$

With D the diameter of the O-ring equal to 23mm.

$$V_{exp} = \frac{1}{4}\pi D^2 d \tag{4.2}$$

with the thickness of the anodes d equal to 3.8mm.

$$V_{tot} = lwd \tag{4.3}$$

with a length l and width w equal to 30mm according to the dimensions of the surface area of the mold and a depth d equal to 3.8mm related to the mass of 13.4gr of composition mass per sample. The surface area exposed to the electrolyte was A_{exp} equal to 4.15cm^2. So, the current values should be based on this value by simply multiplying the surface area with the current density. The volume exposed was in each case V_{exp} was equal to 1.57cm^3 so a fractional value of 0.46 was calculated with a total volume of 3.42cm^3 for the anode.

4.3.1. Initial Capacity Determination

A galvanostatic charging/discharging technique was applied with just one 1 cycle. The technique was applied to both samples FePE and FePEK$_2$CO$_3$ according to Table 4.3. Note that the active material for the sample FePEK$_2$CO$_3$ is equal to 85wt% of the volume exposed to the electrolyte.

Multiplying the exposed fraction of volume (0.46) with the total mass per sample (13.4 gr) with also the amount of active material (96% for FePE and 85% for FePEK$_2$CO$_3$) brings the total effective active material to 5.91 gr for FePE and 5.24 for FePEK$_2$CO$_3$ assuming the electrolyte accesses the total depth of the anode. The samples were located in the half cell and tested with CorrTest instrument with an initial charge of 2hours at current I_C=12.3mA. Then the samples were discharged at a current I_D=12.3mA for sufficient hours (50) to make sure it would stop at a cut-off potential of -0.55V.

4.3.2. Kinetic Studies by Cyclic Voltammetry CV

Cyclic voltammetry is a power tool as electrochemical characterization technique revealing the redox potentials with corresponding current densities. By applying a linear time dependent potential peak potential and current density values can be read and evaluated for to kinetic behaviour analysis. Every next cycle By identifying the CV data per different, different characteristics can be made visible. The focus will be on the charge/discharge peaks, evaluating the charge/discharge capacity ratio. To identify the HER value, the peak potentials and overpotentials will be read from the curves after identifying the right peak to HER. The relevant reactions that should be identified are stated in Table 4.4 and Table 4.5.

For this reason, the potential range is stated -1.3V to -0.1V vs MMO. It was chosen to start the cycle at -0.9V vs MMO in anodic direction. Prior to this, the samples underwent -0.1V vs OCP for 2 or 5 minutes depending on their manufacturing time. A scanning rate of 10 and 5 mV/s resulted in too high current densities and too high resistance within the cell. Therefore, the scanning rate was determined at 0.5 mV/s. For reliability of the results every CV experiment was repeated 3 times and every measurement consisted of 20 full cycles. The number of 20 was chosen in order to understand the kinetics and HER intensification or reduction. In the results, the first cycles were not always considered because of the conditioning of the anodes. Because of the porous nature of the samples, it required some time for the electrolyte to fully enter the depth of the electrodes, which resulted in broad unidentifiable peaks in the first place. The current densities remained for all CVs relatively high because of large surface area of the samples. The CVs were carried out with Princeton Applied Research VersaSTAT 3 instrument. The O-ring was slightly higher, area equal to 4.52cm^2.

Table 4.4: Relevant redox reactions for iron oxidation/reduction steps. All potentials are given vs MMO. Fe/Fe(I) conversion described by Tian et al. [42]. Equilibrium potentials retrieved from Hang et al. [18] for Fe(II)/Fe(II,III) (note hydrate phase, 8M KOH) and Fe(II)/Fe(III) or Weinrich et al. [3] (note separate phase) and Rajan et al. for Fe/Fe(II) [43]

Conversion	Redox Reactions	E^0
Fe(0)/Fe(I)	$Fe + OH^- \rightarrow [Fe(OH)]_{ad} + e^-$	-
Fe(0)/Fe(II)	$Fe + 2\,OH^- \rightleftharpoons Fe(OH)_2 + 2\,e^-$	-0.98
Fe(II)/Fe(II,III)	$3\,Fe(OH)_2 + 2OH^- \leftrightharpoons Fe_3O_4\ (\cdot/+)\ 4\,H_2O + 2e^-$	-0.76
Fe(II)/Fe(III)	$Fe(OH)_2 + OH^- \leftrightharpoons FeOOH + H_2O + e^-$	-0.65

Table 4.5: Relevant redox reactions for additive oxidation/reduction steps. All potentials are given vs MMO. Reactions are retrieved from Mitra et al. [17], Manohar et al. [13] [14] and Weinrich et al. [3].

Additive/Ion	Formula	Redox Reactions	E^0
Bismuth (III) Sulfide	Bi_2S_3	$Bi_2S_3 + 6\,e^- \rightleftharpoons 2Bi + 3\,S^{2-}$	-0.92
Bismuth (III) Oxide	Bi_2O_3	$Bi_2O_3 + 3\,H_2O + 6\,e^- \rightleftharpoons 2\,Bi + 6OH^-$	-0.56
Zinc Sulfide	ZnS	$ZnS + 2e^- \rightleftharpoons Zn + S^{2-}$	-1.51
Iron (II) Sulfide	FeS	$FeS + 2e^- \rightleftharpoons Fe + S^{2-}$	-1.07
Sulfite	SO_3^{2-}	$SO_3^{2-} + 3\,H_2O + 6e^- \rightleftharpoons S^{2-} + 6\,OH^-$	-0.76
Sulfide	S^{2-}	$S^{2-} \rightleftharpoons S + 2\,e^-$	-0.62
Sulfide	S_2^{2-}	$S_2^{2-} + 2\,e^- \rightleftharpoons 2\,S^{2-}$	-0.56
Hydrogen	H_2	$2\,H_2O + 2\,e^- \rightarrow H_2 + 2\,OH^-$	-0.93
Oxygen	O_2	$O_2 + 2\,H_2O + 4\,e^- \rightleftharpoons 4\,OH^-$	+0.30
Additive/Ion	**Formula**	**Reactions**	**E^0 (V)**
Iron Hydroxide	$Fe(OH)_2$	$S^{2-} + Fe(OH)_2 \rightleftharpoons FeS + 2\,OH^-$	-
Iron (II) Sulfide	FeS	$S^{2-} + Fe^{2+} \rightleftharpoons FeS$	-
Bismuth (III) Oxide	Bi_2O_3	$Bi_2O_3 + 3H_2O + 3Fe \rightarrow 2Bi + 3Fe(OH)_2$	-

4.3.3. Durability Tests

Galvanostatic Cycling with Potential Limitation (GCPL) is performed in both half cell and full cell for both research questions. For these type of samples the current densities had to be optimized in order to research a sufficient DoD considering limitation of time. It was found that 10mA/cm^2 for 5 hours and even 5mA/cm^2 for 5 hours was too demanding for discharging for all samples and/or system set up and faded after 5 cycles for FePE and 10 cycles for the samples with the additives. It was decided therefore, to investigate 2mA/cm^2 for 10 hours for both charging and discharging to reach the same capacity.

For the research objective on porosity:

- A cut off was set at -0.70V[1] for the half cell with a current density of i_D equal to 2.18mA/cm^2 for 12.5h and i_C equal to 5.45mA/cm^2 for 5 hours all contributing to a total discharge and charge capacity of 113mAh. The sample underwent charging and then discharging (for all the other tests it was started with discharging). These measurements were done with Biologic instruments with EC-lab software and data acquisition.
- For full cell a current density of 2mA/cm^2 for 10h was chosen for both charging and discharging with a cut-off potential of 2V for charging and 0.001V for discharging. Full cells were measured in BTS Biologic systems with EC-lab software and data acquisition.

For the research objective on additives:

- For the anode characterization in half cell a current density of 2mA/cm^2 for 10h was chosen for both charging and discharging with a cut-off of -0.55V for discharging[2]. This testing was done in CorrTest instrument potentiostat/galvanostat (8-channel) model CS310X with CorrTest software and data acquisition.
- For full cell a current density of 2mA/cm^2 for 10h was chosen for both charging and discharging with a cut-off of 2V for charging and 0.001V for discharging. Full cells were measured in BTS Biologic systems with EC-lab software and data acquisition.

[1] This value prevented the anodes into deep discharge in order to check only the first oxidation plateau.

[2] This cut-off value -0.55V was based on a study by Rodriguez et al. [44] where it was ensured to study at least the first discharge plateau and probably the second was observed

Note that for the full cell performances, the efficiency is given as the first discharge capacity divided over the previous charge capacity. For the half cell, the capacity retention is given as the discharge capacity divided by the previous charge capacity. The actual initial retention was 4000% since the initial charge was 15 minutes. All half cell tests were stopped in different cycles, depending on its performance over time. This is considered when doing post-test surface analysis on the samples, mentioning the state. In the full cell, the test was stopped when the potential exceeded the upper limit (2V) and lower limit (0.001V) many times in a short time. Initially in the full cell, the tests were carried out up to 25 cycles, and extended in a another test.

4.3.4. Configuration Testing Set-up

The testing set-ups are revealed in Figure 4.4 and Figure 4.5. Note the difference in counter electrode for the cells in Figure 4.4, step 1 for the initial discharge capacity determination. Sample with pore former has a SS mesh and the sample without has air diffusion cathode as counter which could not be applied for the sample with potassium carbonate due to carbonization risks. In durability tests, the counter electrodes were identical.

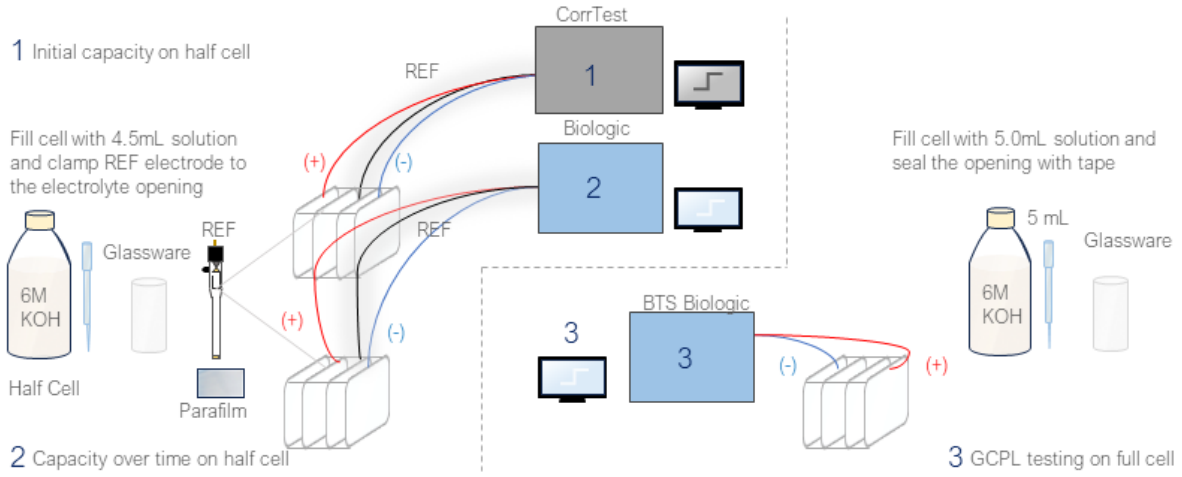

Figure 4.4: Illustration of testing set-up for Porosity studies. For the half cells the MMO REF electrode is clamped with parafilm in the cell. Full cell is sealed with tape. In setups 1, 2 and 3 are assigned to the test applied on either the half cell or the full cell with corresponding potentiostat/galvanostat.

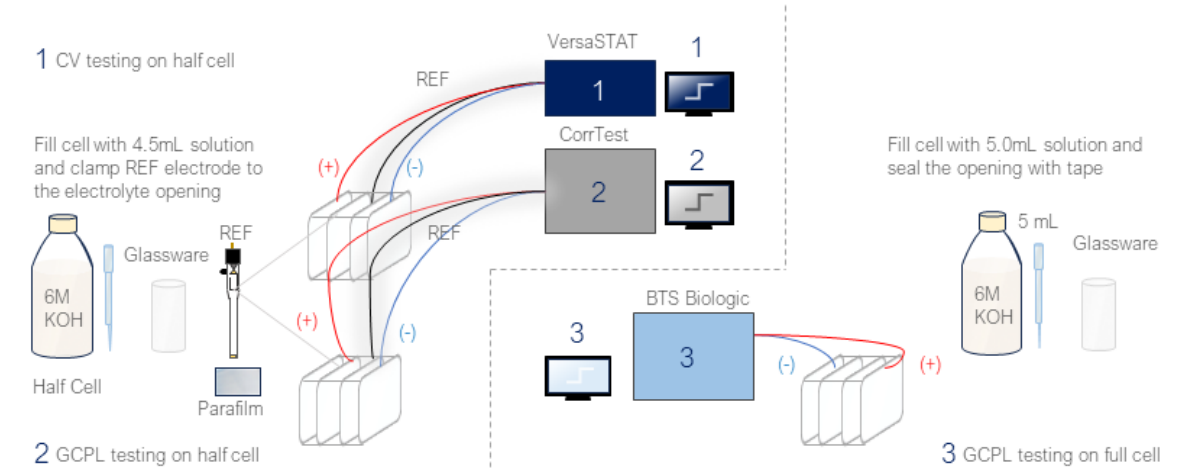

Figure 4.5: Illustration of testing set-up for Additive studies. For the half cells the MMO REF electrode is clamped with parafilm in the cell. Full cell is sealed with tape. In setups 1, 2 and 3 are assigned to the test applied on either the half cell or the full cell with corresponding potentiostat/galvanostat.

4.4. Anode Characterization

In these Sections, the experimental methods for the characterization of the anodes will be revealed. Porosity measurements consist of porosity initiation determination within the samples for Porosity Studies. Subsequently, the for all samples for both research questions, the porosity will be determined.

4.4.1. Porosity Measurements

Long-term decomposition

Within long-term decomposition, the samples with potassium carbonate, the samples will undergo long-term decomposition within a vacuum drying oven (DZF Vacuum Drying Oven model JUTU JTD-8000, Rotary Vacuum Pump XP135) for 3 hours at a pressure of p=-0.1 MPa and T=125^{o}C (a temperature lower than the melting temperature of PE). Decomposition should occur within hot pressing but because of the enclosed compartment within hot pressing, it is more plausible that the potassium carbonate will decompose following [45]:

$$K_2CO_3 \rightarrow K_2O + CO_2 \tag{4.4}$$

Another set of equivalent samples were cooled in open air. The mass was real-time monitored to see mass increment and pore initiation and analyzed. The methods were compared.

Isopropanol immersion

All samples for both Porosity studies and Additive studies were immersed in isopropanol as absolute porosity measurement. All immersed samples were brought to vacuum from -0.1 MPa to 0 MPa for three times in order to ensure full immersion of isopropanol. Samples were weighted before and after and with isopropanol density (0.786g/cm^3) and the total volume of the sample the porosity was calculated (%). The maximum capacity was estimated according to [12].

$$C_{max} = \frac{p}{1-p}K \tag{4.5}$$

With K equal to a material's constant for iron equal to 0.353 Ah/g with p the porosity [12]. This formula is used to determine the capacities based on a first rough estimation of porosity and measured porosity. Then it is utilized to compare it with the measured capacity.

4.4.2. Surface Analysis

Optical and Digital Microscopy

Two different types of optical microscopes were used in order to characterize the anodes: an optical microscope with objective lenses 4x, 10x, 40x and 100x WideField eyepiece 25x of type OMAX (software OMAX AmScope Toupview) were used and an digital microscope KEYENCE model VHX-5000, magnifications in between 20x and 2500x. Both microscopes served for both pre-test characterization as well as post-electrochemical characterization. Predominantly, KEYENCE allowed for three-dimensional imaging, to map the overall roughness and porosity behaviour, whereas OMAX mainly served for 2D imaging.

Profilometry

For profilometry a 3D Optical Profilometer (BRUKER interferometer) was used allowing for roughness parameterization with high effective vertical resolution. An intermediate magnification of 20x was used for roughness determination on a stitched area (1mm by 1 mm). The roughness measurements after electrochemical analysis were carried out with KEYENCE 3D imaging technique with lower lateral resolution to map the total depth.

Scanning Electron Microscopy (SEM)

In order to look into particle distribution and porosity within the sample, a Scanning Electron Microscope (SEM type JSM-IT100) was utilized. This type of microscope is based on inelastic electron scattering releasing secondary electrons, from which higher intensities will be visualized as brighter spots in the image. In addition, with this microscope, Energy Dispersive X-ray Spectroscopy (EDX/EDS) was applied in order to identify the areal chemical composition of different powders in the sample. This was applied to the sample with Fe, PE and ZnS and a sample that was ball-milled. EDX relied on high

precision detection of characteristic X-ray emission by electron relaxation process of filling an inner electron, therefore having elemental mapping visualization capabilities.

X-ray Photoelectron Spectroscopy (XPS)
X-ray Photoelectron Spectroscopy was applied in order to characterize the discharge products on the post-CV samples containing the four different additives (Bi_2S_3, Bi_2O_3, ZnS and FeS). The system (XPS instrument Phi system) consists of an high vacuum chamber (reached <10^{-7} tor) in which the sample of dimension of 1mm by 1mm in a holder was positioned. In this system, an electron beam was focused on an Al Kα anode which emitted monochromated characteristic X-ray with known energy. Subsequently, this beam was focused on the sample, on which the photoelectric effect lead to emission of photoelectrons towards an Energy Analyzer interpreting the binding energies following the equation:

$$BE = hv - KE - \phi \tag{4.6}$$

in which hv is the X-ray energy of Al kα, KE is the kinetic energy of the photoelectron, ϕ is the work-function and BE is the binding energy of the electron. The intensity (counts/second) versus binding energy spectrum could be provided by the analyzer and the software. At first, the full survey was obtained and hereafter the Fe2p and O1s peaks were measured in high resolution. Full survey and high resolution peaks were interpreted and analyzed by PHI Multipak software. XPS peak deconvolution for compound binding analysis was carried out with the software of PHI MultiPak as well, with Shirley background filtering and with a fitting approach of Gauss-Lorentz ensuring a χ^2 less than 40.

Before deconvolution of the peaks from XPS, all spectra were carbon-shifted according to adventitious carbon on the sample towards 284.8eV. The sample containing ZnS was shifted with respect to Zn2p$_{3/2}$ peak around 1022eV. All peaks were examined on their (relative) intensity in the specific spectrum and in addition, to the other compounds. All theoretical/reference peaks from Fe2p spectra were relied on the average theoretical peaks from the 'Handbook of X-ray photoelectron spectroscopy' by Chastain et al. [46]. All theoretical values in the high resolution O1s peak relied and were based on literature [47]. Note that the difference between Fe2p$_{3/2}$ and Fe2p$_{1/2}$ implies the spin-orbit splitting.

5

Results

The results are subdivided into the results on Porosity studies and Additive studies structured by pre-test characterization, electrochemical analysis and post-test surface analysis.

5.1. Porosity studies

The results on the porosity are given in this Section. The characteristics of the anode – macroscopically and microscopically – before electrochemical analysis will be given.

5.1.1. Pre-Test Characterization

In Figure 5.1, different observations of a sample with pore former are given. No consistency was observed with the addition of pore former into the samples. Artifacts such as non-uniform distribution, side cracking, cracking inside the pores along the pores and coarsening were observed.

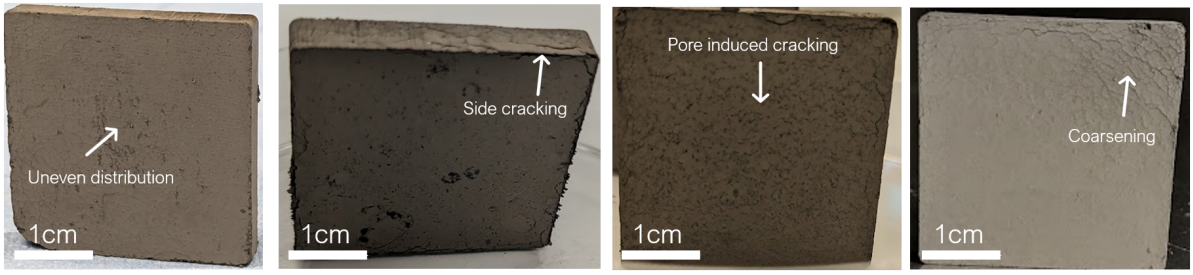

Figure 5.1: Different artifacts in sample with a pore former. In the samples: non-uniform distribution of the pores, side cracking, pore induced cracking and coarsening occur.

When the samples were kept over time (days) the samples attracted a lot of moisture inside the samples. This is illustrated in Figure 5.2.

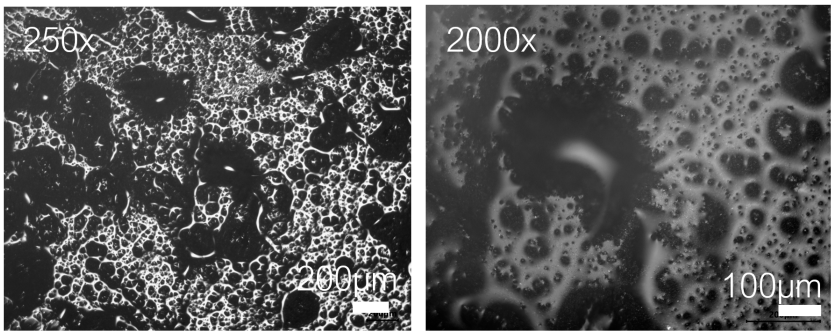

Figure 5.2: Moisture inside the samples after a couple of days.

Characterization prior to electrochemical analysis on the samples was illustrated in Figure 5.3 and Figure 5.4.

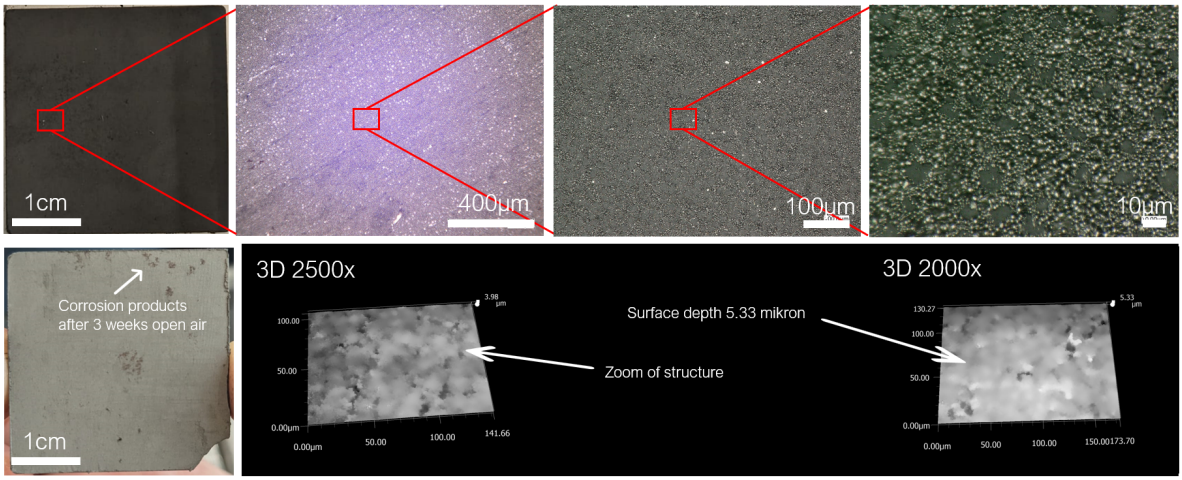

Figure 5.3: Gradual zooming onto the surface of a sample without any pore former. A flat surface is illustrated as seen as well in the 3D scans.

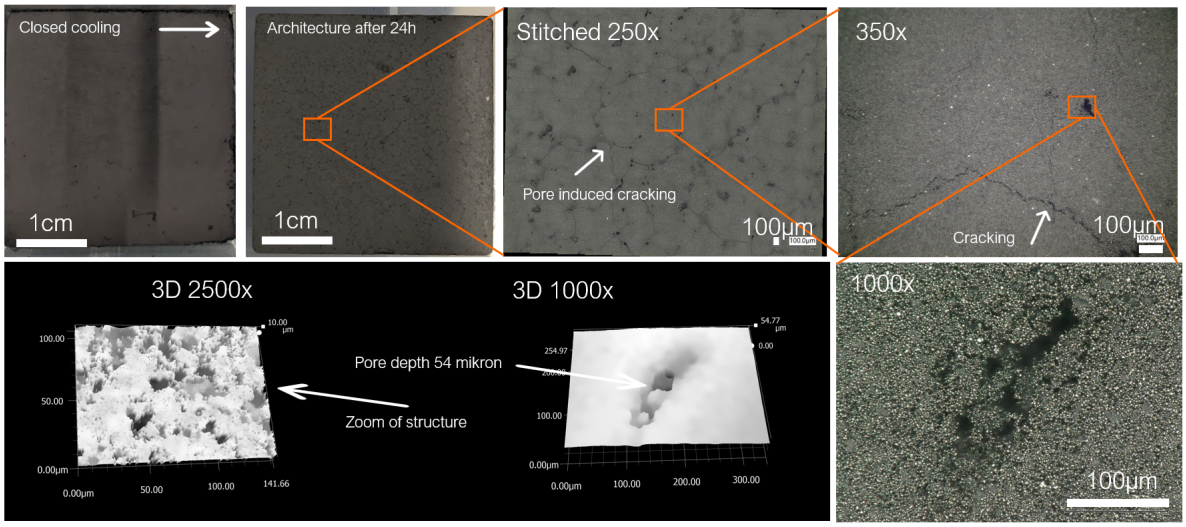

Figure 5.4: Gradual zooming on a sample with pore former. The 3D depth profile by KEYENCE on a typical pore in the size of around 200 μm has been showed. Note that this sample was cooled between Al blocks. The samples exhibited less cracking when cooled in open air, but identical morphology of the pores. An in open air cooled sample was used for porosity measurements and half- and full cell testing.

The results for long-term decomposition and cooling in open air are given in Table 5.1. From these results it can be seen that mass reduction was not achieved. In addition, from open air cooling no trend could be seen in while cooling in open air.

Table 5.1: Methodological results of vacuum drying decomposition and long term decomposition. Two samples were tested in order to check reliability.

FePEK2CO3	**1**	**2**	**FePEK2CO3**	**1**	**2**
Decomposition in oven 125°C, t=3h, p=-0.1MPa			**Cooling in open air**	1 (1h)	2 (30 min)
Mass before (g)	13.4329	13.3614	Mass before (g)	13.4189	13.4053
Mass after (g)	13.3762	13.3346	Mass after (g)	13.5066	13.3685
Difference (g)	*-0.0567*	*-0.0268*	*Difference (g)*	*+0.0877*	*-0.0368*

Hereafter porosity measurements where carried out and given in Table 5.2. Two samples were tested again in order to preserve reliability.

Table 5.2: Overview of isopropanol immersion. Comparison can be seen with a sample without pore former and with pore former.

	FePE		FePEK2CO3	
Sample	**1**	**2**	**1**	**2**
m before (g)	13.3279	13.2641	13.3181	14.0247
m after (g)	14.1004	14.0602	13.6969	14.4552
Δm (g)	+0.7725	+0.7961	+0.7066	+0.7583
Porosity (%)	28.77	29.56	26.32	28.25

Notably, the porosity differences between FePE and a sample with potassium carbonate resulted not observable differences. Also, within these measurements it was concluded that most of the observable pores were visible after open air cooling.

5.1.2. Initial Capacity Determination

In Figure 5.5, the initial discharge capacity is given. Both samples underwent one cycle to a cut-off potential of -0.55V. End stage of the samples for FePE resulted in a specific discharge capacity of 63 mAh/g and for FePEK2CO3 in a discharge capacity of around 35 mAh/g. The sample without any pore former was determined on 62 mAh/g. Notably the reduced active iron material in FePEK2CO3 should be taken into account. Assumed is that the electrolyte accessed the full depth of the sample.

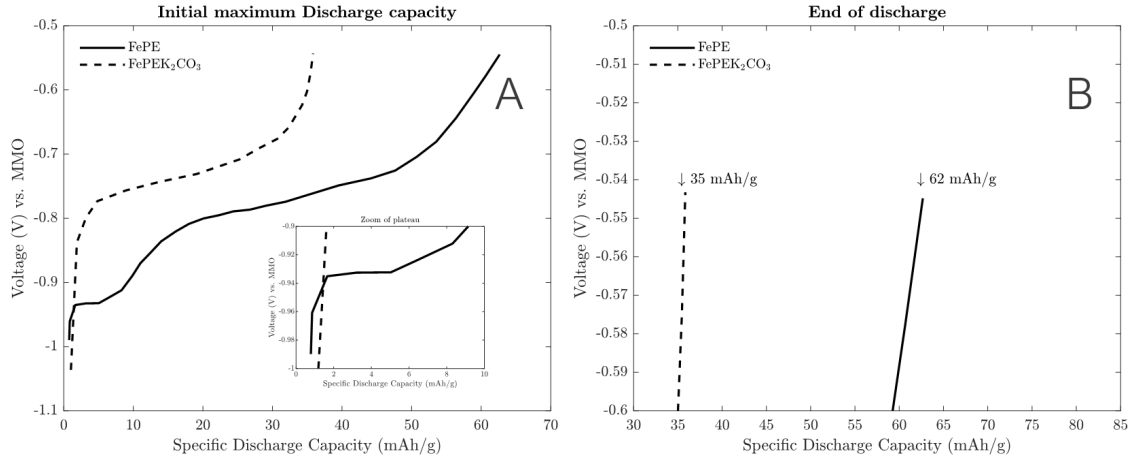

Figure 5.5: Plot of initial capacity determination of a sample with and without pore former K_2CO_3. A) shows the overall capacity trend with respect to the voltage. B) shows the end stage discharge capacities. The active material of FePE was 5.91gr and FePEK2CO3 was 5.24gr.

Table 5.3: Overview of estimated porosity and calculated DC=Discharge capacity. Second line reflects measured porosity and calculated max discharge capacity as Formula 4.5. Line 3 reflects measured porosity and measured DC.

	FePE		FePEK2CO3	
	Porosity (%)	**DC (mAh/g)**	**Porosity (%)**	**DC (mAh/g)**
Calculated	10	39	26	124
Measured/Calculated	29.17	144	27.29	132
Measured	29.17	62	27.29	35

The estimated porosity (10% for FePE and 26% for FePEK2CO3 (calculated with the density and mass contribution of potassium carbonate) and calculated (by Formula 4.5) maximum capacity are given in Table 5.3. Also the measured porosity with maximum capacities are given. In addition, the measured capacity is given.

5.1.3. Durability Test

In Figure 5.6, the discharge capacities are given for cycle 1, 3, 5, 7, 12 and 18. In the plot of cycle 18 also cycle 21 has been plotted. A clear increase in discharge capacity was observed here. All discharge capacities were equal to 2.18mA/cm^2 and lasted for 12.5h. The charge current density was equal to 5.45mA/cm^2 lasting for 5h, both ideally equating to an equivalent total capacity of 113mAh.

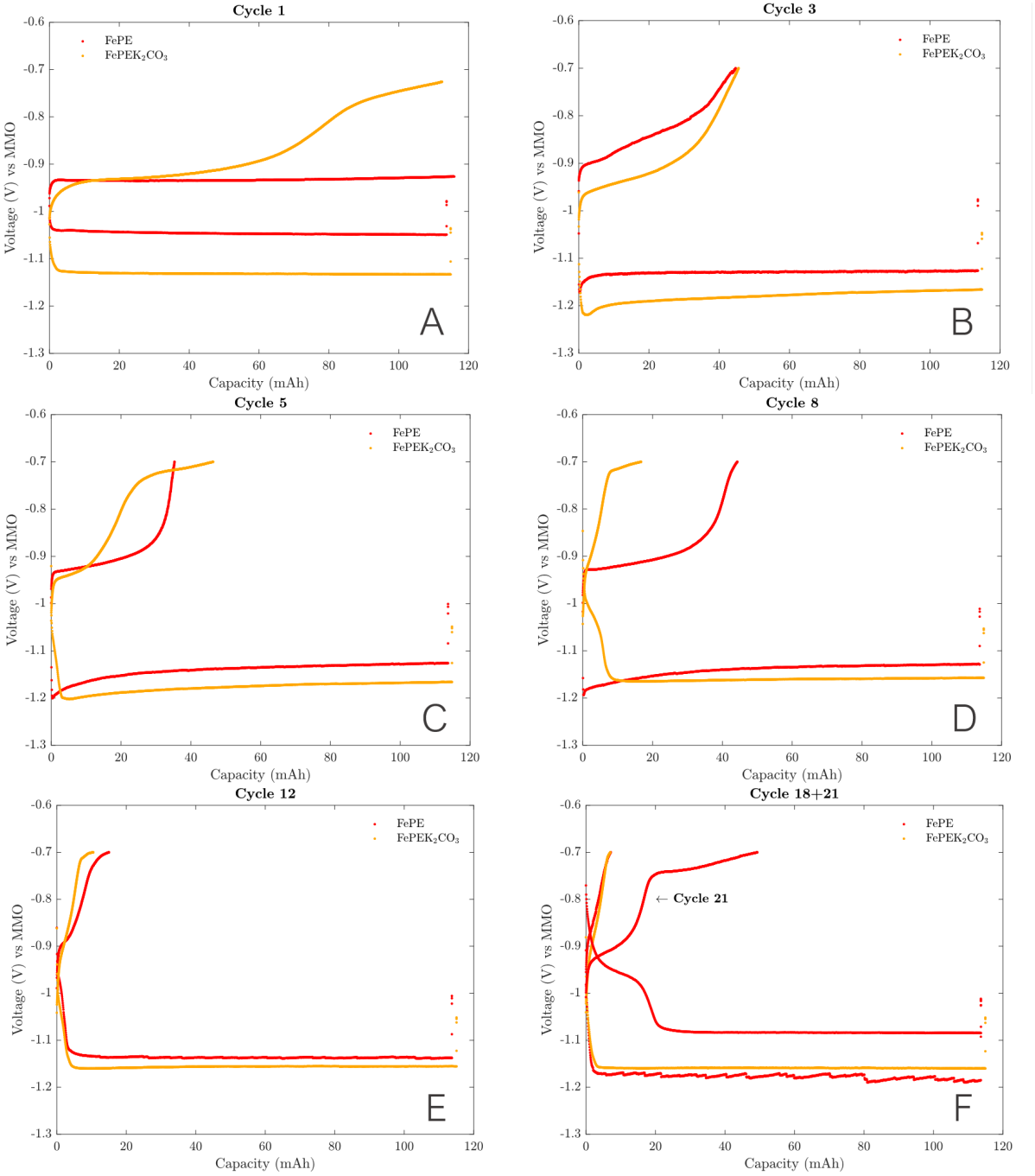

Figure 5.6: A-F) display the different cycles of the half cell tests. Cut-off potential set at -0.7V in order to prevent deep discharge. In the plot of cycle 21 an sudden increase in discharge capacity is observed in F). Note the increased active iron material for the sample FePE. In cycle 3 and 12 this had given higher specific capacity for FePEK2CO3. Also large reactivation seen in cycle 21.

We observe a fast passivation behaviour already in the third cycle in which the discharge capacities are equal. In cycle 5, the discharge capacity is slightly higher than the sample without any pore former. In cycle 8 the difference was the largest up to 23mAh difference, from which the difference diminished

again and became almost equal in cycle 18. The sample without any pore former showed an capacity increase again in cycle 21, which was not observed for the sample with pore former.

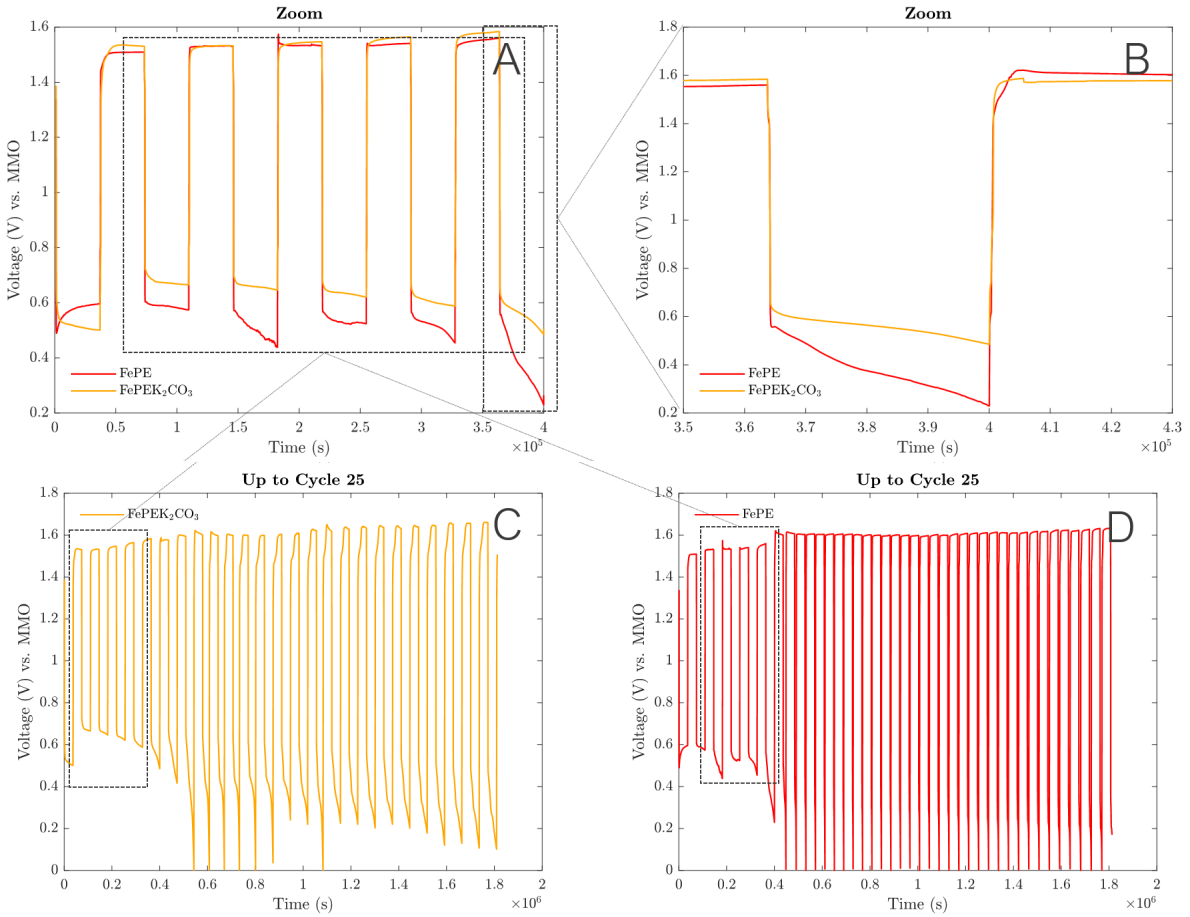

Figure 5.7: Full cell test results of the sample with and without any pore former. In A) reflection of the first five full cycles. B) is a shift in the potentials upon discharging in the fifth cycle. C) and D) reflect the cell potentials during the first 25 cycles. The full cell tests for FePE and FeK2CO3 were also extended after 25 cycles in which FePE continued its behaviour without any discharge capacity for many cycles and FePEK2CO3 increased its discharge capacity with 100% for another 12 cycles. Only the first 25 cycles are given here.

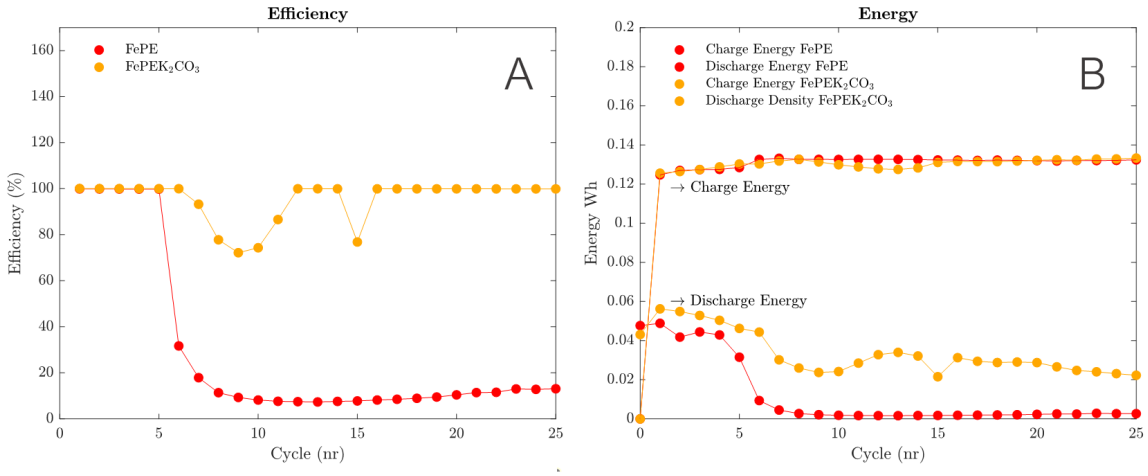

Figure 5.8: Overview of the efficiency (%) and energy (Wh) for the samples with and without pore formers.

5.1.4. Post-Test Characterization

In Figure 5.9 and 5.10, the surface is illustrated for the samples after 20 cycles of galvanostatic charging and discharging (in (almost) fully charged state). Most importantly, we observe some loss of active iron material in the sample within the sample with pore formers and alongside the pore, much cracking was observed. Note that the samples after full cell performance were not given, but showed a highly roughened stable surface on the sample with pore former and a stable flat surface/slightly roughened after testing (FePE in fully charged state, FePEK2CO3 in predominantly discharged state).

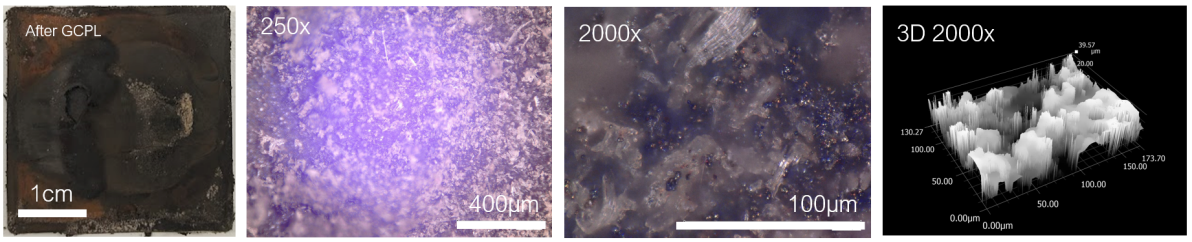

Figure 5.9: Sample structure of a sample with initial composition FePE architecture on a cycled sample after durability test. Images are from regular camera and KEYENCE microscope.

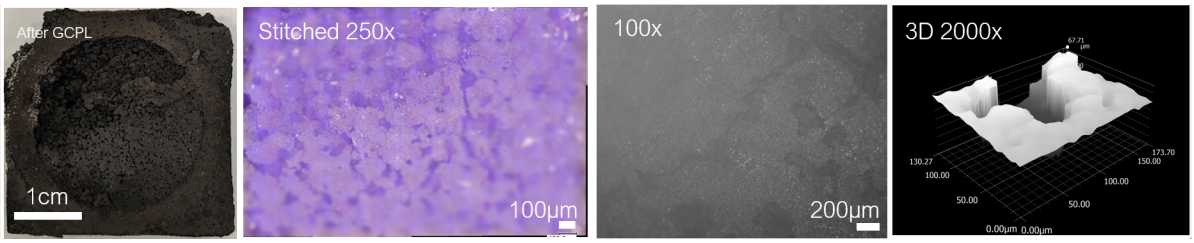

Figure 5.10: Sample structure of a sample with initial composition FePE and pore former K_2CO_3 architecture on a cycled sample after durability test. Images are from regular camera and KEYENCE and OMAX micrscope.

5.2. Additives studies

In this Section, the results on Additive studies will be revealed. Pre-Test characterization, Electrochemical Analysis and Post-Test microstructural analysis will be given.

5.2.1. Pre-Test Characterization

At first the porosity measurements for the samples with the additives will be given. For reliability, each time two samples were given. In Table 5.4, the obtained porosities were given. Porosities were measured in between approximately 15 and 30 %. This was considered relatively low.

Table 5.4: Porosity measurements of the samples with CIP, PE and additive.

Immersion	**Bi_2S_3**		**Bi_2O_3**		**ZnS**		**FeS**	
Sample	**1**	**2**	**1**	**2**	**1**	**2**	**1**	**2**
m before (g)	13.2685	13.3274	13.2706	13.2362	13.2136	13.4077	13.7401	13.3873
m after (g)	13.71	13.7122	13.8050	13.7582	14.0347	14.2234	14.2244	14.1846
Δm(g)	*0.4415*	*0.3848*	*0.5344*	*0.522*	*0.8211*	*0.8157*	*0.843*	0.7973
Porosity (%)	16.45	14.33	19.91	19.44	30.58	30.38	31.40	29.70

In Figure 5.11, the results for profilometry are given. No clear differences are given by the profiles. The average values plus their mean absolute error is given in Table 5.5.

Table 5.5: Overview of average values with mean absolute error per sample with different additives. More roughness values are given in Table B.1.

	FePE	**Bi_2S_3**	**Bi_2O_3**	**ZnS**	**FeS**
Av. roughness	1.58±0.10	1.09±0.03	1.30±0.15	1.61±0.09	1.04±0.12

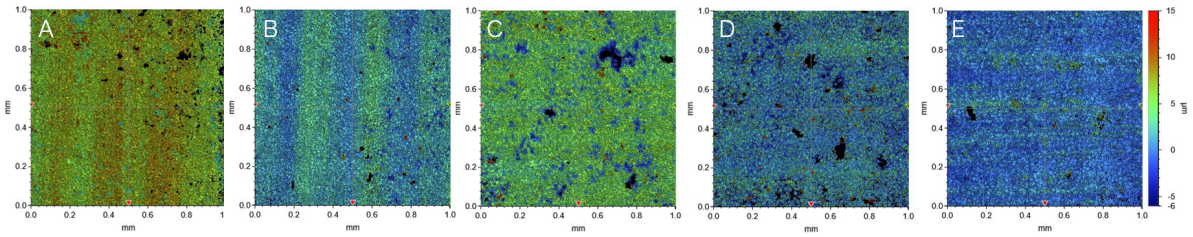

Figure 5.11: Profilometry results for given by BRUKER interferometer before electrochemical testing. All stitched areas of 1mm by 1mm were measured 3 times. A) FePE B) Bi_2S_3 C) Bi_2O_3 D) ZnS E) FeS.

In Figure 5.12, the initial particle sizes are illustrated. The powders containing bismuth sulfide and iron sulfide were determined as the largest and most brittle particles. In image A) on the left the largest particle can be seen as bismuth sulfide chunks were observed from the powders, which were grinded to a size equal to 100 μm $\pm$ 300 μm after grinding. Iron sulfide in image D) shows relatively large particles and sizes of a maximum around 400 μm. In Image B) predominantly agglomerations were observed of soft powders, since the powder size of bismuth oxide was stated as a maximum of around 10 μm and higher sizes were measured of around 300 and 400 μm even. In Image C) the smallest particles were observed, most closely to their mentioned particle size of around 10 μm, but still with their original size before mixing of around 100 to 200 μm. The observations were done without observing the effect of mixing, but it was assumed that the amount of agglomerations diminished and was observed by SEM which confirmed particle sizes of 10 μm for ZnS.

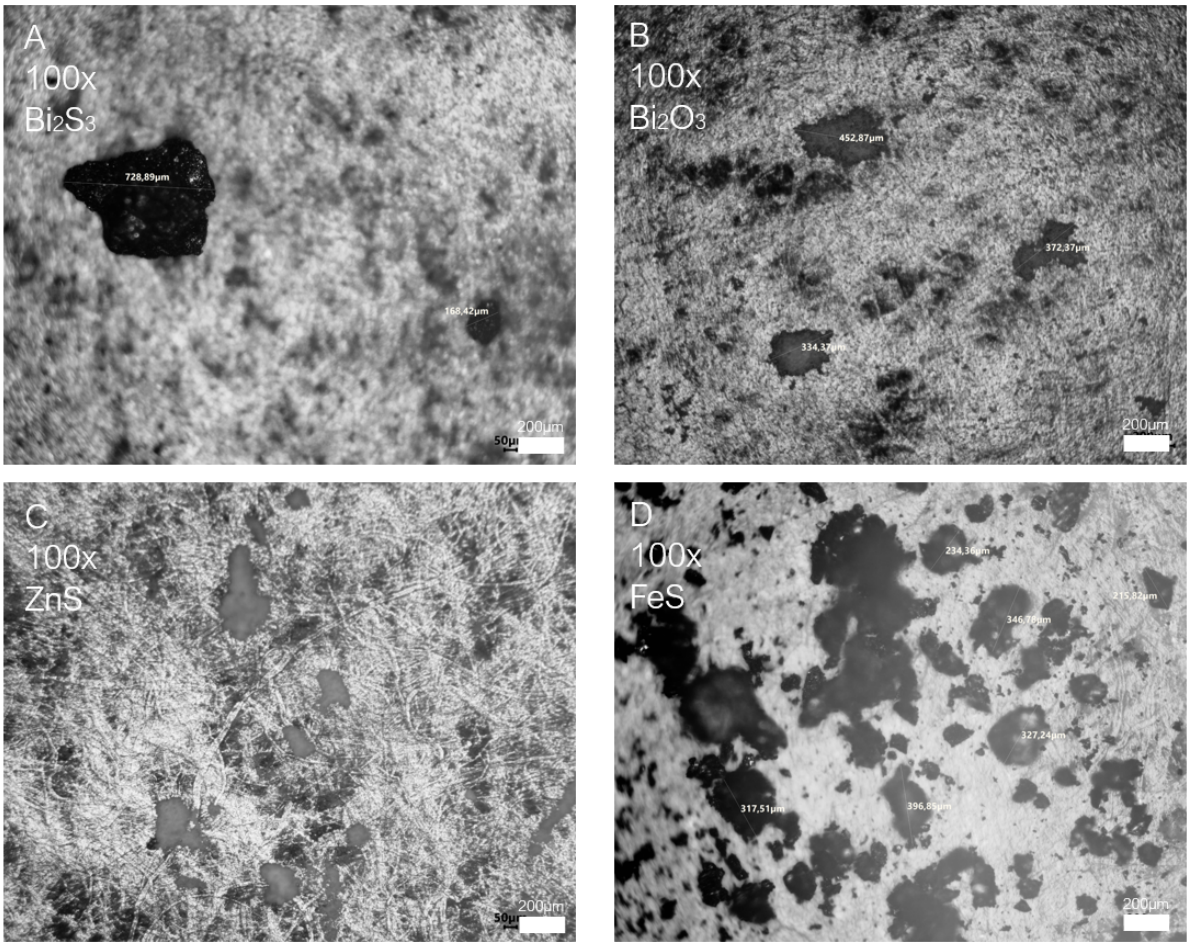

Figure 5.12: Overview of powders before mixing and their particle size or agglomerations. Images are obtained with OMAX optical microscope. A) reflects bismuth sulfide, B) bismuth oxide, C) zinc sulfide and D) iron sulfide.

In Figure 5.13, 5.14, 5.15 and 5.16, the samples prior to electrochemical testing are illustrated. It was observed that the overall depth was almost equal for all samples. Although the porous structure in the samples with the relatively larger particles was less dispersed and exhibited larger pores. Depth was measured up to a rounded value of 10, 11, 13 and 12 μm for the samples with bismuth sulfide, bismuth oxide, zinc sulfide and iron sulfide. Pores for the samples with bismuth sulfide and iron sulfide were bigger up to 75 μm. The pores for the samples with bismuth oxide and zinc sulfide exhibited pores in the size of a maximum of around 50 μm. Note that the illustrations given were not identical for all sections, but the behaviour showed this trend of a more non-uniform distribution of larger pores for the samples with bismuth sulfide and iron sulfide.

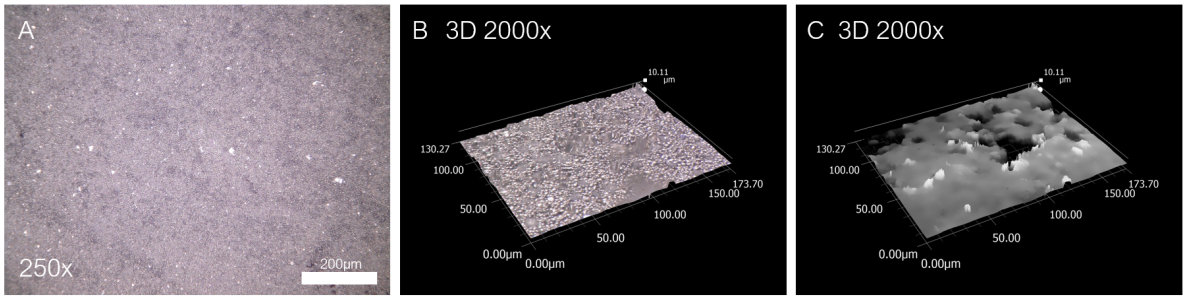

Figure 5.13: Representation of KEYENCE images of different magnifications of pre-tested surfaces of the samples with additives. A) Flat surface, magnification 250x of bismuth sulfide. B) 3D image of surface, magnification 2000. C) 3D monochrome plot to observe the depth of the sample better. Note that for the sample with bismuth sulfide also areas were found with flat surface (indicating the absence of the relative larger additive particle).

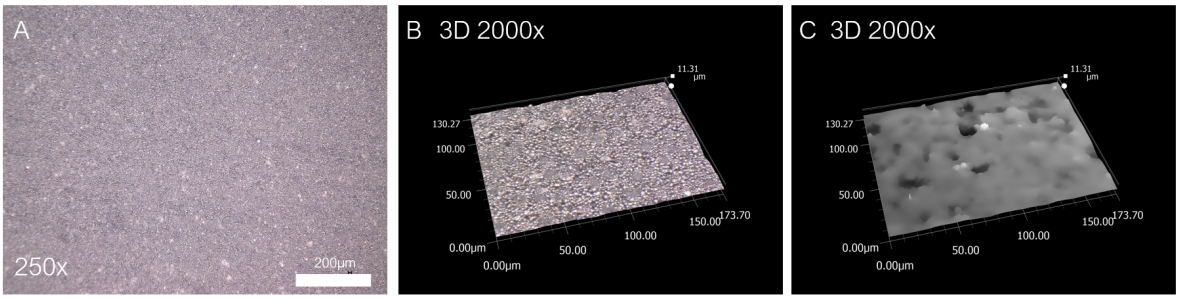

Figure 5.14: Representation KEYENCE images of different magnifications of pre-tested surfaces of the samples with additives. A) Flat surface, magnification 250x of bismuth oxide. B) 3D image of surface, magnification 2000. C) 3D monochrome plot to observe the depth of the sample better.

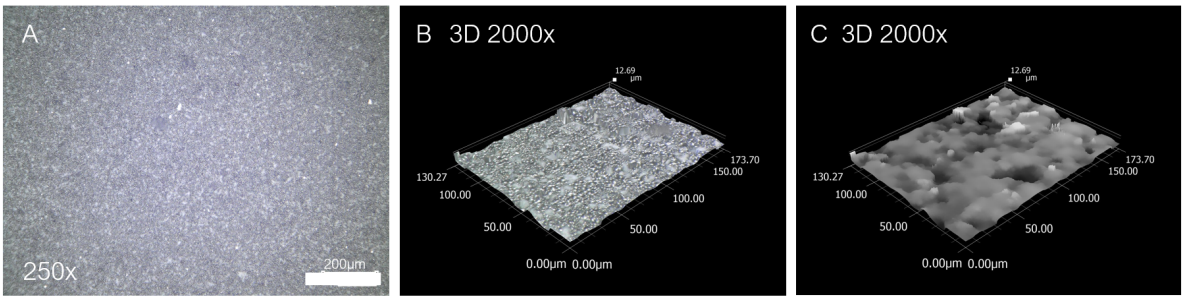

Figure 5.15: Representation of KEYENCE images of different magnifications of pre-tested surfaces of the samples with additives. A) Flat surface magnification 250x of zinc sulfide. B) 3D image of surface, magnification 2000. C) 3D monochrome representation to observe the depth of the sample better.

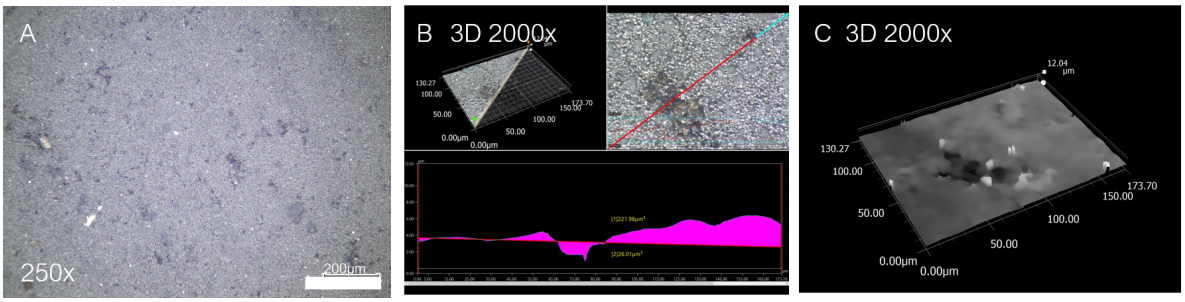

Figure 5.16: Representation of KEYENCE images of different magnifications of pre-tested surfaces of the samples with additives. A) Flat surface mag 250x of iron sulfide. B) 3D image of surface magnification 2000. C) 3D monochrome representation to observe the depth of the sample better. Note that for the sample with iron sulfide also areas were found with flat surface (indicating the absence of the relative larger additive particle).

5.2.2. Kinetic Studies by Cyclic Voltammetry

FePE In Figure 5.17A and B, the performed CV is given for a pristine sample without any additives. All repetitions were in adequate agreement with each other, confirming consistency in the cyclic voltammograms. Remarkable was the absolute value of the current densities which might deviate slightly.

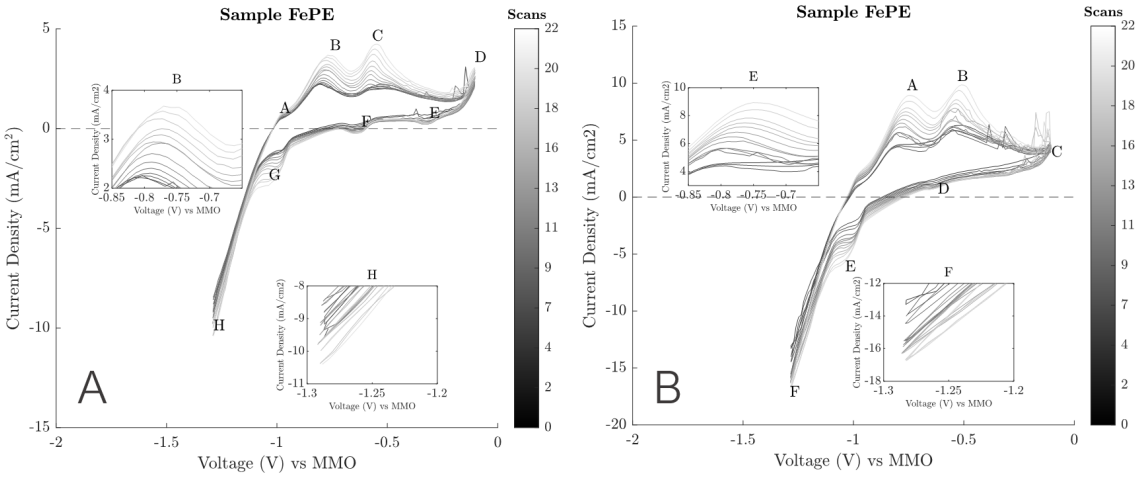

Figure 5.17: Cyclic voltammogram of pristine sample hot-pressed at 150^{o}C for 10 min at 88MPa. Note that the sample was almost completely dissolved after CV. Note as well that the active iron material was higher for a sample with FePE compared to the samples with additives.

The first given cycle was the 6th cycle and the last is the 20th. The first 5 cycles had to be disregarded because of their high currents without proper identifiable peaks and couldn't lead to adequate examination of the electrochemical thermodynamics and/or kinetic behaviour. This late conditioning can be assigned to the wetting process of the iron anode and diffusional limits caused by the powder nature of the iron electrode.

The detailed observation for a cyclic voltammogram on FePE will be elaborated. All observable peaks are assigned to the letters A, B, C, D, E, F, G and H. In all cases, with increasing cycle number, current densities intensified, hinting at the activation within the anode. Since the oxidation peaks were better identifiable than the reduction peaks, the peaks with respect to their theoretical values were examined, corresponding to 0.2V off the theoretical value for the peaks A, B and C. It is stated in literature that peak A is ascribed to the first intermediate step Fe/Fe(I) in the conversion Fe/Fe(II). In literature it was also stated this could also be related to the oxidation of hydrogen gas, but that it was rather believed to reflect Fe/Fe(I) conversion.

Peak B reflects the conversion Fe(0)/Fe(II) and between cycle 6 and 20 shows an increase in current density from 2mA/cm2 to 3.6 shifting its potential from -0.82V to -0.77V highly probable indicating

its increased activation energy to successfully oxidize active iron material of iron to its oxidized state since the discharge capacity is much higher than the charge capacity (both in the first cycle as the last cycle).

Peak C might show the conversion of Fe(II)/Fe(II,III) or the conversion from Fe(II)/Fe(III). In the 6th cycle, these peaks assigned to C are separately identified at -0.56V and -0.47V as two low peaks, whereas one centralized peak occurs not far (+0.02V) from the left low peak in cycle 6. In the most positive value of the potential range, peak D might be assigned to the capacitive current since the potential is largely separated from any occurring redox equilibrium potential.

Peak E and F both show some current dips. The current dip in the positive current range in the cathodic direction during all scans is remarkable here. In peak F in cycle 6 the peak starting at a current density of 0.22 mA/cm^2 and ending in cycle 22 at a current density of -0.22 mA/cm^2 might either reflect some processes coping with desorption or absorption. Another possibility here is a net positive current while reduction of Fe(II,III)/Fe(II) or Fe(III)/Fe(II) occurs.

Peak G can be assigned to the Fe(II,III)/Fe(II) or Fe(III)/Fe(II) conversion or the Fe(II)/Fe(0) conversion and is located in the 6th cycle at -0.98V gradually decreasing to -1.05V with increasing current density of 1.16mA/cm^2 to 2.86mA/cm^2 in cycle 20. In the first case of only Fe(II,III)/Fe(II) or Fe(III)/Fe(II) conversion, the increased C peak over cycles and not identically in value increasing peak B, can come from the fact that more iron hydroxide is present and available for Fe(II)/Fe(II,III) conversion in the oxidation direction since no reduction of Fe(II)/Fe(0) is identified. In the case of only Fe(II)/Fe(0) and the overlapping peak H, it might be the case that effectively less Fe(II) is converted back to Fe(0), therefore confirming the intensification of FeOOH/Fe_3O_4 development. Considering the large peak-to-peak distance for C to G (around 0.5V difference) for the last cycle, it is more probable that it is assigned to the conversion Fe(II)/Fe(0). Peak-to-peak separation of B and G is -0.27V and C to F is -0.09V in the last cycle (20).

In the case that F belongs to Fe(II)/Fe(II,III) and Fe(II)/Fe(III) and G to Fe(0)/Fe(II), peak current ratios can be determined for B-G: i_{pC}/i_{pA}=1.16/2.17=0.53 for the first cycle and i_{pC}/i_{pA} =2.86/3.68= 0.77 for the last cycle means an increase in reversibility in that conversion. For C-F yields: i_{pC}/i_{pA}=0.22/1.97= 0.11 (6) and for the last cycle (20) equal to i_{pC}/i_{pA}=0.24/4.24= 0.06 referring to an reversibility reduction.

Considering the steep high current density peak at -1.3V and observation of gas formation inside the cell, the peak H is assigned to the hydrogen evolution. In cycle 6, the current density is -8.4 mA/cm^2 and in cycle 20 this even increased to -10.37 mA/cm^2. The slopes in in sixth cycle can be determined at 40.54 and in the 20th cycle at 41.27 hinting at an ongoing increase in HER upon further cycling. The total discharge Q is higher than the charge capacity Q.

Bi_2O_3 and Bi_2S_3 In Figure 5.18A, the performed CV is given for a sample with the additive Bi_2S_3. Again, the first couple of cycles needed to be disregarded due to its reactive behaviour. The first to be obtained cycle was stated in cycle 7. It can be observed than within this sample, no clear sharp observable peaks can be identified. It was also observed during the CV of this sample, that additive dissolved to a large extent into the electrolyte by a visible yellow color change.

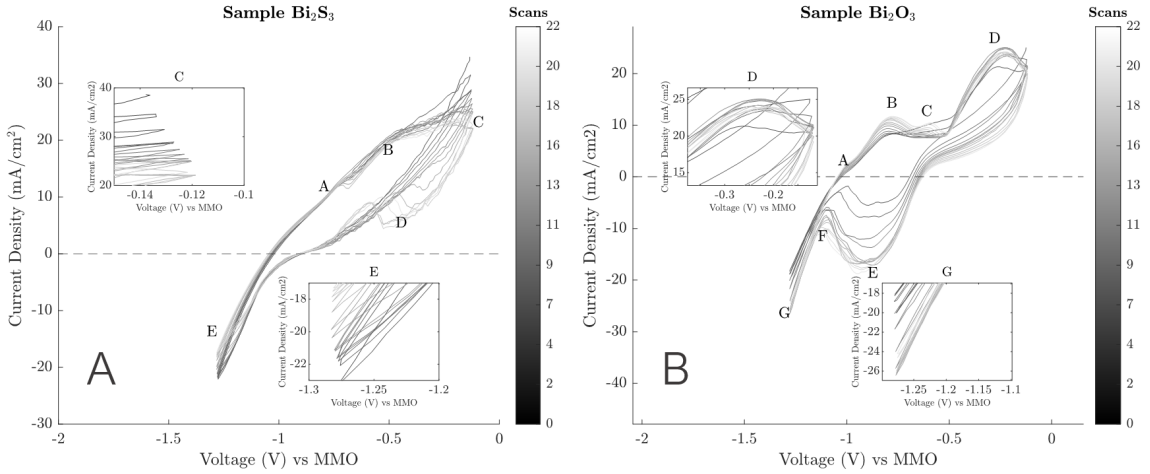

Figure 5.18: Cyclic voltammogram of sample with bismuth sulfide A) and bismuth oxide B) hot-pressed at 150^{o}C for 10 min at 88MPa.

No Fe(0)/Fe(I) or Fe(0)/Fe(II) conversion was observed at a defined peak during linear increase of the potential, but it might be believed that peak A can be accounted for Fe/Fe(II) conversion which became visible in cycle 18.

Peak B might be is reflecting, conversions of Fe(0)/Fe(II) but more probable the conversion Fe(II)/Fe(II,III) or Fe(II)/Fe(III). Peak B (more a shoulder) at a potential -0.46V with current density at 21.64mA/cm^2 in cycle 7 shifted a bit to the left in cycle 20 at -0.50V with current density 19.83mA/cm^2. This delayed peak B with respect to theoretical values can be due to diffusion limits enhanced by ion migration blocking by the larger bismuth sulfide particles.

At very high potentials with respect to the expected equilibrium potentials of Fe(0)/Fe(II) and Fe(II)/Fe(III) or Fe(II)/Fe(II,III) peak C appears from which the potential is delimitated by its potential window at -0.1V. The current decreases over cycle 7-20 from 31.22mA/cm^2 to 22.33mA/cm^2. Further in the cathodic direction no clear reduction peaks were identified. This can be either to high resistance within the system causing linear I-V relationships.

Peak D is what has been identified earlier as a current dip in the cathodic direction indicating some anode surface modifications. Note that no negative reduction peaks were observed for the anode with bismuth sulfide as additive, which might be assigned to passivation/ongoing discharge process even in the cathodic direction, since the currents still reflect an net current. D decreases between cycle 15-20 from a potential peak at -0.37V to -0.54V and the current density decreased from 11.31mA/cm^2 to 4.43 mA/cm^2. It might reflect Fe(II,III)/Fe(II) or Fe(III)/Fe(II) conversion.

Point E shows a large reduction in current develops after the 7th cycle. Between the 7th and the 20th cycle a reduction of around 4.81mA/cm^2 (from -22.0788 to -17.27 in the position -1.3V) occurred in peak E and a reduction in slope of HER from 130.93 to 95.701 was linearly determined in the peak E at -1.3V. The sole contribution of hydrogen reduction at this potential can not only be assigned to HER but might also reflect the reduction of bismuth sulfide at a potential of around -0.92V or the reduction of in situ formed FeS at a potential of around -1.07V.

During further quantitative analysis, peak-to-peak separation was determined, the peak current ratio was obtained and the anodic charge and cathodic charge were analyzed as well. Contrary, to the experiment without any additive as discussed before, no clear observable peaks were observed and therefore also no corresponding anodic and cathodic peaks. The peak-to-peak ratio was given for i_{Cp}/i_{Ap} B-D. For cycle 7, the peak B corresponded to -0.47V at a current density of around 21.64mA/cm^2 shifted to -0.50V at 19.83mA/cm^2 in cycle 20. For peak D it started in cycle 15 at a potential of -0.34V to -0.52V in cycle 20 and decreased its current density from 11.30mA/cm^2 to 4.43mA/cm^2. Since the currents were still positive, the ratio was not calculated.

Clearly, the anodic charge is much higher than the cathodic charge revealing an increased discharge capacity, from which the discharge/charge capacity ratio stays the same (both reducing, might be due to passivation). This can be assigned to loss of sulfide ions.

In Figure 5.18B, the curve is stated for anode with CIP iron particles, PE and Bi_2O_3. Again the same experimental conditions are applied in the measurement. In these curves, much more defined peaks are observed. Here, it was necessary again to eliminate the first cycles, because of some formation, electrolyte migration, wetting and conditioning of the electrode-electrolyte interface. The first cycle at which clear peaks could be read was in the 8th cycle. Overall, it can be directly remarked that some defined peaks occur in the cathodic direction, in contrast to the other cyclic voltammograms of the pristine sample and the sample with bismuth sulfide.

The peak A at position -1.01V and current density 2.09mA/cm^2 in cycle 20 hints probably at the conversion Fe(0)/Fe(I), equivalently as in the CV for the pristine sample at the same potential (-1.005V for both). Over time this peak remains relatively constant in peak potential and current density. Peak B is located at a peak potential of -0.79V and shifts over the time span to a potential of -0.788V in the 20th cycle. In addition, the current density increases from 8.29mA/cm^2 to 11.65mA/cm^2. In peak C we observe a peak shift and current density intensification from approximately the same order of magnitudes as in peak B. In cycle 8 the voltage was read from -0.61V at a current density of around 8.09mA/cm^2 which shifted to -0.58V at a current density of 10.41mA/cm^2. This peak C probably reflects the conversion Fe(II)/Fe(II,III). In peak D, a large amplification is observed in current density already at cycle 8. In this potential range (-0.25V to -0.21V) the peak potential is gradually increasing from cycle 8 around 23.58mA/cm^2 (at -0.21V) and from its maximum in cycle 16 (at -0.23V) at 24.80mA/cm^2, reducing again to 24.10mA/cm^2 in the last cycle. This peak located at D reflects probably the conversion of Fe(II)/Fe(III).

In addition to that reaction occurring with this large anodic charge, also an oxidation of Bi_2O_3 might be present here for which the equilibrium potential is -0.56V increasing the current density even higher at that potential. At the end of the potential range, peak D was slightly reduced compared to how it was increased in current density, whereas in the cathodic direction, a smooth reduction peak was observed. Peak E can be assigned to the reduction of Fe(II,III)/Fe(II) or Fe(III)/Fe(II). Here, the largest cathodic peak has been observed compared to all other cyclic voltammograms. Peak-to-peak separation of D and E is determined in the 20th cycle of (-0.25V to -0.95V) -0.70V and in the 11th cycle from -and a cathodic peak to anodic peak ratio was given as i_{Cp}/i_{Ap} is the 11th cycle: 5.01mA/cm^2/23.58mA/cm^2=0.21 and in the 20th cycle: 18.73mA/cm^2/24.10mA/cm^2=0.78 clearly showing a gradual doubling of reversibility for that redox reactions. Note that the cathodic peak in cycle 11 from peak E was slightly shifted with a value from around -0.12V if it belongs to the same redox reaction.

Between peak E and F some indication can be found of reduction of Fe(II,III)/Fe(II), Fe(III)/Fe(II) and Fe(II,III)/Fe(0), but was complicated to state and assign specific peaks to specifically that reaction. The scattered data reflects some reactive behaviour translated into unidentifiable peaks within the CV. The peak in position -0.89V at current density -5.50mA/cm^2 could reflect the conversion Fe(II,III)/Fe(II), Fe(III)/Fe(II) in the 8th cycle. The more broad peak could represent more than one conversion/peak that could be assigned to the reduction of Fe(II,III)/Fe(II), Fe(III)/Fe(II) and Fe(II)/Fe. In cycle 15 which was between the peaks of E and F at a potential of around -1.00V at current density -16.11mA/cm^2 shows that one broad peak.

Peak E can reflect the reduction associated with the oxidation of peak D (and C). The peak in cycle 8 around -0.82V at current density -5.01mA/cm^2 could be assigned to the conversion Fe(II,III)/Fe(II) or Fe(III)/Fe(II) but it was difficult to state clearly. The peak located in can be assigned to a peak position of -0.95V at a current density of -18.73mA/cm^2 in cycle 20. This is probably reflecting the reduction of Fe(II,III)/Fe(II) or Fe(III)/Fe(II). The peak-to-peak separation for D to E was stated as a value of -0.7V in the 20th cycle. An cathodic peak to anodic peak ratio was given as i_{Cp}/i_{Ap} is the 11th cycle: 5.01mA/cm^2/23.58mA/cm^2=0.21 and in the 20th cycle: 18.73mA/cm^2/24.10mA/cm^2=0.78 indicating the amplification of reversibility over the cycles as well.

Peak F can reflect the reduction associated with the oxidation of peak B (and C). At cycle 8, at a potential around -0.97V at current density -3.14mA/cm^2 the corresponding peak could be reflected to Fe(II)/Fe(0) but it was difficult to state clearly. A peak located in F can be assigned to a peak position of -1.07V at a current density of -13.89mA/cm^2 in cycle 20. This is probably reflecting the reduction of Fe(II)/Fe(0), corresponding to peak B. The peak-to-peak separation for B to F was stated as a value of -0.17V in the 20th cycle. An cathodic peak to anodic peak ratio was given as i_{Cp}/i_{Ap} is the 8th cycle: -3.14mA/cm^2/8.27mA/cm^2=0.22 and in the 20th cycle: 13.89mA/cm^2/11.65mA/cm^2=1.19 indicating the amplification of reversibility over the cycles as well.

The steep curve in G is assigned to HER equivalently as the other CVs enhanced by clear gas formation of this potential range. Current increases in 12 cycles from a current density of -18.10mA/cm^2 to -24.15mA/cm^2 in the 20th cycle. Note that in earlier cycles even lower current densities are measured up to a value of around -27mA/cm^2 at the potential of -1.28V. The slopes in this potential range at -1.3V were found as 112 in the 20 cycle while in the 8th cycle the slope was equal to 84 which means an increase of a slope of 28 in the HER equilibrium potential range. This was a large increase with respect to the sample without any additives.

This was not expected – knowing the reduction potential of Bi_2O_3 at -0.56V vs MMO – able to deposit bismuth on the electrode which might effectively suppress HER. Instead, it is observed that bismuth deposition has effectively reduced stable iron hydroxide and iron oxide, while also decreasing the overpotential with respect to the equivalent peak E for a pristine sample reflecting the conversion Fe(II) to Fe(0) which is much more bounded to the hydrogen peak. The electrochemical catalytic effect might be due to the electronic structure change effectively absorbing iron ions at the surface.

It might be caused that the effective reduction of iron oxide or hydroxides increase conductivity of the electrode which might also reflected in an increase in HER, catalyzed by active iron material increase and thus electrical conductivity increment. In addition, a coverage of active iron material of iron formation after bismuth deposition might reduce the active iron material of bismuth. The catalytic effect of bismuth oxide will be discussed further in the Discussion section. It might also be that the HER was intensified here.

ZnS and FeS In this paragraph the cyclic voltammogram of a sample with the addition of ZnS will be given as seen in Figure 5.19A. Notably, the equilibrium potential of ZnS is outside the applied potential range. In these scans, the 3th cycle was considered the first valuable scan and the 19th scan was again considered as the last scan. In these graphs in the cathodic direction, some small dips are again observed, while the overall net current is still positive. It was not expected in these curves thus, to obtain some reduction peak for ZnS, but we might suspect some reduction in the evolution of gas.

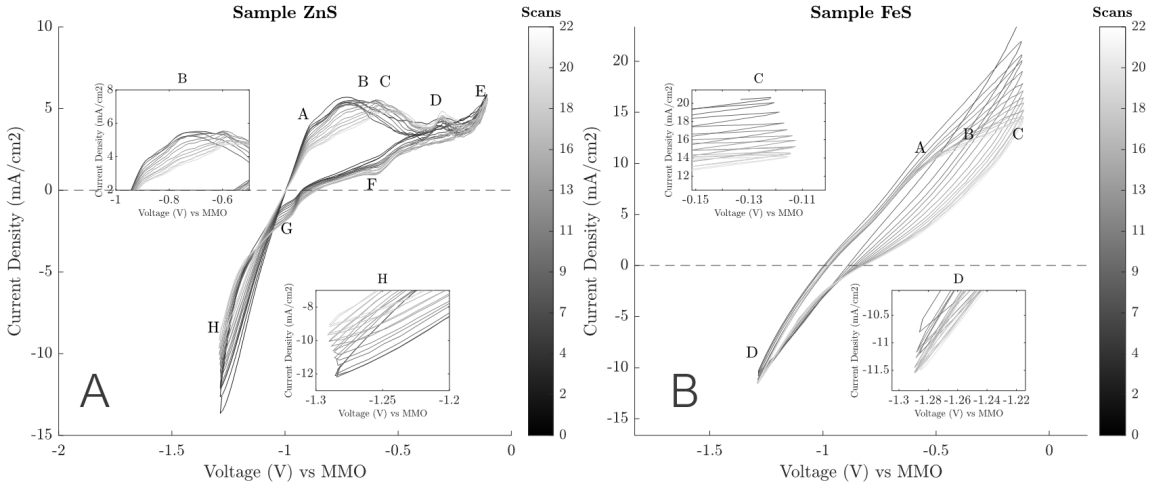

Figure 5.19: Cyclic voltammogram of sample with zinc sulfide A) and iron sulfide B) hot-pressed at 150^{o}C for 10 min at 88MPa.

Peak A which is slightly shifted to the right with respect to the CVs of FePE and Bi_2O_3 can be reflecting the Fe/Fe(I) conversion. It can be observed that this peak is increasing from 2.46mA/cm^2 to 3.75mA/cm^2 and that the peak position stays rather at the same position (-0.88V). Since this peak is slightly more shifted to positive values, it might also be considered that this peak is the Fe/Fe(II) peak with less overpotential than measured in the other cyclic voltammograms.

Peak B can be associated with either the conversion Fe/Fe(II) or the conversion Fe(II)/Fe(III) and is located in the 3th cycle at -0.74V at a current density of around 5.68mA/cm^2. In the latter case, peak C should be assigned to the conversion Fe(II)/Fe(III). It was showed that upon cycling this peak A, B and C reduced in magnitude and all shifted to more positive potentials hinting at the phenomenon of passivation when more activation energy (potential) is needed to drive this current. It was complex to assign which peak shifted to what extent to more positive values, but in cycle 19 the current density was given at 4.94mA/cm^2 at a potential of -0.52V. Considering that the conversion Fe/Fe(I) should always give a smaller peak it is plausible to state that peak A is equal to Fe/Fe(II) conversion, B to Fe(II)/Fe(II,III) conversion and C equal to the Fe(II)/Fe(III) conversion. All peaks shift to the peak of C and even more positive than C at the assigned values.

In D and E some data is acquired but could not be assigned easily. D is located in cycle 19 at a position of -0.31V at a current density of 4.67mA/cm^2. In E, the value remained relatively high, at a position of -0.11V with a current density of 5.62mA/cm^2 through all cycles. In peak F in cycle 3 the position was -0.57V with a current density of around 2.07mA/cm^2, and in cycle 19 the position was around -0.59V with a current density of around 0.99mA/cm^2. This dip in the cathodic sweep can be assigned to an ongoing oxidative behaviour in the high potential range. This peak F can be assigned to reduction of Fe(III)/Fe(II) or Fe(II,III)/Fe(II) conversion. Notably, the reduction is much lower compared to the oxidation of corresponding conversions.

In peak G the reduction might be observed as the Fe(II)/Fe(0) conversion at a potential in cycle 3 equal to -0.94V with current density 0.31mA/cm^2 and in cycle 19 increasing to a value of 1.56mA/cm^2. Since this peak is near the hydrogen evolution peak in H, it can overlap with that peak and therefore observed more in 'shoulder'-shape. Within the qualitative analysis, peak-to-peak distance and cathodic charge and discharge ratios can be calculated. Considering that A belongs to G and C belong to F. The peak-to-peak distance can be determined for A-G equal to -0.06V in cycle 3 and -0.08V in cycle 19. For C-F it was hard to determine the peak-to-peak ratio in the beginning because of scattering behaviour. In cycle 19, it was determined at -0.07V. An cathodic peak to anodic peak ratio was given as for G/A i_Cp/i_Ap is the 3th cycle: 0.31mA /cm^2/2.46mA/cm^2=0.13 and in the 19th cycle: 1.56mA/cm^2/3.75mA/cm^2=0.42 confirming amplification of reversibility over the cycles as well. For F/C this was not easy to calculate because of the positive reduction current.

The peak H can be assigned to the HER in consistency with the other experiments and cyclic voltammograms. In this case the current at potential value -1.3V decreases between cycle 3 and 19 from -12.195mA/cm^2 to a value of -9.06mA/cm^2. The slope of the HER is equal is cycle 3 to: 38.17 and in cycle equal to 26.81 which means a reduction of 11.36 in the current density at the location of HER. Remarkable was here the shape of the curve descending in the cathodic direction and crossing its own value. This happened also for the repeated measurements. Note that the HER is not evaluated as a peak.

In Figure 5.19B, the cyclic voltammogram of a sample with FeS is given. Only the last couple of cycles are given again, since the behaviour was very reactive in the anodic direction. The peaks obtained are stated as A, B, C and D. Equivalent to the sample with Bi_2S_3 as additive, a large resistance within the CV is measured as a linear behaviour. No colour change was observed within the system, confirming the bismuth compound in bismuth sulfide to be responsible for such a colour change. In addition, the discharge capacity is much large than the charge capacity, indicating reactive behaviour with large capability to oxidize.

Peak positions of A, B and C are measured at a potential according the following explanation. A starts in cycle 6 at a potential of -0.57V at a current density of 11.14mA/cm^2 and ends in cycle 21 at a potential of -0.56V a and current density of 9.63mA/cm^2. The potentials and currents are described of peak B which is not clearly assigned as a peak. Although the evolution of the curve is interesting to state as a slight shoulder in the curve. Shoulder B in cycle 6 is located at -0.35V at a current density of 16.67mA/cm^2. In cycle 21 this reduces to a potential of -0.37V at a current density of 11.75mA/cm^2. In peak C the the peak is located at -0.13V at a current density of 24.42mA/cm^2 in cycle 21 and decreases to a position at -0.12V at a current density of 14.17mA/cm^2. The broad current density peaks lead to complexity in identification of the individual processes. A might be assigned to conversion of Fe(0)/Fe(II) but is stated to have a too high potential around -0.56V. Accordingly peak B might be assigned to the conversion Fe(II)/Fe(III) or Fe(II)/Fe(II,III) but might also be located at to positive potentials. Peak C at the end of the potential window can reflect capacitive currents or ongoing iron oxidative behaviour.

D might show the reduction of FeS around a potential of -0.98V theoretically, or the conversion of Fe(II,III)/Fe(II) or Fe(III)/Fe(II) or the conversion Fe(II)/Fe(0) or even the hydrogen evolution reaction. The latter is the most probable. The combination of many possible reactions might be identified. The slope in D decreases between cycles 6 and 21 from 140 to 95. Although the slope decreases, note that the current density still decreases between cycle 6 and 21 from -10.81mA/cm^2 to -11.50mA/cm^2. In the two repetitions of this sample, this fluctuated. Also an ascending slope was measured while the current density near this potential decreased.

Comparative study With acquiring the data applying a linear potential sweep back and forth for 20 cycles, the cyclic voltammograms could be observed for all different species. Regarding the potentials near the HER, the current densities and evolution of current densities were observed. The slope of the curves in potential -1.3V were given in Table 5.6. Note that the absolute values

Table 5.6: Overview of important quantities in cyclic voltammograms with different additives. Regarding the current densities and evolutions in the HER range, the electrochemical behaviour in the HER range was influenced by the kinetics occurring at a more positive potential from the cathodic linear sweep. A=anodic, C=cathodic. Note that the active iron material was higher for a sample without the additive.

	FePE	**Bi_2S_3**	**Bi_2O_3**	**ZnS**	**FeS**
First - last cycle	6-20	7-20	8-20	3-19	6-21
HER slope development	41.27-40.54	96-131	112-84	26.81-38	95-140
HER difference	+0.73	-35	+28	-11.36	-45
HER difference per cycle	+0.05	-2.69	+2.33	-0.71	-3.00
Anodic/Cathodic Charge	A»C	A»C	A $\approx$ C	A»C	A»C
Linear behaviour i-V	No	Yes	No	No	Yes

For the sample with Bi_2O_3, unlike the peak B for a pristine sample, two separate peaks C and D could be observed which might reflect the two-step separate oxidation of Fe(II)/Fe(II,III) and Fe(II)/Fe(III)

subsequently. Peak B from the pristine sample as well as peak B from the sample with bismuth oxide are in good agreement (around -0.82V to -0.77V for a pristine sample between the first and last cycles and -0.78V to -0.74V in the first and last cycle for bismuth oxide). Whereas for a sample with ZnS the potential was determined at -0.88V if this peak was reflecting the conversion Fe(0)/Fe(II). The deep discharge reactions of the anode were assigned to B/C and D but could not be characterized specifically.

For a pristine sample and ZnS: for ZnS the conversion Fe(II)/Fe(0) was measured as a shoulder peak near the HER at a potential of around -0.94V with current density 0.31 mA/cm^2 in cycle 3 and in cycle 20, at position -0.98V the current density becomes -1.56mA/cm^2 cycle. For a pristine sample, the peak position increases from -0.98V to -1.05V and the current density increases from -1.16mA/cm^2 to -2.86 mA/cm2. Thus, ZnS was able to reduce the overpotential for the reduction of Fe(II)/Fe(0).

Only bismuth oxide was able to show some reversibility in the CV while decreasing overpotential for both the Fe(II)/Fe(0) conversion with respect to a pristine sample (from -1.05V to -0.99V for cycle 20) and the reduction of Fe(II,III) or Fe(III) to Fe(II) valence states drastically. No other cyclic voltammogram showed any sharp reduction peak in this range. Its lower particle size and the higher reduction potential (around -0.56V vs MMO) of bismuth oxide in combination with effective deposition of bismuth might have caused the effective reduction of Fe(II,III)/Fe(II) and Fe(III)/Fe(II) here.

As seen from the previous diagrams within the CVs with additives bismuth sulfide, bismuth oxide, zinc sulfide and iron sulfide, the overall behaviour of a sample with bismuth sulfide and iron sulfide were quite equivalent. The reduction of bismuth sulfide might happen at a equilibrium potential of around -0.92V strongly interfering with the HER, because subsequent deposition occurs in the same range of potentials.

$$Bi_2S_3 + H_2O + 6e^- \rightarrow 2Bi + 3S^{2-} \tag{5.1}$$

The sulfide ions breakdown the oxide layer of $Fe(OH)_2$ down into FeS and 2 OH^- ions. This formed compound FeS might increase the anodic charge heavily:

$$S^{2-} + Fe(OH)_2 \rightarrow FeS + 2OH^- \tag{5.2}$$

Note that for the sample with FeS the slope decreased but the current near the HER potential decreased. This was fluctuating between the different measurements slightly thus. Note that the larger particle size of bismuth sulfide and iron sulfide might have contributed to less efficient electron transfer and diffusion limits causing the more linear behaviour in the curves. Moreover, the lower reduction potentials might not have a great effect on the lowering of the overpotential. The peak belonging to Formula 5.1 might have happened but was not observed from the CV for the sample with bismuth sulfide. In addition, the reduction of FeS was not observed clearly. All in all, the increase in reversibility of discharge products seen in the CV for the additive with Bi_2O_3, with this particle size, was observed. It might be that this more positive reduction potential of bismuth oxide can be beneficial for the anode.

Note the difference on the active iron material of FePE and the samples with additive. Therefore, the evolution in the slope near the HER should always be considered in combination with the absolute values. Irrespective of the active iron material, the anodic charge was larger than cathodic charge for FePE, bismuth sulfide, zinc sulfide and iron sulfide in the CV. FePE has an increased slope and current density with respect to the HER potential in combination with low reversibility.

5.2.3. Post-CV Characterization

In Figure 5.20 5.21 5.22 and 5.24 the XPS spectra are given of the post-CV samples. The data consist of full surveys and the high resolution spectra including peak fitting by Gaussian-Lorentzian fitting approach and deconvolution of corresponding Fe2p and O1s peaks. In the deconvoluted spectra, the peak shape, positions and corresponding chemical bonding can be seen. In Appendix B Table B.2, all the deconvoluted peak positions are stated as well as their theoretical values (in which the peak positions are close to the theoretical value).

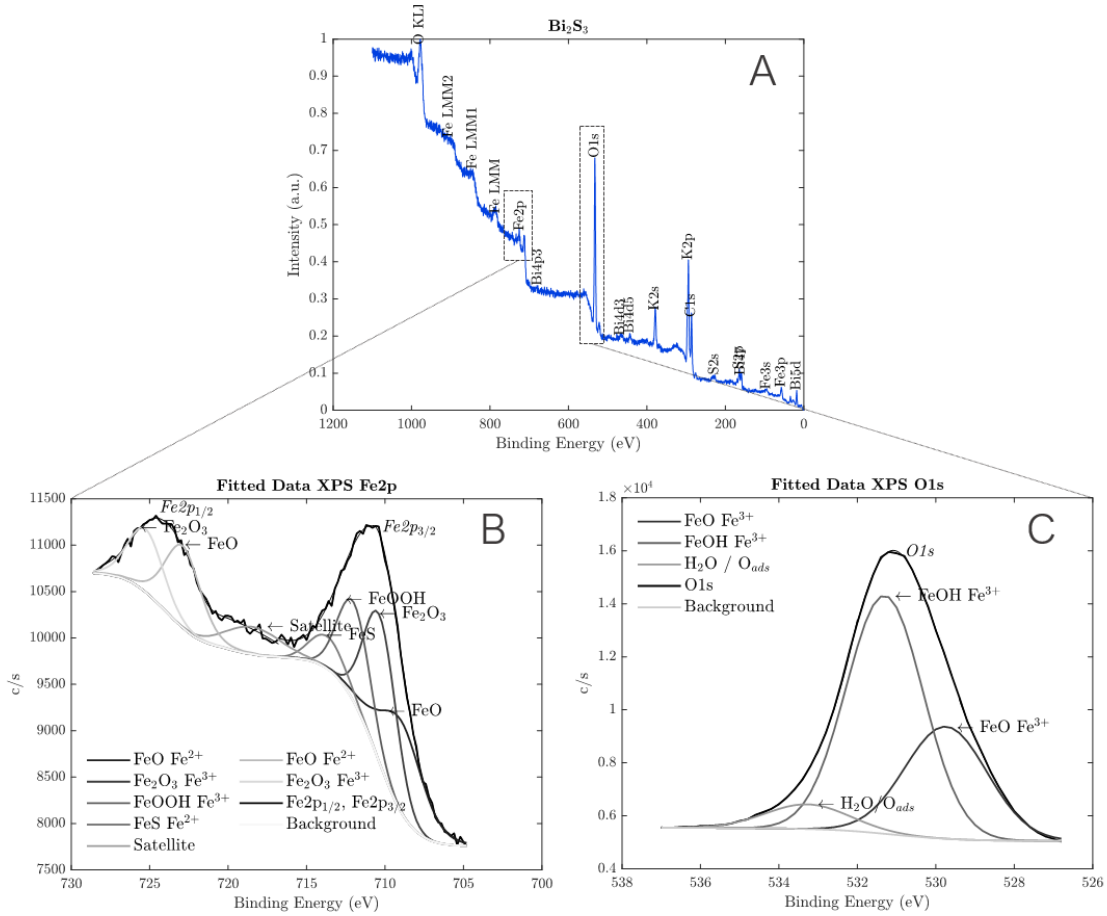

Figure 5.20: XPS spectra. A) Full survey B) High resolution on $Fe2p_{3/2}$/$Fe2p_{1/2}$ and C) the O1s peak. Sample was a post CV tested sample with bismuth sulfide. A Gaussian fit for readability was done by Matlab on top of the original data. The χ^2 for Fe2p was lower than 40 and the χ^2 for O1s was lower than 40.

In Figure 5.20, we see a significant O1s peak with respect to the rest of the peaks from the full survey. We observe 5 different bismuth states: Bi4p3, Bi4d3, Bi4d5, Bi4f and Bi5d. The first three seem to have minimal contribution within the bismuth compounds. There was an increased amount of Bi4f and Bi5d. Large K2s and K2p peaks was observed which confirms the adsorption of K^+-ions from the electrolyte. A small amount of sulfide ions were found and the surface was according to the XPS data covered with oxides and iron compounds. The Fe2p and O1s spectrum reveal the different chemical states. A significant contribution of FeS was found which should imply the breakdown of the $Fe(OH)_2$ layer. In addition, contributions of FeOOH, Fe_2O_3 and FeO were present. Fe_3O_4 is a mixed valence state of Fe(II) and Fe(III) showing compounds of Fe_2O_3 and FeO. We observed a relatively high O1s peak with Fe(III) bonded compounds with respect to the sample with zinc sulfide and bismuth oxide. Note that the Fe2p were lowest in intensity (around 11500 c/s). The relative peak of Fe_2O3 was always higher than the FeO peaks.

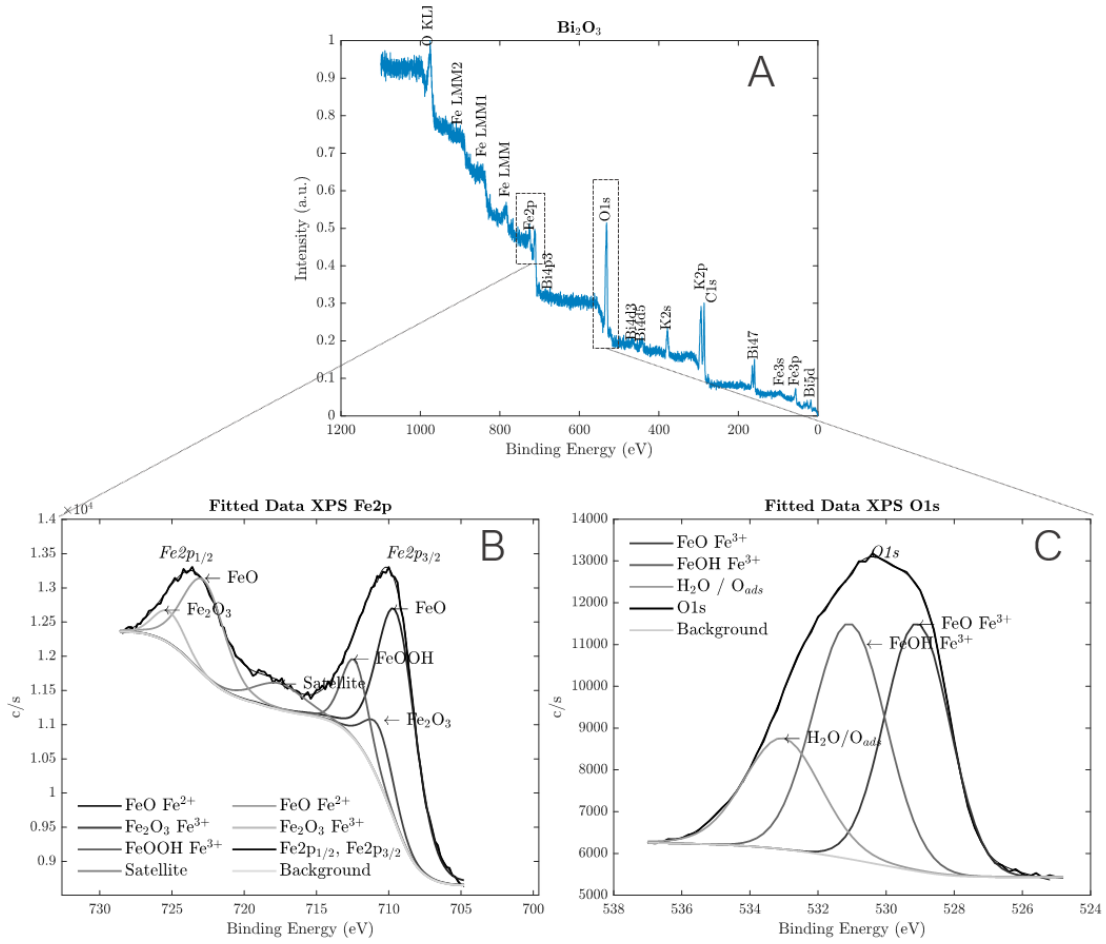

Figure 5.21: XPS spectra. A) Full survey B) High resolution on $Fe2p_{3/2}$/$Fe2p_{1/2}$ and C) the O1s peak. Sample was a post CV tested sample with bismuth oxide. A Gaussian fit for readability was done by Matlab on top of the original data. From PHI fitting, the χ^2 value was equal to 16.791 for Fe2p and the χ^2 for O1s was lower than 40.

In Figure 5.21, again the full survey A) and the high resolutions of Fe2p B) and O1s C) are stated, now for a sample with bismuth oxide. Equivalent compounds could be found in except the sulfide peaks. The iron and oxygen peaks in B) and C) were almost equivalent in intensity around 13000 c/s. Compared to the spectrum with bismuth sulfide, the O1s peak is lowered in intensity of the peaks and the Fe2p peaks are slightly higher. Remarkable is the significantly reduced Fe_2O_3 peak in the $Fe2p_{3/2}$ and $Fe2p_{1/2}$ spectra, which might imply a less stable oxide rich surface area which was in good agreement with the CVs obtained when focusing on the reversibility. Moreover, the drastic decrease in O1s peak confirmed this. Also an increased amount of Bi4f was found which might imply the effective deposition of bismuth on the electrode interface, effectively playing a beneficial role for efficient reduction of iron oxides towards iron. Compared to bismuth sulfide, this spectrum had a larger FeOOH peak at 12000 c/s, but was lower than FeO.

In the Figures 5.22 and 5.23, the spectra for a sample of with ZnS post-CV are given. In addition to the information given in A-C also the zoom plot of the zinc peaks $2p_{3/2}$ and $2p_{1/2}$ were shown in order to understand the degree of soluble zinc species. Since the peaks of the zinc spectra were relatively high compared to the other peaks, also having the zinc peak exactly at the relative position around 1022.07 eV. Comparing the Zn peak to 1021.9 eV and ZnS 1022.3 eV it was assumed some ZnS had dissolved into the electrolyte, confirmed by relatively low sulfide peaks. Because of the high relative peaks of Zn overall, it was assumed not a sufficient amount had dissolved. In the Fe2p and O1s peaks, all values were relatively high. In these fitted and deconvoluted spectra, it could be observed mainly Fe_2O_3 compounds were present.

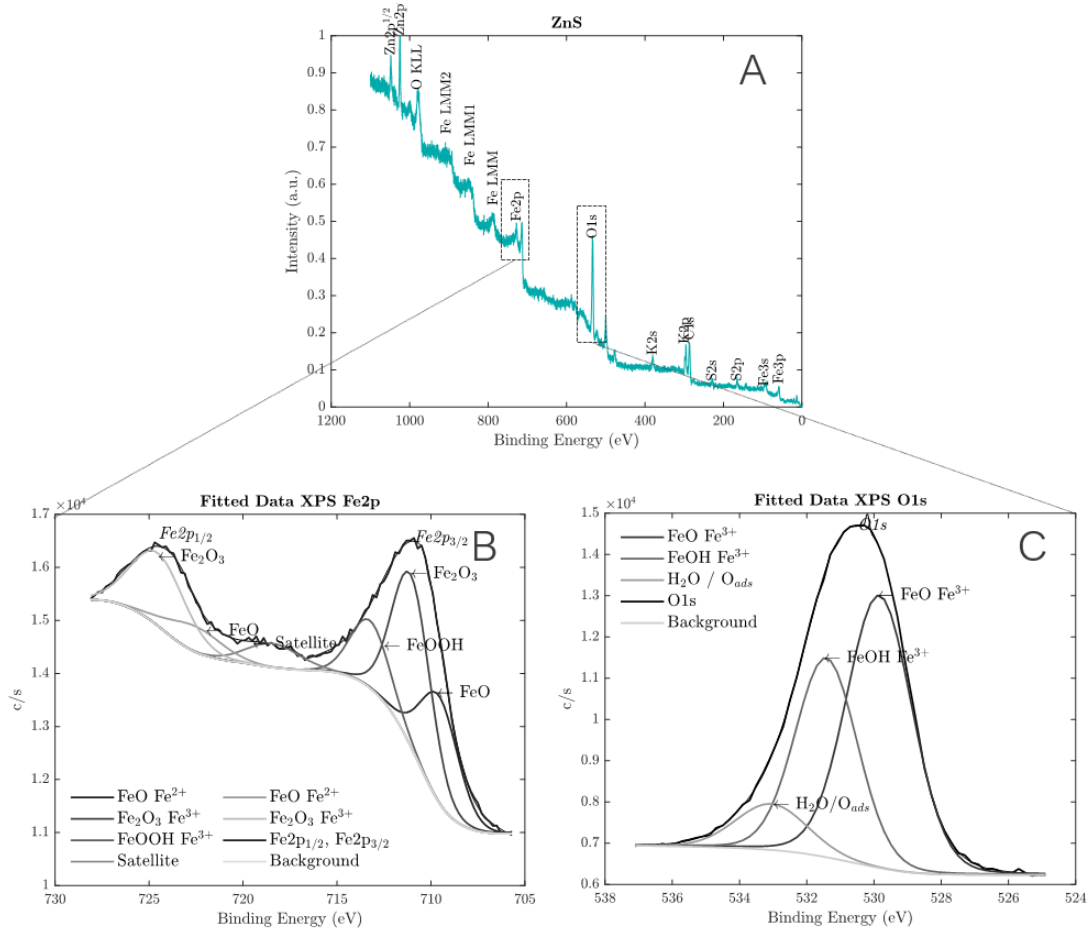

Figure 5.22: XPS spectra. A) Full survey B) High resolution on $Fe2p_{3/2}$/$Fe2p_{1/2}$ and C) the O1s peak. Sample was a post CV tested sample with zinc sulfide. A Gaussian fit for readability was done by Matlab on top of the original data. From PHI fitting, the χ^2 for Fe2p was equal to 15.460 and the χ^2 for O1s was equal to 8.697.

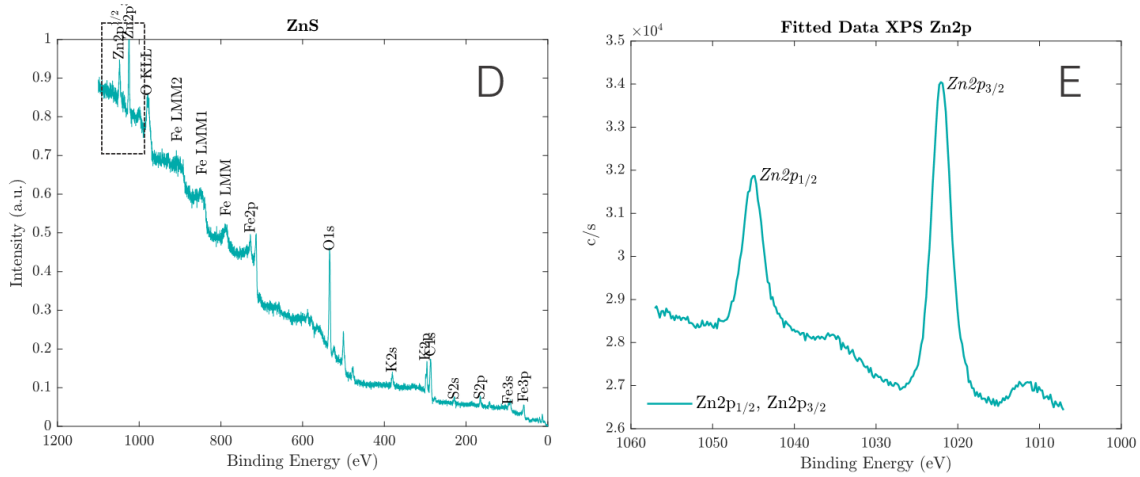

Figure 5.23: Zoom on Zn peaks from full survey. No high resolution was done on this window. Probably, a few amount of zinc or sulfide ions were dissolved into the system.

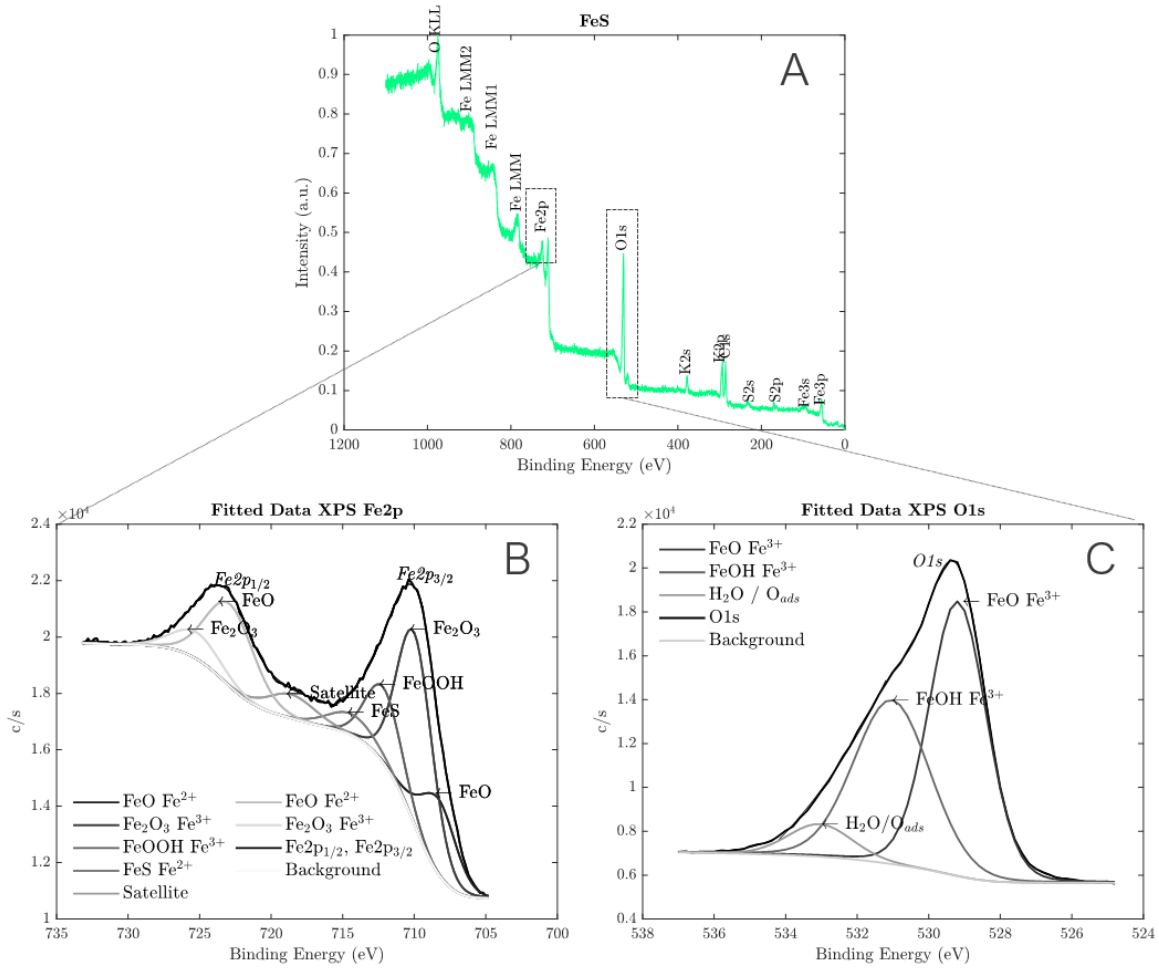

Figure 5.24: XPS spectra. A) Full survey B) High resolution on Fe2p$_{3/2}$/Fe2p$_{1/2}$ and C) the O1s peak. Sample was a post CV tested sample with iron sulfide. A Gaussian fit for readability was done by Matlab on top of the original data. From PHI fitting, the χ^2 for Fe2p was equal to 9.330 and the χ^2 for O1s was equal to 18.387.

In Figure 5.24A-C the highest amount of iron was measured probably because addition of iron sulfide resulted in an increase of active iron material during the CV scans. The largest intensities in the oxygen spectra O1s were identified for this sample with iron sulfide, equivalently to the sample with bismuth sulfide (around 22000 c/s for O1s (FeS) and 18000 c/s for O1s (Bi_2S_3) compared to 15000 c/s for O1s (ZnS) and 13000 c/s for O1s (Bi_2O_3). Within the Fe2p spectra, the lowered FeS peak compared to the oxides might indicate the dissolved sulfide ions into the electrolyte. The sample with FeS still had a higher peak (18000 c/s) of FeS compared to the FeS peak for the bismuth sulfide sample (around 10000 c/s). The stable oxide peak of Fe_2O_3 was larger compared to FeS and FeO, but in the Fe2p$_{3/2}$ spectrum the Fe_2O_3 peak was lower. To sum up the observations from kinetic studies in CV and obtained spectra from XPS:

1. Sample without any of the four additives showed increasing HER peak, with also increasing slope (but still lower than bismuth oxide).
2. Within the performed CVs, Bi_2O_3 might increase reversibility in reduction, since Bi might be effectively deposited before reduction of iron (hydr)oxide species, effectively promoting reduction in that range. The compound Fe_2O_3/FeOOH was compared to FeO peaks low (not observed for the other samples). Only the absolute values of the bismuth sulfide species had significant lower peak values Fe_2O_3/FeOOH, but no Fe_2O_3/FeOOH peak lower relative to the other peak FeO. Moreover for Bi_2O_3, the O1s peak showed the lowest intensities compared to the other samples.
3. It was difficult to identify magnetite because of its mixed valence state of Fe(II) and Fe(III). Fe^{2+} and Fe^{3+} were ascribed to FeO and Fe_2O_3 solely. Never, the peak-to-peak ratio was 1:2 Fe(II):Fe(III) and can be solely ascribed to magnetite, but is was assumed magnetite was formed. Fe_2O_3 was

not described as redox reaction hahhbut can also form.

5.2.4. Durability Test

In Figure 5.25A, the first full cycle including discharging for 10 hours at a 2mA/cm^2 rate, cut off potential at -0.55V. The initial charging of 15 minutes with equal charging current density was not shown but was performed to reduce the native oxide layer. All curves in cycle 1 show initial stable behaviour all adding up to a full discharge capacity of 8.3mA*10h/(0.46(=fraction exposed to electrolyte)*total gram of 13.4 sample*0.865 gr active iron material=15.6mAh/g. In sample with Bi_2O_3, the maximum retention was already measured at a maximum in the fourth cycle where the discharge/charge retention was determined as 30.8%, from which it faded. In Figure 5.25B the last measured cycle for ZnS was given in the 31th cycle, in which the discharge capacity was fading with a retention of around 17.8%, so no curves were there to be displayed in the last cycle 36 in Figure 5.26F. The discharge capacity is not measured in a later stadium than -0.55V where the cut-off potential was stated.

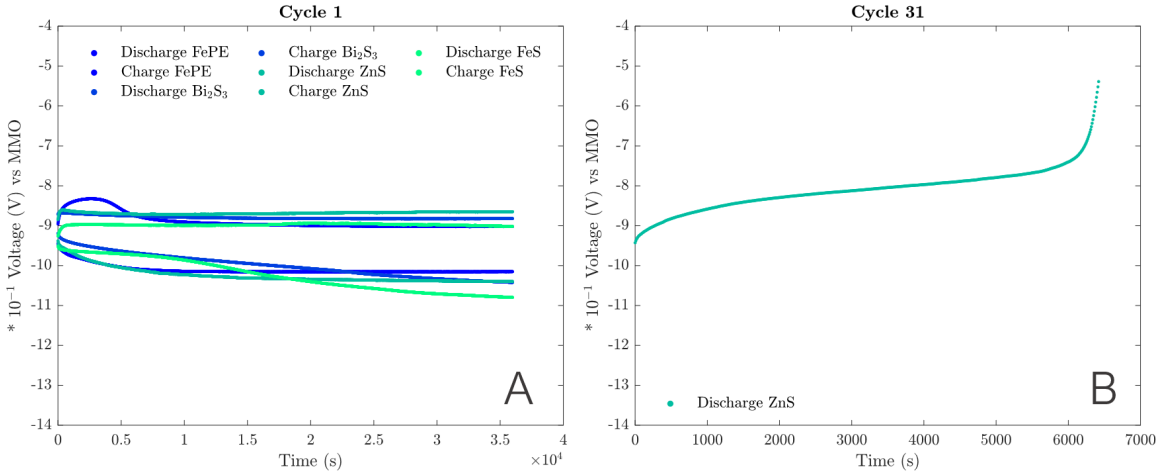

Figure 5.25: Illustration of four samples with the three different additives. All samples have capacity retention of 100%. Note that this is actually 4000% with respect to previous cycle (15 min charge). Note that bismuth oxide needed 2 cycles to have its potential more negative than the cut-off potential, so not illustrated here.

There is a discharge capacity loss determined in cycle 6 by Bi_2O_3 as is indicated in Figure 5.26A. Discharge capacity decreased slightly after the maximum measured in cycle 4 of 30.8% and fluctuated between the fifth and 33th cycle always between the minimum value for cycle 33 at 11.5% and a value of 20.3% in the fifth cycle. With bismuth oxide the capacity remained very low. Notably, in cycle 12 (Figure 5.26B, the sample without any additives (FePE) also started to lose its discharge capacity. FePE lost its capacity between cycle 7 and cycle 8 by a significant increase in potential of +0.24V measured between cycles 7 and 8 at the end of discharging and thereafter only reducing capacity retention. In cycle 10 the lowest capacity retention was measured of around 11.3%. Remarkably, the capacity of FePE started to increase again and in cycle 30, the capacity retention decreased to a value of 91.6% after full capacity retention in cycle 28 and 29 of 100%. In cycle 35, the capacity retention was still determined on 78.0%. It was expected the capacity retention would decrease after this value. This phenomenon of discharge increase after rapid passivation was also given for a sample in the study on porosity in which in cycle 21 a significant increase in capacity was given again.

It was observed here that ZnS lost 60% of its capacity between cycle 14 and 17. After cycle 18, there was a slight discharge capacity increase up to cycle 24 and faded again in cycle 30. The latest cycle for ZnS was measured in 31 as discussed earlier. For the samples with bismuth sulfide and iron sulfide, the discharge capacity remained the highest among all the different samples and could sustain their capacity retention at 100% at a cycle of 36 in the half cell. The most stable flat plateaus were designated to FeS and characterized mostly the Fe(0)/Fe(II) conversion. The samples with bismuth sulfide could hold its discharge capacity at 100% even at the 36th cycle as well. It is assumed the reactions were mainly in the Fe(0)/Fe(II) and Fe(II)/Fe(III) or Fe(II)/Fe(II,III) as well, The potential of bismuth sulfide gradually increased to higher voltage values over the cycles of around -0.6V at the end

of the cycles from cycle 24 and on. Note that in the fourteenth cycle and in the twentieth cycle of FeS and ZnS, respectively, the electrolyte reservoir was slightly refilled since the level was lower than the half of the total volume. Despite the sufficient sealing effect of the parafilm clamped onto the reference electrode with the cell design, still some room for leakage occurred from the top and that was why the cells with FeS and ZnS were refilled. Note that the cell with Bi_2O_3 also had lower-level electrolyte than full, but still more than half was filled to the top.

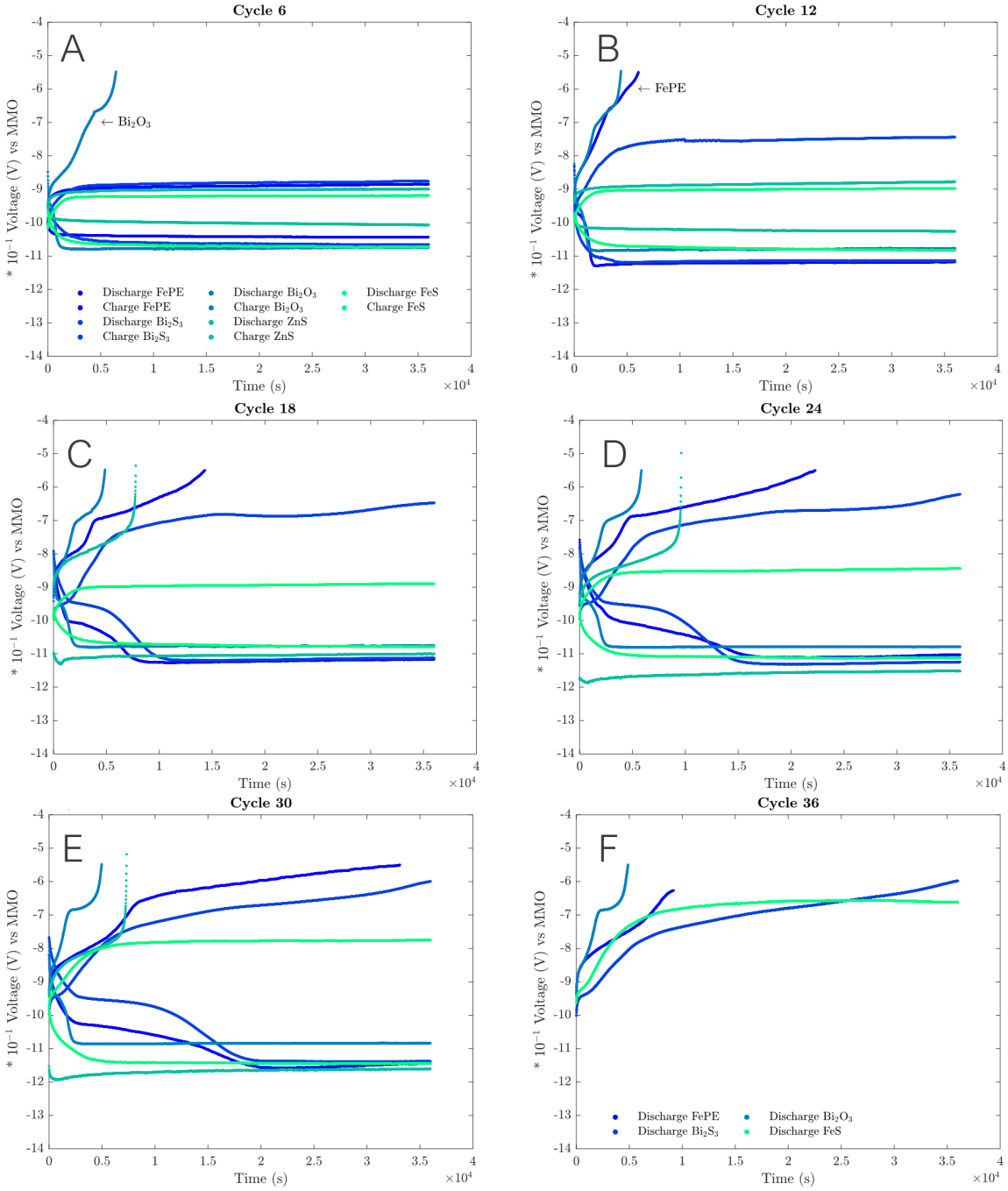

Figure 5.26: A-F) give illustration of different cycles 1, 6, 12, 18, 24, 30 and 36 during galvanostatic cycling of the 5 different samples. Note that FePE was suddenly stopped in cycle 36 but could be extrapolated to around 90% as well. Only the plateau was observed around -0.70V.

Coulombic efficiency could have been calculated if the dominant reaction was only capacity loss that could be ascribed to hydrogen gas evolution. Since also passivation plays a dominant role here,

not the coulombic efficiency was described here, but the capacity retention on cycles 1, 18 and 30. The histogram that was obtained by these measurements are given in Figure 5.27. In addition, the potentials at the end of charging were given per sample. The differences here were not significant and could not explain difference in electrochemical behaviour to high extent. Capacity retention for all samples in the cycles 1, 18 and 30 are given in the Figure.

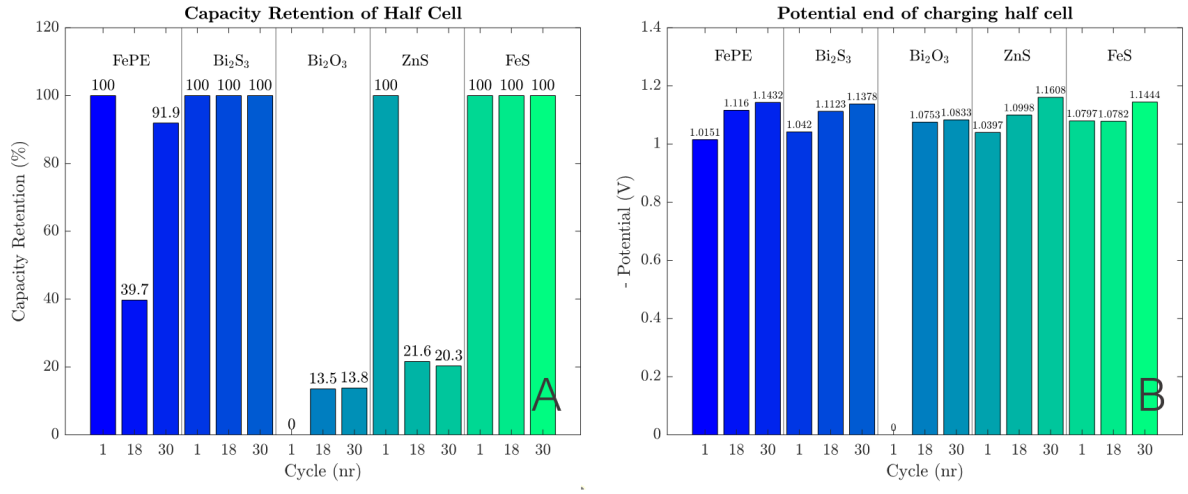

Figure 5.27: A) reflects the capacity retention in cycles 1, 18 and 30. B) reflects the potential at the end of charging to examine the overpotential here (note that the values are negative values).

From the results given in Figure 5.27B, it can be observed that the potential differences at the end of charging did not significantly differ. The main differences were observed in the first stage of charging. In Figure 5.27A, the discharge capacity retention percentages were given.

The results on full cell measurements are given here. In Figure 5.28A and B the efficiencies (%) and energies (Wh) are given for alle samples with the four additives and without.

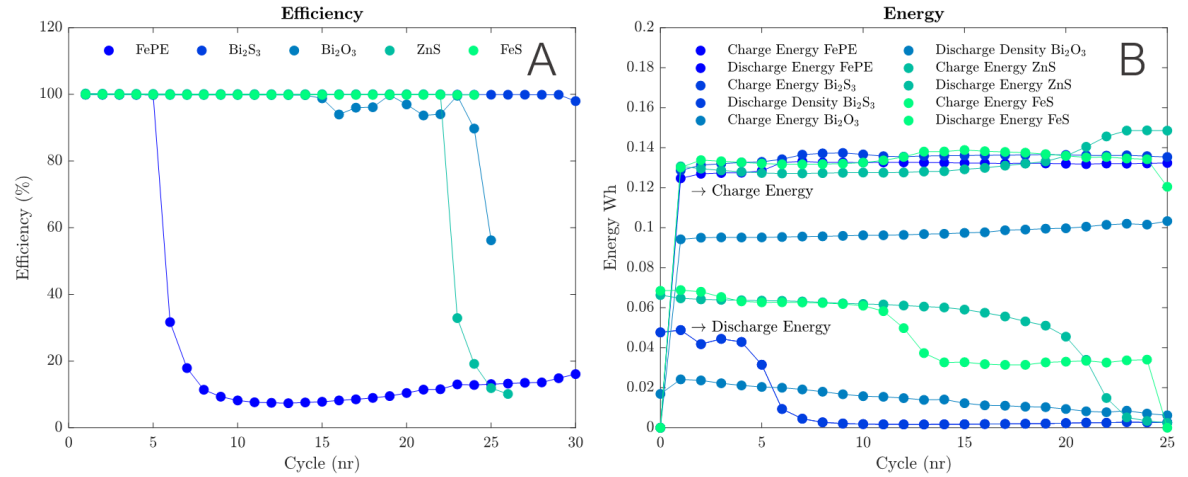

Figure 5.28: Overview of left A) the efficiencies in the full cell and on the right B) the energy for discharging and charging. From each charge/discharge pair the charge values are given in the top, and the discharge values on the bottom.

Note that the efficiencies are no more than a capacity retention the previous charging cycle here. All cells were initially cycled up to 25 cycles and all cells were prolonged in order to check the maximum durability of each full cell.

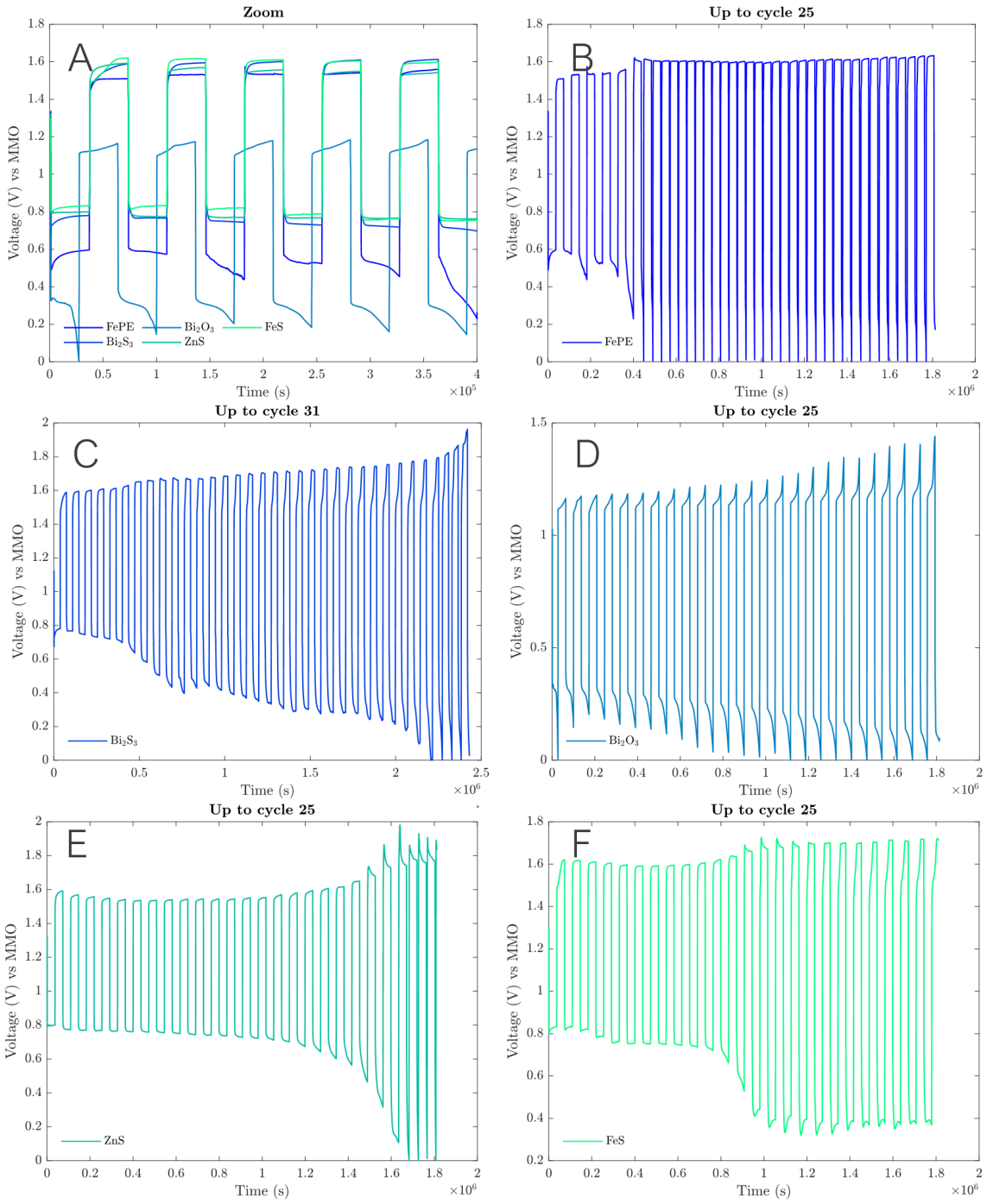

Figure 5.29: A-F) results reflect the full cell performance of the samples with different additives. A) shows the first 5 to 6 full cells. B) reflects FePE, C) reflects the behaviour of a sample with bismuth sulfide as additive and D) with bismuth oxide. E) reflects ZnS and F) reflects FeS. Tests from diagram D), E) and F) were extended, but not reflected here. E) and F) were extended to see if the discharge capacity could be retained. For F) 100% efficiency was extended to cycle 41, see Figure A.2.

The Full E vs. time plots are given in Figure 5.29 for all samples with a clear zoom on the first 5 to 6 cycles. In Figure 5.29B the rapid passivation can be seen for a sample without any additives already after 5 cycles. For long time – which can be seen in Figure C) the sample with bismuth sulfide sustained capacity, but faded after around 29 cycles. In D) we observe a total shift in the potentials concerning charging and discharging. Both values were significantly lower than all the other samples as seen in Figure 5.29A. Remarkable is the prolonged constant behaviour of potentials in this range, which might confirm the reversibility. In D) a full capacity retention was measured only up to cycle 14.

In E) a stable behaviour of ZnS is observed which passivated after $\pm$ 22 cycles. Only the sample with FeS showed in F) a long stable behaviour up to 25 cycles, which in an additional measurement could sustain the discharge retention of 100% for another 16 cycles. So, of all samples with additives, in the full cell the sample with FeS could sustain its capacity for a total of around 41 cycles.

The results of the full cell show a good agreement with the results in the half cell, when looking at the orders of passivation. In the full cell, FePE shows fast passivation, Bi_2O_3 a constant low value of discharge and charge capacity value. FeS shows highest capacity retention (100%) over the most cycles (41) in the assigned potential range. The extended measurement on the sample with FeS is given in Appendix A A.2. Bismuth sulfide shows in the half cell large capacity retention up to cycle 36, from which the retention was definitely stopped in cycle 29 in the full cell. Apart from Bi_2S_3, all galvanostatic charge-discharge full cell tests were extended from Figure 5.29 in order to observe further passivation behaviour. Apart from FeS, from which the Figure is shown in Figure A.2, these curves were not showing an increase in the discharge capacity anymore (their figures not shown). Bi_2S_3 as seen from Figure 5.29C was fully charged, ZnS was fully charged (after 44 cycles charging) in the extended test, Bi_2O_3 was almost fully charged in the extended test and FeS was fully charged as seen in Figure A.2. The samples evaluated by microscopy in the next Section underwent these additional cycles thus, and ended in the fully charged state. These additional cycles for Bi_2O_3 and ZnS (except thus for Bi_2S_3 which was not extended and FeS in which the performance was increased) were not considered for the performance since these tests were not valuable.

5.2.5. Post-CV and Durability Test Characterization

In Figure 5.30, the results are given of the samples after CV in a 2D and 3D image to map their contour and depth profile. Profiling has been given for samples with the relevant additives: bismuth sulfide (A-B) and bismuth oxide (C-D). The sample with bismuth sulfide, shows a depth of around 18.53 μm and the sample with bismuth oxide around 14.50 μm. In Figure 5.31, the results are given of the samples after CV in a 3D image to map their contour and depth profile for the samples with zinc sulfide and iron sulfide. For the sample with zinc sulfide a uniform distribution is observed with a depth of around 16.54μm and for the sample with iron sulfide this was equal to 22.71 μm.

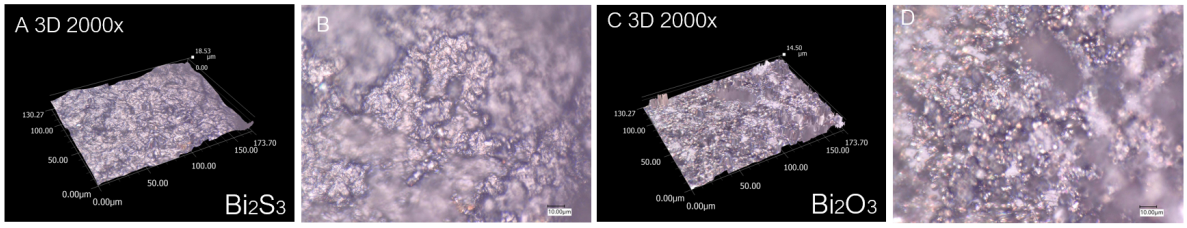

Figure 5.30: Overview of left A) the 3D image and in B) the 2D image after CV of bismuth sulfide and in C) 3D image of bismuth oxide and in D) the 2D image. All obtained by KEYENCE microscope. These findings were not found universal for different cross-sections in the samples, but their overall behaviour (roughness) on the samples was reproducible. The samples with bismuth sulfide contained full coverage of iron oxide products, whereas the sample with bismuth oxide also shows reduced discharge products and more active iron material was found on the surface.

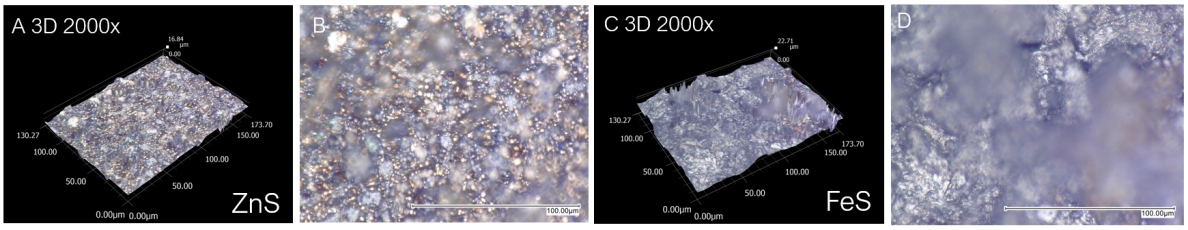

Figure 5.31: Overview of left A) the 3D image and in B) the 2D image after CV of bismuth sulfide and in C) 3D image of bismuth oxide and in D) the 2D image. All obtained by KEYENCE microscope. These values were not found uniformly through the whole surface area of the sample, but the behaviour of surface coverage was identical. In the sample with zinc sulfide we identify some redox products with also some active iron material formed again. The sample with iron sulfide shows heavy coverage of discharge products.

In this study we were able to perform a cyclic voltammogram on iron-based electrode with powder nature. Different combined observations were found:

1. FePE: shows an increase in their slope near this potential of -1.3V as well as their absolute current densities (FePE increases from -8.4mA/cm^2 to -10.37 mA/cm^2). After cycling the sample with FePE it was observed that almost no material of the anode was preserved, and much powder was ripened off. This made post characterization almost impossible, so no illustration was given on this.
2. Bi_2S_3: the absolute value decreased (22.96 to 17.27 mA/cm^2) as well as their slope (decreased with 35 from cycle 7 to 20) near this value. The anodic charge was significantly higher than the cathodic charge. The sample with bismuth sulfide shows a clear linear behaviour in CV. The larger brittle particles obtained from pre- characterization might have increased the resistance for efficient ion migration paths or electron transfer. Note that bismuth sulfide still has the highest absolute value in current density near HER.
3. Bi_2O_3: the current density increased from 18.08 mA/cm^2 to 24.18 mA/cm^2 near the HER potential. Bismuth oxide shows the highest slope increase in that potential range (+28 from cycle 8 to 20). In addition, the highest reversibility is measured in these CVs, which might confirm the effective role of bismuth increasing electron transfer and catalyzing the relevant electrochemical reactions. In addition, the post tested surface was relatively flat and showed some increase in active iron material again.
4. ZnS: the absolute values decreased as well as their slope near this value (for zinc sulfide from -12.195mA/cm^2 to -9.06mA/cm^2). Its slope decreased with 11.36 between 3-19. The surface after testing was relatively flat and showed some increase in active iron material and an uniform passive layer after CV. The CV and high stable oxide peaks from XPS could not validate the reactivation of the material.
5. FeS: the absolute current densities in this potential increased from -10.81mA/cm^2 to -11.50 mA/cm^2 over the cycles but its slope decreased (slope reduction of 45). A clear linear behaviour was observed in the diagram. The larger brittle particles obtained from microscopy might have increased the resistance for efficient ion migration paths or electron transfer. High oxidative behaviour was measured. This slope reduction or absolute value near the HER fluctuated. Here, its slope decreased with 45 between cycle 6 and 21.

Note that it was important to determine the state of each sample clearly (fully charged, fully discharged, etc.) after the durability test, i.e. at which point the half- and full cell measurements were stopped. This was necessarily in order to understand and compare its roughening and degree of accumulation of discharge products.

In Figure 5.32, the surface of the samples are given of the samples after the durability test in the half cell (fully dried). Note that the state of the samples after the half cell test were directly related to where the half cell test was stopped illustrated in Figure 5.26. In all half cell tests, the final charged/discharged state was slightly different when looking at where the test was stopped. Although, some trends could be observed. Bi_2S_3 and FeS were both in the fully discharged state and both showed heavy roughening. Looking at ZnS from which the experiment was stopped only 2 hours of charging showed less rough surface and some cracking in the surface. Looking at bismuth oxide (more in a charged state retrieved from Figure 5.32) an heavily ruptured sample was observed as well. It was unclear when this happened, but during the whole experiment the back of the sample seemed stable. Despite having different charge or discharge states after half cell testing, it was assumed that cracking would always have been observed independent of any discharge or charge state (also confirmed by full cell test of bismuth oxide which was not so much in the fully charged state). Because ZnS and Bi_2O_3 reached soon the potential of -0.55V upon discharging, it was assumed that these samples were more in combined charged state. Since all samples of the half cell were in different states, it was necessary to obtain the full cell surface after testing.

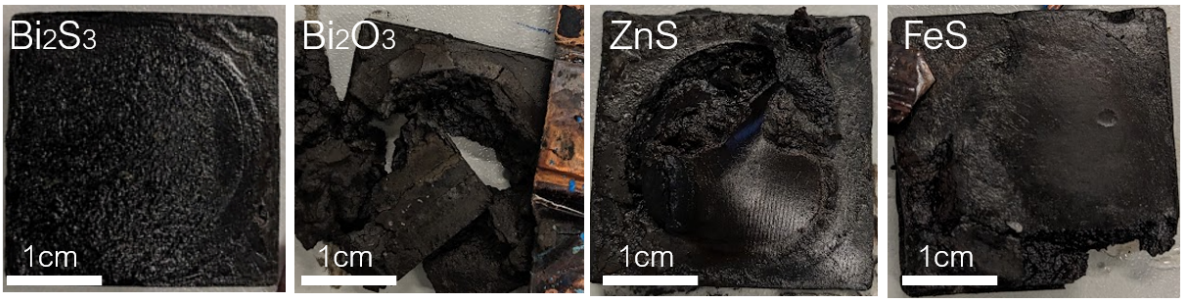

Figure 5.32: Overview of left A) bismuth sulfide B) bismuth oxide C) zinc sulfide and D) iron sulfide after durability test in the half cell.

Apart from Bi_2S_3, all galvanostatic charge-discharge full cell tests were extended from Figure 5.29 in order to observe further passivation behaviour. In was confirmed that bismuth sulfide, bismuth oxide and zinc sulfide already reached their maximum efficiency in the results depicted in Figure 5.29. Only FeS could extent its behaviour to cycle 41 as mentioned earlier. Apart from FeS thus, from which the Figure is shown in Figure A.2, these curves were not increasing the discharge capacity anymore (their figures not shown). Although, the surfaces after these extended tests were given in Figure 5.33. The samples when illustrated after testing were almost in equivalent state (fully charged, only bismuth oxide (slightly more discharged/half-discharged)). Thus, bismuth sulfide, iron sulfide and zinc sulfide were all in completely charged state. This was due to the fact the test was stopped when the potential hit the upper and lower limit many times in short time and the sample lost much of its discharge capacity already, all samples ended in the fully charged state. Now it was possible to compare the surface morphology and roughness systematically. The sample roughness is most dominant in the samples with bismuth sulfide and iron sulfide, in agreement with the samples after testing in a cyclic voltammetry and with previous full cell tests. In cyclic voltammetry, ZnS showed some more roughness than the sample with bismuth oxide. To conclude, even when the samples with bismuth sulfide and iron sulfide were in fully charged state and showed apparent rough behaviour.

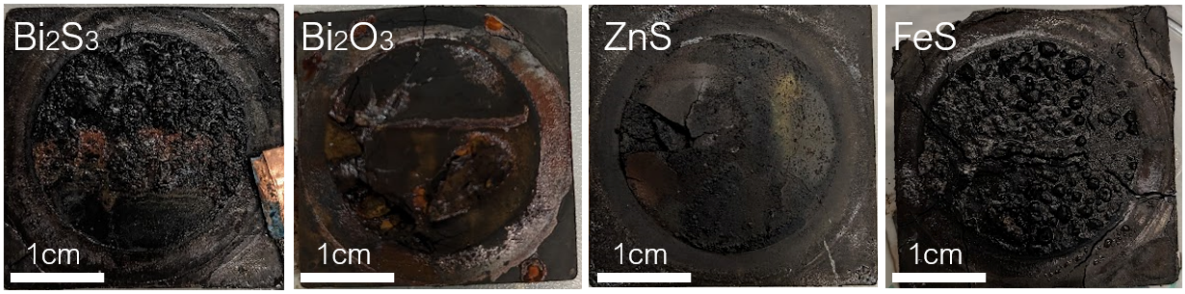

Figure 5.33: Overview of left A) bismuth sulfide B) bismuth oxide C) zinc sulfide and D) iron sulfide after durability test in the full cell. Note that only the sample with bismuth sulfide corresponds directly where the durability test in Figure 5.29. All samples were dried in order to see effective roughness without wetting KOH electrolyte residuals.

To sum up the observations from durability test, a couple of observations were done. The large brittle particles Bi_2S_3 and FeS might imply particle coarsening of active iron material to a larger extent than samples with ZnS and Bi_2O_3. The 3D profiles also confirmed these observations after CV in which an increased thick layer was found for bismuth sulfide and iron sulfide, to lower extent for zinc sulfide and the lowest extent for bismuth oxide. Here a combined explanation will be given on post-test and durability test observations. In the half cell, durability tests showed a clear shift already in the sixth cycle under these experimental conditions. It was found that the half cell correlated to the full cell performances to a clear extent. The performance of the half- and full cell will be summarized here:

1. FePE: in the half cell it was able to cycle with 100% capacity retention, but reached its minimum in cycle 10. In cycle 28 and 29 it retained capacity again after which it faded. This reactivation of the surface could imply that a new surface layer was dissolved and a new layer could sustain discharge capacity. In the full cell it could only sustain for 5 to 6 cycles and completely faded

afterwards. No heavy roughening was observed to the extent of the other samples. A uniform small roughness was found for the sample after full cell testing in fully charged state. In the half cell no roughness was found (half-discharged state). This reactivation was confirmed by the porosity study (in cycle 21).

2. Bi_2S_3: main observation is the heavily roughened surface structure after durability test in combination with 100% capacity retention in cycle 36. In the full cell the sample with bismuth sulfide was cycled up to 100% capacity retention until cycle 29.
3. Bi_2O_3: main observation is the heavily degraded anode surface structure after durability test in half cell and the flat surface after full cell performance. In the half cell, the capacity faded already after cycle 1 and showed maximum capacity in cycle 4. In the full cell the sample with bismuth oxide was cycled up to 100% capacity retention until cycle 14. The total voltage was shifted to significant lower values and were stable over time. Note that this additive was able to not bring discharge capacity immediately to zero, but gradual - in the full cell. A flat broken surface was considered here.
4. ZnS: a broken surface area was observed after the durability test in half cell and not so heavily roughening. In the half cell ZnS faded between 14-17 cycles and in the full cell after 22 cycles.
5. FeS: Main observation from the sample iron sulfide is the heavily roughened surface structure after durability test in combination with 100% capacity retention in cycle 36. For the sample of FeS this was 100% up to cycle 36 and up to 100% in the full cell up to cycle 41. To combine and understand these results, the material's properties of the additives and post-test imaging are considered. Note that the additive FeS might benefit from its beneficial reduction potential creating porosity, high electrical conductivity, solubility (dispersing well over the surface), readily available FeS ions, compatibility effect and larger particle size.

Note that the exact post-state of the samples depended on the underwent cycles and ratio of discharging/charging for a specific amount of cycles. So, the exact state was not considered, but from full cell test it was definitely stated that the samples were more in the charged state, and the main trends were depicted here. Note that electrolyte control was important to consider as well. For the half cell, by observation of sufficient leakage, a refillment was performed. This was not done when the level was still sufficient. For the full cell, the level was always filled to the top, especially in the first 25 cycles. It might be that the electrolyte level has been lowered in some cells in the last couple of cycles.

6

Discussion

In this Section the results of the Porosity studies and the Additive studies will be discussed in detail.

6.1. Porosity studies

The effect of 10wt% pore former was studied here. The pore former rich sample was investigated by an approach to decompose the K_2CO_3 pore former agent by naturally cooling in open air and under vacuum. The intensification on surface cracking was observed for the K_2CO_3-rich sample which might be clarified by high partial pressure pCO_2 by the enclosed compartment while hot pressing [45]. A sample which was cooled in between aluminum blocks showed more cracks than a sample cooled in full open air. For the sample that was cooled in full open air showed thus less cracking with the same dimensions of the pores. The vacuum method could not decompose any further K_2CO_3. The samples cooled in full open air were used in the tests and for the porosity measurements.

It is learned that the initial estimation on porosity might be too low. There is almost no difference measured with immersion technique for the sample with and without pore former. This might be assigned to incomplete decomposition of the pore former and fast attraction of ions from air by the pore former. Namely, the samples showed wetting by ambient air by its hygroscopicity after a while when held in open air. Despite the repetition of the measurement for reliability, the immersion technique was not considered ideal considering o.a. rippening off active material. It was assumed that most of the residual of K_2CO_3 will be dissolved by immersion in 6M KOH electrolyte, mentioned by Rodriguez et al. [44] and will then effectively work. This was characterized by electrochemical analysis studying the initial capacity and passivation behaviour. Subsequently, electrochemical analysis shows (note the inequal active material for the samples FePE and FePEK2CO3):

- Higher discharge capacity for the initial discharge capacity test. The specific discharge capacity for the sample with pore former was about 27 mAh/g more. Note that the counter electrodes in the half cell differ for the initial capacity (for the durability test, the counter electrodes were identical). A stainless steel mesh was applied since the sample with potassium carbonate might poison the cathode with carbonates.
- Discharge capacity decrease in the half cell test respectively with the addition of 10wt% pore former. The lower active iron material of FePEK2CO3 might have lowered this absolute discharge capacity for the half cell test. In the 20 cycles half test the discharge capacity was almost higher for the sample without pore former (note difference in active iron material and relatively low cut-off potential). In the half cell, FePE had ability to reactivate itself after full passivation after 20 cycles. The C/5 charge rate could have been the reason for the destruction after testing. The sample with pore former was totally ruptured. Both samples were here in the more charged state.
- Discharge capacity increase in the full cell test respectively with the addition of 10wt% pore former. This might be due to the fact that in the full cell the charge current density applied was 2.5 times lower than in the half cell or it can be assigned to unpredictable mechanical integrity of the sample by addition of a pore former. In the full cell where the charge current was lower, the sample with pore former performed better with a fluctuating discharge capacity. This might have hinted on

some dissolution of the K_2CO_3, dissolved over time. Note also the roughened behaviour of the sample with pore former after full cell test with stable behaviour (in a more discharged state), whereas the sample without pore former showed a more flat behaviour after testing (in the fully charged state although). Note that the extended cycles were not given for the samples with and without pore former in the full cell in which FePEK2CO3 achieved another 12 cycles.

Note that according to McKerracher et al. [6], the pore former did not have an effect on a 1mm thickness anode and they recommended to investigate the pore former K_2CO_3 on a thicker anode. The thickness of the anode was such, that the pore former should have an effect thus [6]. They recommended to shape the anode thicker in order to test the effect of pore former on the accessibility of electrolyte. According to Weinrich et al. [10], the thickness of the samples heavily lowered the specific discharge capacity. With a total thickness of around 3.8mm, this was confirmed. However, this thickness beneficial for the mechanical stability. The samples after testing that had underwent heavy mechanical degradation after addition of pore former had a lower capacity.

The hypothesis was not confirmed for the half cell and initial capacity where the capacity was lower for a sample with pore former. For the full cell this was reversed. In future, the ratio decomposition, dissolution and residual should be characterized. The initial estimation could have been too low and the calculated maximum capacity could not be relied on residuals of K_2O that might have been in the sample left.

6.2. Additives studies

Here, the effect of specific additives were investigated on their effect on the HER and passivation behaviour in hot-pressed iron samples. In the first stage of this study, all samples with different additives were pre-characterized, by obtaining the roughness and the porosity. The differences were marginal with respect to each other. Highest roughness was measured for a sample with bismuth oxide and zinc sulfide. It was assumed that the larger brittle particles of bismuth sulfide and iron sulfide were not captured in these areas. The roughness measurements were for all samples very close in surface roughness value. The porosity was obtained as well before electrochemical analysis. The porosity measurement for all samples were in between 15%-30% which was a relatively low porosity. From these measurements no clear trend was found in the additive particle types or particle sizes. Note that the low porosity and low equal surface roughness value for all samples could be ascribed to the high amount of pressure (88 MPa) which was applied, which was found necessary in order to preserve mechanical stability. We found the porosity measurements (as well as for the research question on porosity) inconclusive. The testing method might not be consistent for every sample. Drying of isopropanol at room temperature occurred. Although this method was applied consistently for all samples, it might be that in differences of milliseconds different amounts of isopropanol evaporated affecting the mass difference and thus porosity.

In CV the essential role of bismuth (or bismuth oxide) is displayed effectively increasing reversibility. Bismuth individually, might enhance kinetics suppressing side reactions lowering the reduction overpotential for the Fe(II,III)/Fe(II) or Fe(III)/Fe(II) and Fe(II)/Fe(0) conversion. Note that the linear behaviour of bismuth sulfide and iron sulfide might have hindered the representation of the peaks. There could be a chance that a lower particle size here would show some defined more peaks by effective charge transfer. From the XPS spectra and the post-test characterization by microscopy it was learned that a high oxidation behaviour is observed, but for all samples to another extent. In the high resolution spectra of bismuth oxide, the stable oxide peak of Fe_2O_3 decreased heavily which might confirm the highest reversibility of the sample with addition of bismuth oxide. The peaks of Fe_2O_3 and FeOOH were always lower than the FeO peak. The O1s spectrum also contained lower intensity here. To complete, also the reduction of stable oxides Fe(II,III)/Fe(II) or iron hydroxides Fe(III)/Fe(II) seems more effectively reversed with this sample. This might be due to the effective deposition of bismuth by its redox potential before sweeping the potential to the potential at which the reduction of magnetite and FeOOH occur. The increased current in the HER potential might be caused by the increased overall conductivity by increased active material. The Zn2p peaks for the sample with zinc sulfide showed a peak (at 1022.07 eV) in which both Zn (1021.9 eV) and ZnS (1022.3-5 eV) [46] were found. This could hint at some zinc dissolution for which the solubility was higher than for bismuth oxide or sulfide. Note that all potentials

were always slightly off their theoretical values. This might be caused by diffusion limits of the powder pressed anodes. For all samples no reduction peaks of the specific additives were observed. For ZnS this was fully explained by the fact that its reduction potential was out of the potential window. Note that particle size can affect the representation of the sharpness of the peaks, since larger particles might decrease effective electron transfer, resulting in a more linear behaviour.

To understand the enhanced electrochemical behaviour and performance of bismuth sulfide and iron sulfide, the following explanations for the different observations for the different samples are given with the help of different studies from literature:

- For the samples with bismuth sulfide micro-galvanic coupling might occur in which FeOOH and BiOOH are established enhancing electrochemical activity. The increased integrity by its appropriate compatibility of bismuth sulfide or iron sulfide with the iron matrix might improve strength in the matrix. Fe-S-Bi bonding was suggested by Posada et al. [20], in which a sample with bismuth sulfide, iron, PP and K_2CO_3 showed highest active material utilization and highest coulombic efficiency within 35 cycles.
- The large brittle particles of iron sulfide/bismuth sulfide, redox potential and formation of FeS might play a beneficial role in preserving porosity upon charging/discharging retaining discharge capacity, therefore preserving internal space for discharge products and increasing active material plus (in situ) formation of FeS (which was seen as a rough surface). Comparing the solubility constant of iron sulfide with bismuth sulfide, the solubility constant of iron sulfide is much higher than for bismuth sulfide which might gradually release its sulfide ions compared to bismuth sulfide and shown in the graphs of stable plateaus effectively depassivating. This formation phenomenon was also described by Manohar et al. [13] in which the full mechanism was described.
- Sulfide ions with sufficient solubility and beneficial reduction potential might sustain porosity upon galvanostatic cycling increasing discharge capacity and preserving electrolyte excess in the anode while also serving conductivity. Sulfide ions might increase conductivity, can break down $Fe(OH)_2$ layers, weaken the oxide layers [48] and might decrease hydrogen evolution reaction. It might bond with FeS to sustain conductivity and provide compatibility as explained earlier. The increased solubility of FeS might enhance this behaviour even further since increased solubility provides the sulfide ions to effectively participate in the system and accumulate dispersed on the surface [13] [14]. In addition, FeS shows an excellent electrical conductivity of around $1.5*10^3$ S/cm.

We observe that the samples with zinc sulfide and bismuth oxide showed less roughening and more cracking and rupture in the surface and could not sustain high capacity retention. The combined reasoning can be:

- The compatibility effect of bismuth sulfide and iron sulfide with the iron matrix was less plausible for zinc sulfide and bismuth oxide, since it could not from FeS. This might lower mechanical integrity, having more internal stress causing cracking.
- The combination of the smaller particle size of zinc sulfide and bismuth oxide, lack of formation of FeS, and low reduction potential of zinc sulfide (-1.56V vs MMO) [17] might prevent large pore formation over the cycles serving for sustained discharge capacity and electrolyte accessibility.
- A reason for capacity fade in long-term durability test might be the lower solubility (around 10^{-23} compared to 10^{-19} for FeS) hindering effective participation in the system effectively suppressing passivation in combination with lack of ZnS-Fe compatibility effects. The electrical conductivity of ZnS which was around $1*10^{-6}$ S/cm compared to 10^3 S/cm for FeS [17]. Some trends could be observed within the electrical conductivity but not for the solubility, since bismuth sulfide was almost insoluble but reached high discharge capacity. The electrical conductivity was assumed that bismuth oxide had a low electrical conductivity and bismuth sulfide exhibited higher electrical conductivity. Bismuth oxide might miss the essential role of sulfide ions or suffer from its higher HER current density as seen in CV.

Note that all explanations for the electrochemical behaviour in the durability test were based on the electrochemical properties and post-test surface characterization. The electrochemical material's properties of the different additives might enhance with the effects of surface roughness in which active

material is increased and is accounted for a molar volume change by the discharge products, therefore preserving stability. This surface roughness might come from the electrochemical property of a beneficial reduction potential, but it might also be that the individual particle size might play a role here. It should be made clear though, either the particle size or the material's properties had what degree of contribution to the roughness of the post-test surface analysis. E.g., it is mentioned that bismuth sulfide and iron sulfide had a clear roughened structure and could sustain higher electrochemical performance. The roughness can be clarified by the material's properties (such as a beneficial reduction potential or exhibition of S^{2-}-ions accumulating FeS) and the larger brittle particles as mentioned. Material's properties and particle size thus, are accounting both for larger porosity, roughness and increased retention of capacity. Also, material's properties such as the electrical conductivity, higher solubility for FeS, exhibition of S^{2-} suppressing unwanted side reactions might directly contribute to the increased performance. Note that since the mass and dispersion of all additives within the hot-pressed powders were kept constant, it was assumed that the particle size had inferior effect to material's properties on the roughness and totally inferior to the total performance, and relied more on the intrinsic properties on the individual additives. The smaller particle sizes can contribute to more efficient electron transfer, which might be confirmed by the detailed representation of the CVs by bismuth oxide and zinc sulfide and the more linear behaviour in CV for bismuth sulfide and iron sulfide. In a future study this should be made clear by keeping all particle sizes constant.

With a specific capacity of around 15.6 mAh/g and a theoretical capacity of 1273 mAh/g (considering the first discharge and two second discharge reactions[1].), the DoD was around 1.2%[2]. The two deep discharge reactions were also considered since it was not obvious that these reactions had not occurred. However, the plateau higher than -0.70V in durability tests for the half cell is not clearly visible. This cut-off was chosen as the deep discharge conversion should occur at these potentials. According to Rodriguez et al. [44] the formation was visible in the first 46 cycles, which was not reached in this study. Compared to this study of Rodriguez et al., the total discharge capacity is of the same order, but the specific discharge capacity is significantly higher. Note that they observed higher amount of cycles for the formation (more than the total measured here in the half cell). In the study of Rodriguez et al. [44] it was observed the active material was equal to 85 mg active material, compared to 5.33 gr active material exposed in this work. Moreover, within this configuration, the cell was able to withstand a current density of C/5 equal to 250mA/g (=21.25mA or 106mAh total capacity with 85 mg iron) leading a total of 1250mAh/g in 5 hours. We were not able to cycle the anodes for more than $\pm$10 cycles with current around 20mA. We applied 8.3mA for 10h adding up to a total charge of 83mAh. Since the active material is way higher, the specific capacity is way lower, around 15.6 mAh/g. Based on Rodriguez et al. results [44], we observe a low DoD, not necessarily laid in the time or charge/discharge current but laid in the total active mass of iron. It might be that the anode was still under formation and reactivation of the material might happen out of the capacity range measured in this work. Almost all studies in literature show higher current densities and lower amount of active material which makes the specific discharge capacity higher. Concerning the full cell, studies were limited with these additives. The study of Rodriguez et al. in 2017 [8] has shown both full cell and half cell measurement for iron-based anodes and the Iron-Air Battery. They achieve higher current densities. For real life battery application and the goal, it is necessary to increase the discharge capacity to at least 0.20 Ah/g with a rate of discharge C/20 and charge C/5 for only the conversion Fe/Fe(II) cutting off deep discharge products.

The hypothesis was partially confirmed that Bi_2O_3 and ZnS indeed could suppress HER. In contrast to the hypothesis however, ZnS did not perform better than FeS in contrast to a study by Mitra et al. [17], in which was stated that ZnS was promising over FeS. FeS was mostly indicated as promising in combination by bismuth oxide as researched by Manohar et al. [14]. Here, FeS was revealed as individual important additive.

[1]The discharge capacity theoretical value of around 1273 mAh/g considering the steps (Fe/Fe(II) 960 mAh/g plus the 320 mAh/g from Fe(II)/Fe(II,III) conversion. If the total is considered, an additional amount of 480 mAh/g should be added for Fe(II)/Fe(III)

[2]The specific discharge capacity may be defined as the capacity over the active material. If only the outer layer of the anode is defined (a thinner electrode appearance), the DoD can be increased with multiplication of around 10 or 20.

7

Conclusion

The effect of 10wt.% pore former on the initial capacity in a hot-pressed iron-based powder was studied referring to the research question of: *What is the effect of 10wt% K_2CO_3 pore former on the initial capacity and after 20 cycles of iron-based pressed-plate pellets?*. The main conclusions are stated here:

- Of all samples pressed, many samples with pore formers showed coarsening, pore induced cracking and non-uniform distribution of the pore formers, especially when cooled in open air between blocks.
- The most stable pore formation mainly seemed to occur in open air without prior blocks, simultaneously also prone to attraction of ions from open air.
- Moisture absorption, incomplete decomposition plus K_2O residuals can clarify the constant value for porosity.
- The higher discharge current for initial test and higher charge current for 20 cycles might have contributed to the active material and mechanical loss of the sample with pore former.
- The mechanical degradation caused by these pore formers might have led to increased propensity for capacity fade shown by lower (27 mAh/g) capacity fade in the half cells.
- The samples in the full test showed reversed behaviour: the sample with pore former could sustain capacity.
- The lower current densities might have lead to a stable sample with pore former by the heavy roughened stable sample after testing. There might have occurred some more stable dissolution over time increasing porosity.

Note that full cell performance of the sample with and without pore former was extended and the sample with pore former could be extended for another 10 cycles which was not given. All in all, a balance should be found between mechanical stability, effect of pore former within a thicker anode and maximized specific discharge capacity with in a thinner electrode to maximize the specific discharge capacity of the anode. Stable pore creation might be achieved by lower pressure.

The individual role of four different promising additives Bi_2S_3, Bi_2O_3, ZnS and FeS on the HER and passivation behaviour were studied. The research question was: *What is the effect of the additives Bi_2S_3, Bi_2O_3, ZnS and FeS on the HER and passivation behaviour of iron-based pressed-plate pellets?* The main findings are given here:

- The pristine sample showed in CV increasing current densities and increasing slope near the HER potential with equal passivation behaviour compared to ZnS, FeS and Bi_2S_3, confirming the effective working of the additives. In durability tests, FePE showed faster passivation than bismuth sulfide and iron sulfide.
- The sample with Bi_2O_3 exhibits reversibility properties shown by CV, while shifting peak potentials of the reduction towards more positive potentials, while it was shown that the current density near the HER potential increased which might be due to increased conductivity. It was shown by XPS that the intensity for stable oxide peak Fe_2O_3 and FeOOH peak decreased with respect

to the FeO peak compared to identical peaks in the XPS spectra for the other samples. This effective deposition of Bismuth and reduced oxide products was confirmed by XPS. The beneficial higher reduction potential of bismuth oxide might provide this deposition of bismuth and clarify reversibility stability within the anodes.

- ZnS showed faster passivation behaviour than a pristine sample, but also showed a large decline in the current density and slope near the HER potential. ZnS might suffer in a durability test from the lower reduction potential and lower electrical conductivity.
- The sample with Bi_2S_3, FeS and showed predominantly a linear relationship in the CV curves and both showed declining slopes for HER, although bismuth sulfide still has high absolute values. FeS and Bi_2S_3 showed the highest capacity retention. The sample with FeS, had FeS readily available in contrast to bismuth sulfide and might clarify its more stable performance over Bi_2S_3.

Although powder samples reveal great opportunity for iron electrodes, the porosity was quite low. Increasing this porosity might lead to higher effective area and higher discharge capacity by giving the opportunity to lower the thickness. The particle size could clarify the differences in CV curves and the roughness behaviour after testing.

This study portrays a systematic study in studying the effectiveness of porosity and specific additives in hot-pressed iron-based anodes, which portrays a novelty within this field. To reflect to the initial motivation of this work, the studies in the pore formers should be carried out in another study to see the ratio of decomposition and dissolution to a clear extend. The study on the additives was driven by the inconsistency in literature on equal manufacturing, experimental conditions and cell design. This work aims to address this inconsistency and results indicate that iron sulfide and bismuth sulfide tend to hold a capacity retention of 100% up to cycle 36 in the half cell both an and to 41 and 29 in the full cell both. An enhancing effect of the reversibility of bismuth oxide could be combined with the a high performance additive such as FeS. This might be a great starting point for further research. Combination of bismuth oxide and a metal sulfide could allow for enhancement of electrochemical properties such as reversibility and passivation suppression.

8

Future Work

8.1. General improvements

In general, for future work, great opportunity can be listed relying on cell design, electrolyte control and porosity measurements:

- The cell design should be designed in such a way that hydrogen gas release does not control the volume of the electrolyte, neither the kinetics or dominant reactions on the anode surface. Cell design in combination with the shape of the anode was also important to consider. An alternative for copper tape such as silver ink (Ag-ink) or a current collector such as a SS-mesh or Ni-mesh in the iron-based anode can be applied. Since, copper tape used in this study might have been one of the biggest contributors to poor connection within the anode. Spot welding on sintered anodes can enhance particle connectivity. Proper methods should be investigated to insert this the SS-mesh or Ni-mesh into the powder sample. Adequate molds are available already.
- Considering the protocol for electrolyte refillment, this should be controlled adequately in a future study. Now, all full cells were refilled in the first couple of cycles and the half cell was refilled if there was a total leakage from the top of the cell. During the tests which might endured for three to four weeks, the electrolyte level was monitored but might not have been constant for all half cells. An exact correlation could be investigated on electrolyte level and electrochemical behaviour, but in this study it seemed that level the refillment did not have a clear effect on the overall behaviour. The half-cell and full-cell test could be repeated more with the exact same experimental conditions. The electrolyte level and state of charge/discharge might have effected post test topology and roughness. It should be made sure that the samples were all in the exact same charged or discharged state with equal amount of underwent cycles.
- A more precise porosity measurement technique could have been applied such as a BET-analysis instead of isopropanol immersion, since the precision of the porosity measurements were questioned (rippening off powder, fast drying time). Measurement techniques to quantify the amount of ions in the electrolyte would be helpful to investigate the ratio of dissolution and decomposition. The ratio of decomposition versus dissolution in the electrolyte might be characterized by a Ion-Selective Electrode technique order to map the dissolution of carbonates into the electrolyte. This technique can also help to calculate the dissolved specific ions from the additive.

8.2. Future

For future studies, opportunities follow in two directions: the manufacturing of the anode with desired electrochemical properties and the electrochemical conditions. For fabrication of the anodes, a hard grade type was chosen: CIP OM, prepared by Metal Injection Molding [33]. This made the anodes relatively brittle to the samples prepared with a soft grade (CIP SM, prepared by diamond tools). The soft grade might also increase defect density having increased electrochemical activity. This increased defect density might also increase the plastic binder properties better adhering to this compound. Ball milling mixing and sintering should be considered as well. Sintering can increase long term mechanical stability, inter particle connectivity and can increase conductivity. Ball milling might increase defect

density within the sample, increasing active sites for redox reactions. It will be an opportunity to make the anode significant thinner in order to maximize specific discharge capacity. The total surface area will be utilized and the specific discharge capacity will be increased by less amount of active material. Note that the mechanical stability is also influenced by the thickness of the samples. A balance should be found here. Together with interparticle connectivity and mechanical stability (achieved by higher pressure) and porosity (achieved by lower pressure) of the sample the optimal conditions should be found to investigate deeper levels of discharge. As mentioned earlier, the particle size of all additives could be held constant.

Considering the electrochemical tests, the cut-off -0.70V was chosen for half-cell porosity studies in order to only measure capacity from conversion of Fe/Fe(II). In future, this might be enlarged. In addition, the cut-off of -0.55V might be enlarged. For future work, lower scanning rates can be investigated in the CV and more cycles, to see the electrochemical evolving behaviour. Also, increased amount of cycles could be researched with other electrochemical conditions to make sure not to include the the formation period. This formation can be help to sustain discharge capacity over time by gradually activating the material in the sample. So, it is plausible that all tested anodes were in the formation period.

References

[1] *IEA – International Energy Agency*. https://www.iea.org/. (Accessed on 10/10/2023).

[2] *Greenhouse Gas Emissions from Energy Data Explorer – Data Tools - IEA*. https://www.iea.org/data-and-statistics/data-tools/greenhouse-gas-emissions-from-energy-data-explorer. (Accessed on 10/15/2023).

[3] Henning Weinrich et al. "Silicon and Iron as Resource-Efficient Anode Materials for Ambient-Temperature Metal-Air Batteries: A Review". In: *Materials* 12.13 (July 2019), p. 2134. DOI: 10.3390/ma12132134.

[4] Manuel Salado and Erlantz Lizundia. *Advances, challenges, and environmental impacts in metal–air battery electrolytes*. Aug. 2022. DOI: 10.1016/j.mtener.2022.101064.

[5] William B Jensen. "Faraday's laws or Faraday's law?" In: *Journal of Chemical Education* 89.9 (2012), pp. 1208–1209.

[6] R. D. McKerracher et al. "Improving the stability and discharge capacity of nanostructured Fe2O3/C anodes for iron-air batteries and investigation of 1-octhanethiol as an electrolyte additive". In: *Electrochimica Acta* 318 (Sept. 2019), pp. 625–634. ISSN: 0013-4686. DOI: 10.1016/J.ELECTACTA.2019.06.043.

[7] *Iron Air Battery: How It Works and Why It Could Change Energy*. https://www.popularmechanics.com/science/energy/a42532492/iron-air-battery-energy-storage/. (Accessed on 05/31/2023).

[8] H. A. Figueredo-Rodríguez et al. "A Rechargeable, Aqueous Iron Air Battery with Nanostructured Electrodes Capable of High Energy Density Operation". In: *Journal of The Electrochemical Society* 164.6 (2017), A1148–A1157. ISSN: 0013-4651. DOI: 10.1149/2.0711706jes.

[9] Henning Weinrich et al. "Impact of the charging conditions on the discharge performance of rechargeable iron-anodes for alkaline iron–air batteries". In: *Journal of Applied Electrochemistry* 48.4 (Apr. 2018), pp. 451–462. ISSN: 15728838. DOI: 10.1007/s10800-018-1176-4.

[10] Henning Weinrich et al. "Electrode thickness-dependent formation of porous iron electrodes for secondary alkaline iron-air batteries". In: *Electrochimica Acta* 314 (Aug. 2019), pp. 61–71. ISSN: 00134686. DOI: 10.1016/j.electacta.2019.05.025.

[11] Henning Weinrich et al. "Understanding the nanoscale redox-behavior of iron-anodes for rechargeable iron-air batteries". In: *Nano Energy* 41 (Nov. 2017), pp. 706–716. ISSN: 22112855. DOI: 10.1016/j.nanoen.2017.10.023.

[12] Chenguang Yang, Aswin K. Manohar, and S. R. Narayanan. "A High-Performance Sintered Iron Electrode for Rechargeable Alkaline Batteries to Enable Large-Scale Energy Storage". In: *Journal of The Electrochemical Society* 164.2 (2017), A418–A429. ISSN: 0013-4651. DOI: 10.1149/2.1161702jes.

[13] Aswin K. Manohar, Chenguang Yang, and S. R. Narayanan. "The Role of Sulfide Additives in Achieving Long Cycle Life Rechargeable Iron Electrodes in Alkaline Batteries". In: *Journal of The Electrochemical Society* 162.9 (2015), A1864–A1872. ISSN: 0013-4651. DOI: 10.1149/2.0741509jes.

[14] Aswin K. Manohar et al. "Enhancing the Performance of the Rechargeable Iron Electrode in Alkaline Batteries with Bismuth Oxide and Iron Sulfide Additives". In: *Journal of The Electrochemical Society* 160.11 (2013), A2078–A2084. ISSN: 0013-4651. DOI: 10.1149/2.066311jes.

[15] Aswin K. Manohar et al. "Understanding the Factors Affecting the Formation of Carbonyl Iron Electrodes in Rechargeable Alkaline Iron Batteries". In: *Journal of The Electrochemical Society* 159.12 (2012), A2148–A2155. ISSN: 0013-4651. DOI: 10.1149/2.021301jes.

[16] Aswin K. Manohar et al. “A High-Performance Rechargeable Iron Electrode for Large-Scale Battery-Based Energy Storage”. In: *Journal of The Electrochemical Society* 159.8 (2012), A1209–A1214. ISSN: 0013-4651. DOI: 10.1149/2.034208jes.

[17] D. Mitra et al. “High Performance Iron Electrodes with Metal Sulfide Additives”. In: *Journal of The Electrochemical Society* 168.3 (Mar. 2021), p. 030518. ISSN: 0013-4651. DOI: 10.1149/1945-7111/abe9c7.

[18] Bui Thi Hang et al. “ Nanoparticle Fe 2 O 3 -Loaded Carbon Nanofibers as Iron-Air Battery Anodes ”. In: *Journal of The Electrochemical Society* 160.9 (2013). ISSN: 0013-4651. DOI: 10.1149/2.066309jes.

[19] S Malkhandi et al. *Organo-sulfur Additives for Suppressing Hydrogen Evolution in Iron-Air Battery*. Tech. rep. 2011.

[20] Jorge Omar Gil Posada and Peter J. Hall. “Post-hoc comparisons among iron electrode formulations based on bismuth, bismuth sulphide, iron sulphide, and potassium sulphide under strong alkaline conditions”. In: *Journal of Power Sources* 268 (Dec. 2014), pp. 810–815. ISSN: 03787753. DOI: 10.1016/j.jpowsour.2014.06.126.

[21] Enbo Shangguan et al. “Sublimed sulfur powders as novel effective anode additives to enhance the high-rate capabilities of iron anodes for advanced iron-based secondary batteries”. In: *Electrochimica Acta* 301 (Apr. 2019), pp. 162–173. ISSN: 00134686. DOI: 10.1016/j.electacta.2019.01.139.

[22] Jang Soo Lee et al. *Metal-air batteries with high energy density: Li-air versus Zn-air*. 2011. DOI: 10.1002/aenm.201000010.

[23] Jorge Omar Gil Posada and Peter J. Hall. “The Effect of Electrolyte Additives on the Performance of Iron Based Anodes for NiFe Cells”. In: *Journal of The Electrochemical Society* 162.10 (2015), A2036–A2043. ISSN: 0013-4651. DOI: 10.1149/2.0451510jes.

[24] Alagar Raj Paulraj et al. “Electrochemical performance and in operando charge efficiency measurements of Cu/Sn-doped nano iron electrodes”. In: *Batteries* 5.1 (Mar. 2019). ISSN: 23130105. DOI: 10.3390/batteries5010001.

[25] R. D. McKerracher et al. *A review of the iron-air secondary battery for energy storage*. 2015. DOI: 10.1002/cplu.201402238.

[26] Bui Thi Hang et al. “Effect of metal-sulfide additives on electrochemical properties of nano-sized Fe2O3-loaded carbon for Fe/air battery anodes”. In: *Journal of Power Sources* 168.2 (June 2007), pp. 522–532. ISSN: 03787753. DOI: 10.1016/j.jpowsour.2007.02.067.

[27] Mylad Chamoun et al. “Stannate Increases Hydrogen Evolution Overpotential on Rechargeable Alkaline Iron Electrodes”. In: *Journal of The Electrochemical Society* 164.6 (2017), A1251–A1257. ISSN: 0013-4651. DOI: 10.1149/2.1401706jes.

[28] Bui Thi Hang et al. “The effect of additives on the electrochemical properties of Fe/C composite for Fe/air battery anode”. In: *Journal of Power Sources* 155.2 (Apr. 2006), pp. 461–469. ISSN: 03787753. DOI: 10.1016/j.jpowsour.2005.04.010.

[29] Bo Yang et al. “Organo-sulfur molecules enable iron-based battery electrodes to meet the challenges of large-scale electrical energy storage”. In: *Energy and Environmental Science* 7.8 (2014), pp. 2753–2763. ISSN: 17545706. DOI: 10.1039/c4ee01454e.

[30] M. K. Ravikumar et al. “In Situ Crystallographic Probing on Ameliorating Effect of Sulfide Additives and Carbon Grafting in Iron Electrodes”. In: *Journal of The Electrochemical Society* 162.12 (2015), A2339–A2350. ISSN: 0013-4651. DOI: 10.1149/2.0721512jes.

[31] P Periasamy, B Ramesh Bahu, and S Venkatakrishna Iyer. *Performance characterization of sintered iron electrodes in nickel/iron alkaline batteries*. Tech. rep. 1996, pp. 9–14.

[32] Zhen Qiu. “Transition Metal-Based Electrocatalysts for Alkaline Water Splitting and CO2 Reduction”. PhD thesis. Acta Universitatis Upsaliensis, 2019.

[33] *Carbonyl Iron Powder - PDF Free Download*. https://docplayer.net/23874265-Carbonyl-iron-powder.html. (Accessed on 09/20/2023).

[34] *MIPELON*. https://tw.mitsuichemicals.com/rwd1438/store/F3/MIPELON_EN.pdf. (Accessed on 09/26/2023).

[35] *Potassium carbonate ACS reagent, = 99.0 584-08-7*. https://www.sigmaaldrich.com/NL/en/product/sigald/209619. (Accessed on 09/20/2023).

[36] *Potassium hydroxide, ca. 85%, ACS reagent, Thermo Scientific Chemicals*. https://www.thermofisher.com/order/catalog/product/424140050. (Accessed on 10/17/2023).

[37] *Bismuth(III) sulfide, 99.9% (metals basis), Thermo Scientific Chemicals | Fisher Scientific*. https://www.fishersci.se/shop/products/bismuth-iii-sulfide-99-9-metals-basis-thermo-scientific/11398727. (Accessed on 10/16/2023).

[38] *Bismuth(III) oxide, 99.9%, extra pure, Thermo Scientific Chemicals*. https://www.thermofisher.com/order/catalog/product/208075000?SID=srch-srp-208075000. (Accessed on 09/20/2023).

[39] *Zinc sulfide - Zinc sulphide*. https://www.sigmaaldrich.com/NL/en/substance/zincsulfide97461314983. (Accessed on 09/20/2023).

[40] *Specs_demiwater_-_EN.pdf*. https://www.hatenboer-neptunus.nl/fileadmin/user_upload/Z_HN_verzamelmap/HN_Downloads/Specs_demiwater_-_EN.pdf. (Accessed on 10/17/2023).

[41] *High Performance Alkaline Air Diffusion Electrode (ADE) with Non-Precious Metal Catalyst*. https://www.fuelcellstore.com/high-performance-alkaline-air-diffusion-electrode-72660000. (Accessed on 10/10/2023).

[42] Bingbing Tian et al. “The effect of Na2S additive in alkaline electrolyte on improved performances of Fe-based air batteries”. In: *Electrochimica Acta* 259 (Jan. 2018), pp. 196–203. ISSN: 00134686. DOI: 10.1016/j.electacta.2017.10.136.

[43] A Sundar Rajan et al. “Carbonyl-Iron Electrodes for Rechargeable-Iron Batteries”. In: *Electrochem. Energy Technol* 1 (2014), pp. 2–9. DOI: 10.1515/eetech-2014-0002.

[44] H. A. Figueredo Rodríguez et al. “Improvement of Negative Electrodes for Iron-Air Batteries: Comparison of Different Iron Compounds as Active Materials”. In: *Journal of The Electrochemical Society* 166.2 (2019), A107–A117. ISSN: 0013-4651. DOI: 10.1149/2.1071816jes.

[45] Richard L. Lehman, Jefffery S. Gentry, and Nick G. Glumac. “Thermal stability of potassium carbonate near its melting point”. In: *Thermochimica Acta* 316.1 (1998). ISSN: 00406031. DOI: 10.1016/S0040-6031(98)00289-5.

[46] Jill Chastain and Roger C King Jr. “Handbook of X-ray photoelectron spectroscopy”. In: *Perkin-Elmer Corporation* 40 (1992), p. 221.

[47] Honghui Yang, Bofang Shi, and Silan Wang. “Fe oxides loaded on carbon cloth by hydrothermal process as an effective and reusable heterogenous Fenton catalyst”. In: *Catalysts* 8.5 (2018). ISSN: 20734344. DOI: 10.3390/catal8050207.

[48] Bui Thi Hang et al. “Fe2O3-filled carbon nanotubes as a negative electrode for an Fe-air battery”. In: *Journal of Power Sources* 178.1 (Mar. 2008), pp. 393–401. ISSN: 03787753. DOI: 10.1016/j.jpowsour.2007.12.012.

A

Appendix A

A.1. Research Hot Pressing

Different factors that affect the final discharge products:

1. The number of components: the powder compositions tested in order to optimize the structure was 3 or 5. It was observed that the stability decreased when embedding >3 components. If this had to do with predominantly with addition of poreformer, should be reconsidered in further studies. To clarify, the reason of stability of the sample was also confirmed with high amount of iron content. The wt% of PE was also tested. Increasing the value to >5wt% would coarsen the samples heavily. Samples were tested without PE and confirmed the mechanical vulnerability to a large extent. It was chosen to stick to 5wt% PE. The temperature: the temperature was initially set at 150^{o}C to ensure the reaching of the melting temperature of 136^{o}C was reached, so that the PE would approximately reach its melting temperature acting as cohesive between dissimilar powder components. It was chosen to preheat the PE around 5 minutes in the mold before pressing.
2. The pressing time: pressure timing of 5, 10 and 15 minutes were applied to the powder pressing procedure. In case of very thin samples (<1.5mm) it was required to apply 15 minutes pressing time to ensure mechanical stability.
3. The press type: initially, a Zwick Hot Press was used which allowed for high precision and control of the load, time and temperature. This instrument allowed for compact testing while recording real-time load-distance data with automatic pressure control. This advanced system allowed us to give electrodes with excellent stability properties. However, the instrument operation required long times end therefor in the end, a bench-top Manual Flat Hydraulic Hot Pellet Press (Double Plate) of maximum 30T was used.
4. Morphology: rectangular dies of with available anode surface were equal to 20mmx20mm, 30mm x30mm and 40mmx40mm. Considering the available cell design and material cost, the 30mm x30mm mold was depicted. The cooling method: when the samples were initially cooled in the open air, clear curvature was observed after 30 min. The curvature was seen that the corners of the samples were slightly curled upward. It was explained that this had to do with cooling of PE. If the sample was cooled and one side was exposed to convection as well, that side would cool down faster and reduce size causing compressive stresses. This curvature was also related to the thickness of the sample.
5. The electrode thickness/amount of material: higher thickness of the anodes provided higher mechanical stability, but might lower the specific capacity, according to Weinrich et. al. [10]. It was required to set the electrode thickness to at least 3.5mm in order to obtain stable anodes.
6. The pressure: a balance had to be found since high compactness for particle inter-connectivity had to be maintained and thus conductivity requires high loads which might reduce porosity lowering accessibility of the electrolyte. Comparing 20, 40, 60 and 88MPa, a highest stability was observed with 88MPa preserving stability and porosity simultaneously. This was tested for a sample with iron, copper sulfide, PE, potassium carbonate and bismuth oxide. The optimized final procedure of hot pressing is depicted in Figure 4.2 as a step-wise illustration.

A.2. Research Mixing Effect

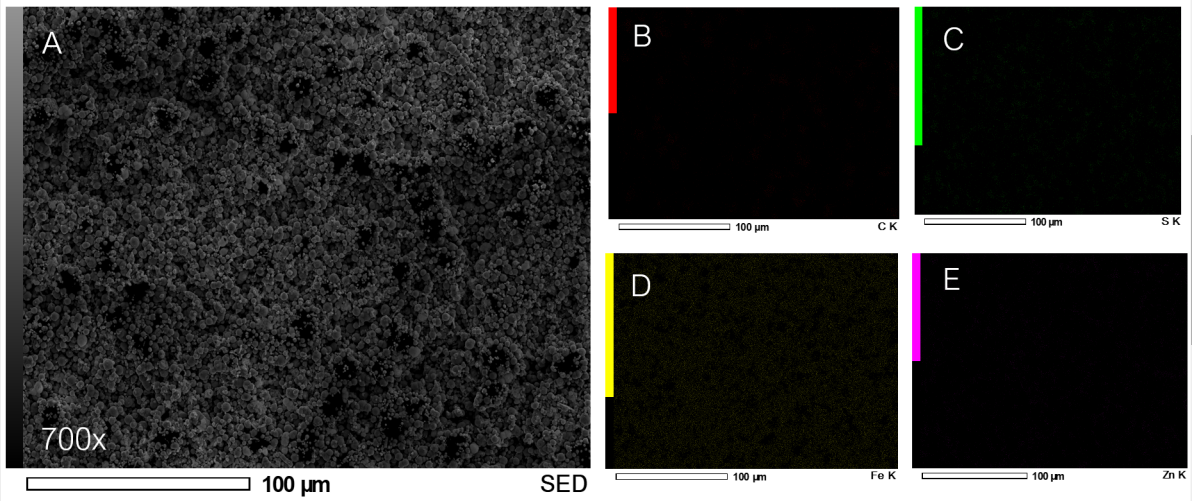

Figure A.1: SEM image of a sample with Fe, PE and ZnS. In here the mixing effect was identified.

A.3. Extended Lifetime FeS

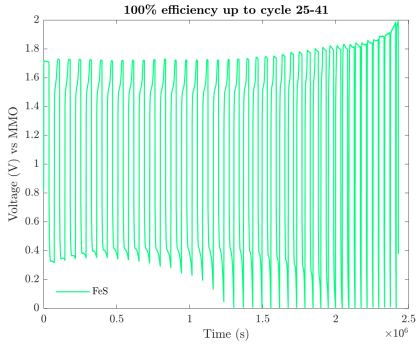

Figure A.2: Extension of lifetime measurement of FeS.

A.4. Research Current Densities

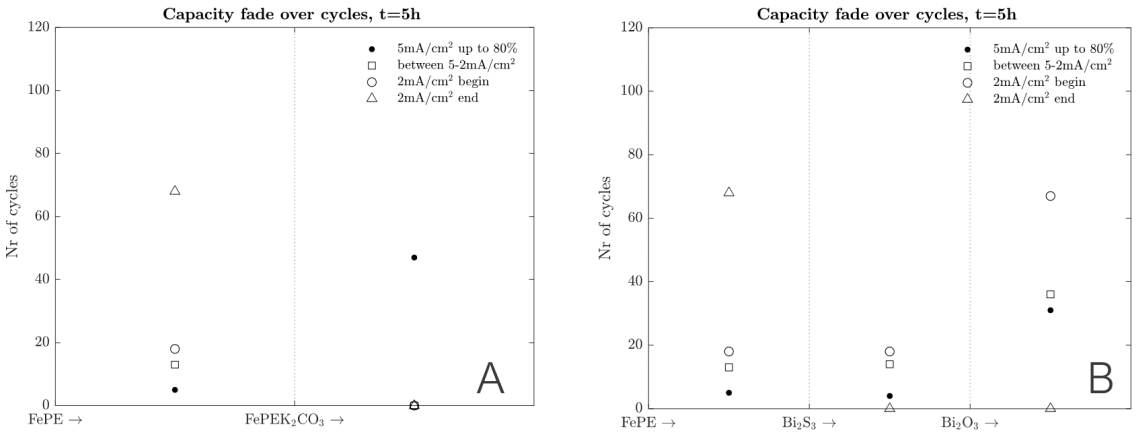

Figure A.3: Current density variation in order to optimize the experimental conditions.

B

Appendix B

B.1. Tables

Table B.1: Results of Bruker Interferometer Roughness values.

Roughness 0.3mm Square					Roughness 1mm Square Stitched				
Sample	**Ra (μm)**	**Ra av**	**Rp**	**Rp av**	**Sample**	**Ra (μm)**	**Ra av**	**Rp**	**Rp av**
	1.54		12.06			1.72		12.06	
FePE	1.69	1.71	10.49	12	FePE	1.33	1.58	10.49	12.00
	1.91		13.45			1.68		13.45	
	1.11		12.34			1.17		12.29	
1	1.01	1.12	13.27	12.72	1	1.04	1.09	12.99	13.38
	1.25		12.55			1.05		14.86	
	1.52		8.07			0.95		14.61	
2	1.75	1.67	8.62	8.67	2	1.60	1.30	10.88	13.40
	1.74		9.3			1.35		14.72	
	1.97		11.95			1.78		15.81	
4	1.76	1.83	13.40	12.26	4	1.39	1.61	15.99	15.73
	1.75		11.43			1.65		15.39	
	1.06		11.26			1.09		11.26	
5	0.76	1.11	11.79	11.30	5	0.76	1.04	15.01	13.96
	1.50		10.86			1.28		15.60	

Table B.2: Theoretical values from the Fe2p$_{3/2}$ are depicted from the book Chastain et al. [46]. Values in the O1s peak are depicted from Yang et al. [47].

Theory				Sample			
Compound	**Valence**	**Theoretical Value (eV)**	**Peak**	**1**	**2**	**4**	**5**
FeO	Fe^{2+}	709.4	1	708.97	709.41	709.52	708.8
Fe_2O_3	Fe^{3+}	710.8	2	710.33	710.64	711.02	709.95
FeOOH	Fe^{3+}	711.5	3	712.01	712.33	713.21	712.14
FeS	Fe^{2+}	712	4	713.71	-	-	714.38
Satellite	-		5	718.48	717.55	718.38	718.57
FeO	Fe^{2+}	722	6	722.91	722.77	722.51	722.84
Fe_2O_3	Fe^{3+}	725	7	725.29	725.19	724.43	725.23
Compound	**Valence**	**Theoretical Value (eV)**	**Peak**	**1**	**2**	**4**	**5**
FeO	Fe^{3+}	529.7	1	529.8	529.07	529.81	529.17
FeOH	Fe^{3+}	531.0	2	531.4	531.05	531.38	531.01
H_2O	-	532.3	3	533.4	533.02	533.02	533.02